USGS
science for a changing world

Wave-Driven Spatial and Temporal Variability in Sea-floor Sediment Mobility in the Monterey Bay, Cordell Bank, and Gulf of the Farallones National Marine Sanctuaries

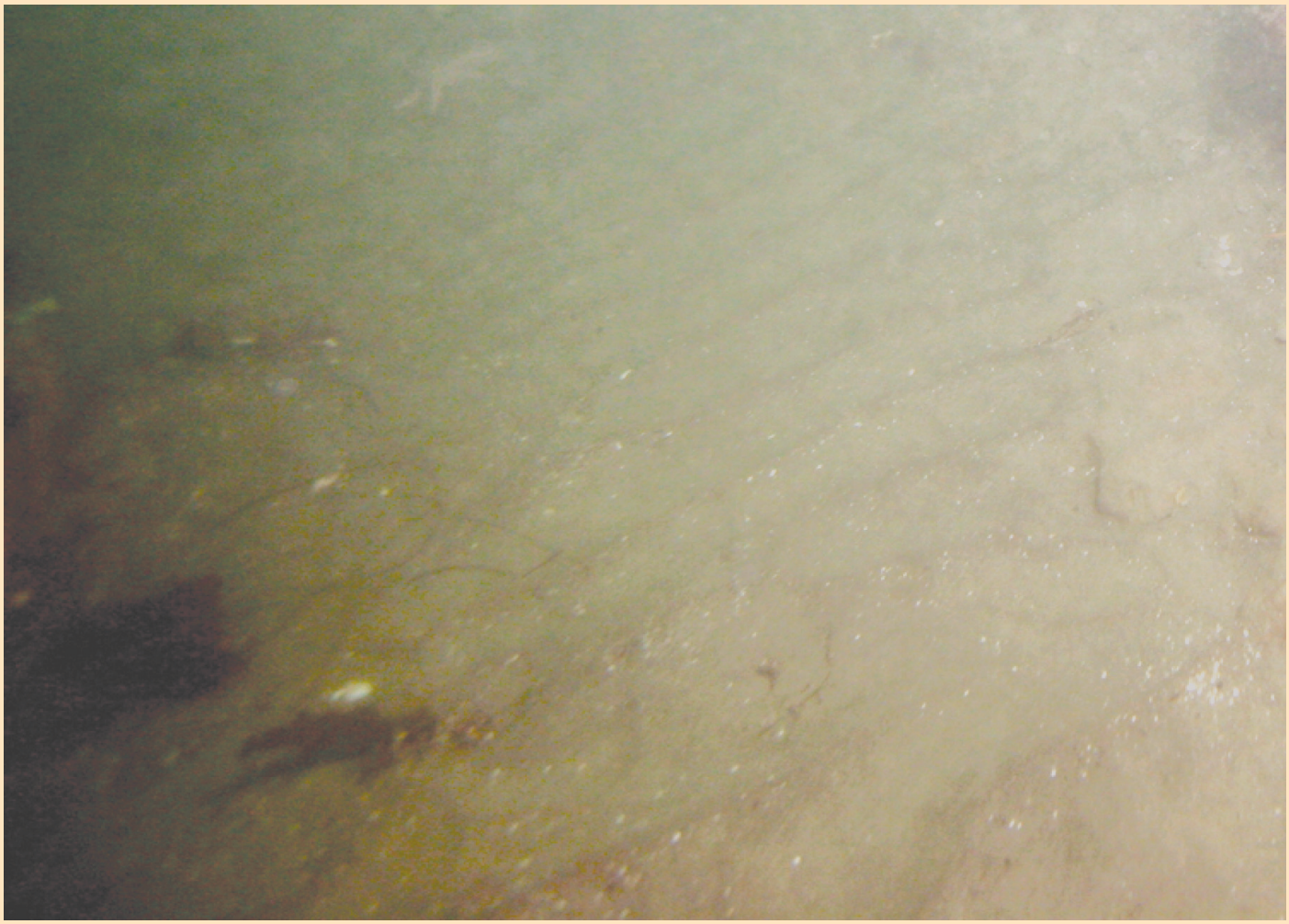

Scientific Investigations Report 2007–5233

U.S. Department of the Interior
U.S. Geological Survey

This page intentionally left blank

Wave-Driven Spatial and Temporal Variability in Sea-floor Sediment Mobility in the Monterey Bay, Cordell Bank, and Gulf of the Farallones National Marine Sanctuaries

By Curt D. Storlazzi, Jane A. Reid, and Nadine E. Golden

Scientific Investigations Report 2007–5233

U.S. Department of the Interior
U.S. Geological Survey

U.S. Department of the Interior
DIRK KEMPTHORNE, Acting Secretary

U.S. Geological Survey
Mark D. Myers, Director

U.S. Geological Survey, Reston, Virginia: 2007

This report and any updates to it are available online at:
http://pubs.usgs.gov/sir/2007/5233

For product and ordering information:
World Wide Web: http://www.usgs.gov/pubprod
Telephone: 1–888–ASK–USGS

For more information on the USGS—the Federal source for science about the Earth, its natural and living resources, natural hazards, and the environment:
World Wide Web: http://www.usgs.gov
Telephone: 1–888–ASK–USGS

Any use of trade, product, or firm names in this publication is for descriptive purposes only and does not imply endorsement by the U.S. Government.

Although this report is in the public domain, permission must be secured from the individual copyright owners to reproduce any copyrighted materials contained within this report.

Cataloging-in-Publication data are on file with the Library of Congress (URL http://www.loc.gov/).

Produced in the Western Region, Menlo Park, California
Manuscript approved for publication, October 4, 2007
Text edited by James W. Hendley II
Layout and design by Stephen L. Scott

Cover—Wave orbital ripples at a depth of 15 m in the Monterey Bay National Marine Sanctuary.

Contents

Abstract ---- 1
Introduction ---- 1
Study Area ---- 2
Methods ---- 4
Sediment Cover of the Central California Continental Shelf ---- 4
Gridded Coverage of Sediment Grain Size ---- 5
Wave Data ---- 7
Wave Modeling ---- 10
Threshold for the Initiation of Sediment Transport ---- 10
Results ---- 15
Discussion ---- 30
Geological Implications ---- 30
Biological Implications ---- 30
Conclusions ---- 33
Acknowledgments ---- 33
References ---- 33
Appendixes 1-41 ---- 35

Figures

1. Map of the study area ---- 2
2. Distribution of bathymetry by depth range ---- 3
3. Wave rose for central California ---- 3
4. Grid of central grain-size data in mm ---- 5
5. Grid of central grain-size data by grain-size class ---- 6
6. Histograms of surficial sediment distributions ---- 8
7. Multivariate El Niño-Southern Oscillation (ENSO) index ---- 10
8. Temporal variability in the wave parameters for El Niño, La Niña conditions, and Normal conditions ---- 11
9. Delft 3D curvilinear modeling grid for the study area ---- 12
10. Example model run showing significant wave height for an El Niño February ---- 13
11. Example model run displaying peak wave-induced near-bed orbital wave velocity for an El Niño February ---- 14
12. Example model run displaying peak wave-induced near-bed shear stress ---- 16
13. Critical shear stresses for the initiation of sediment transport ---- 17
14. Example model run displaying regions mobilized and stable due to wave forcing during an El Niño February ---- 18
15. Example model run displaying regions mobilized and stable due to wave forcing during a La Niña October ---- 19
16. Plots showing the temporal variation in sea-floor disturbance by depth range ---- 20
17. Map of the study area showing the frequency of sea-floor disturbance during a year with Normal conditions. ---- 22
18. Map of the study area showing the frequency of sea-floor disturbance during a year with El Niño conditions. ---- 23
19. Map of the study area showing the frequency of sea-floor disturbance during a year with La Niña conditions. ---- 24
20. Map showing the difference in the frequency of sea-floor disturbance during El Niño and La Niña years. ---- 25

21. Map showing the difference in the frequency of sea-floor disturbance during El Niño and La Niña winter months---------- 26
22. Map showing the difference in the frequency of sea-floor disturbance during El Niño and La Niña spring months ---------- 27
23. Map showing the difference in the frequency of sea-floor disturbance during El Niño and La Niña summer months ---------- 28
24. Map showing the difference in the frequency of sea-floor disturbance during El Niño and La Niña fall months ---------- 29
25. Plot synthesizing the data on the spatial and temporal variations in sea-floor mobility between El Niño and La Niña conditions ---------- 31
26. Map of the study area displaying the mean peak near-bed wave orbital velocity ---- 32

Tables

1. Monthly climatic model run boundary conditions----------9
2. Return interval model run boundary conditions---------- 12
3. Percent of sea floor disturbed by depth range for return interval model run boundary conditions---------- 20
4. Percent of sea floor disturbed by depth range for climatic model run boundary conditions---------- 21

Wave-Driven Spatial and Temporal Variability in Sea-floor Sediment Mobility in the Monterey Bay, Cordell Bank, and Gulf of the Farallones National Marine Sanctuaries

By Curt D. Storlazzi, Jane A. Reid, and Nadine E. Golden

Abstract

Wind and wave patterns affect many aspects of continental shelves and shorelines geomorphic evolution. Although our understanding of the processes controlling sediment suspension on continental shelves has improved over the past decade, our ability to predict sediment mobility over large spatial and temporal scales remains limited. The deployment of robust operational buoys along the U.S. West Coast in the early 1980s provides large quantities of high-resolution oceanographic and meteorologic data. By 2006, these data sets were long enough to clearly identify long-term trends and compute statistically significant probability estimates of wave and wind behavior during annual and interannual climatic cycles (that is, El Niño and La Niña). Wave-induced sediment mobility on the shelf and upper slope off central California was modeled using synthesized oceanographic and meteorologic data as boundary input for the Delft SWAN model, sea-floor grain-size data provided by the usSEABED database, and regional bathymetry. Differences in waves (heights, periods, and directions) and winds (speeds and directions) between El Niño and La Niña months cause temporal and spatial variations in peak wave-induced bed shear stresses. These variations, in conjunction with spatially heterogeneous unconsolidated sea-floor sedimentary cover, result in predicted sediment mobility widely varying in both time and space. These findings indicate that these factors have significant consequences for both geological and biological processes.

Introduction

Wind and wave patterns can affect many aspects of continental shelf and shoreline evolution. Although our understanding of the processes controlling sediment suspension on continental shelves has improved over the past decade, our ability to predict sediment mobility over large spatial and temporal scales remains limited. The development, deployment, and continued maintenance of robust operational oceanographic systems off central California by the National Oceanic and Atmospheric Administration (NOAA) in the early 1980s provides large quantities of high-resolution oceanographic and meteorologic data, such as wave height, wave period, wave direction, wind speed, and wind direction. By 2003, these data sets were large enough to clearly identify long-term trends and compute statistically significant probability estimates of wave and wind behavior during seasonal, annual, and interannual climatic cycles (that is, El Niño and La Niña). Although many studies have investigated the wave climate along central California (Seymour and others, 1984; Inman and Jenkins, 1997; Allan and Komar, 2000; Bromirski and others, 2005), none have investigated how spatial and temporal variations in wave climate influence sediment mobility on the shelf and upper slope. Sea-floor sediment may be resuspended by these waves, depending on their height, period, water depth and the sediment grain size. These natural readjustments of unconsolidated sea-floor materials may influence both the recovery from human perturbations and/or cause short-lived natural disturbances. The effect on benthic and pelagic ecosystems will depend on local sea-floor conditions, sediment distributions, and ecological balances.

Here we interpolated the oceanographic and meteorologic data synthesized by Storlazzi and Wingfield (2005) across the continental shelf, and integrated these with gridded grain-size data held in the U.S. Geological Survey's (USGS) usSEABED compilation (Reid and others, 2006). These two data sets, complemented by bathymetry, allowed the prediction of seabed suspension and mobility at various spatial and temporal scales (months to decades) encountered under different climatic regimes (for example, during normal "winter" months, a typical El Niño January or a La Niña fall) or statistical projections (5-, 10-, 25-, 50- and 100-year storms). Understanding the spatial and temporal variability of these sea-floor disturbances can provide information to managers and planners so that the effects of particular man-

agement practices, such as dredge material disposal, can be forecast. This work would also provide practical scientific information to local, State, and Federal permitting agencies for use in the consideration of offshore activities such as trawling, dredging, and the placement of sea-floor engineering structures (cables, pipelines, others) that disturb the sea floor.

Study Area

The study area for this project extends approximately 280 km from just north of Bodega in Sonoma County southward to Point Sur in Monterey County and extends from the shoreline out past the 2,000-m isobath (fig. 1). Central California has

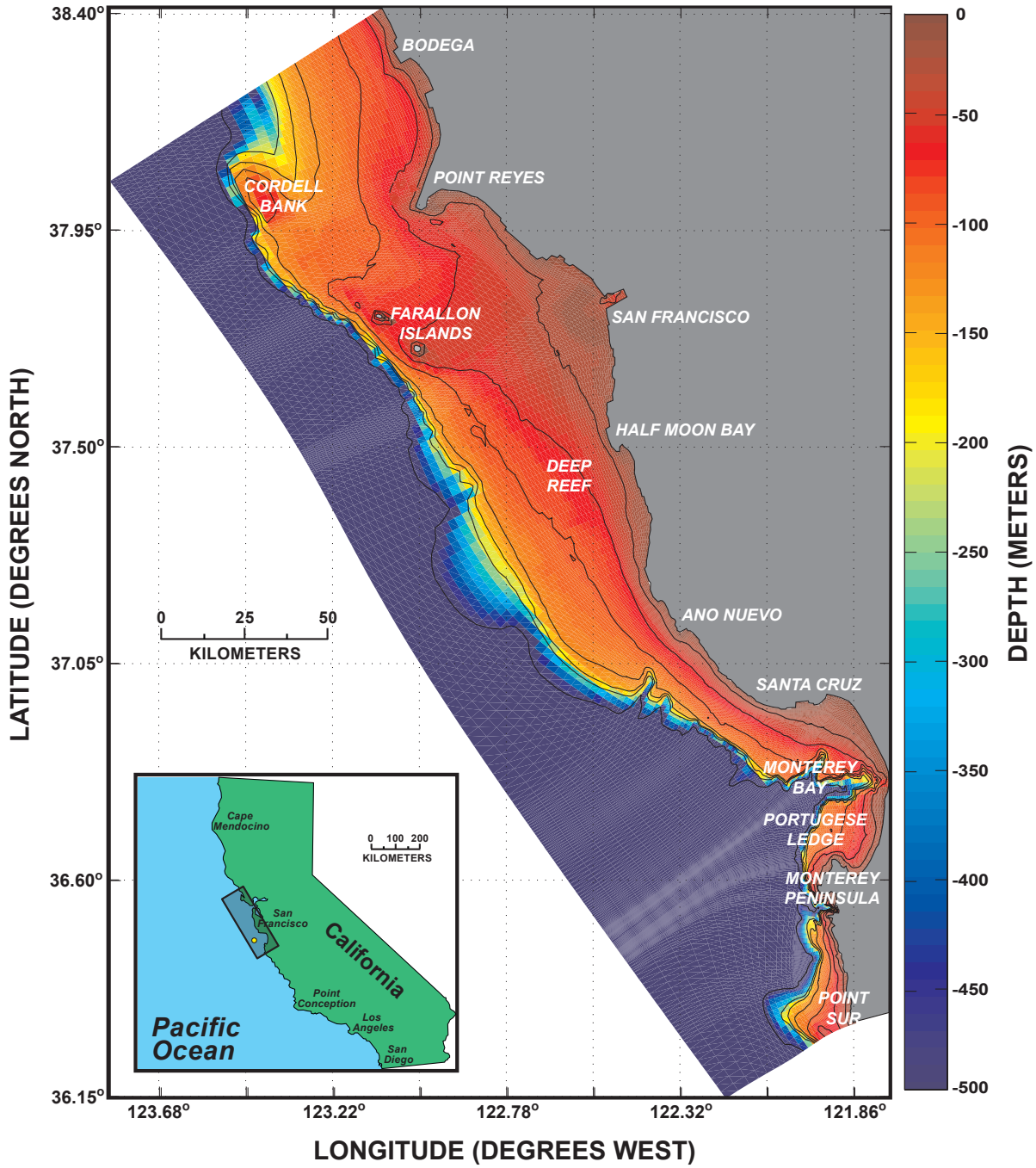

Figure 1. Map of the study area showing location names discussed in the text and the bathymetry of the model domain, which includes the shelf and upper slope down to depths of 500 m. The 30-m, 60-m, 90-m, 120-m, 150-m, 200-m, and 500-m isobaths are shown. Inset: Map of California, showing the locations of the study area and the NOAA National Data Buoy Center buoy (yellow dot) used in this study.

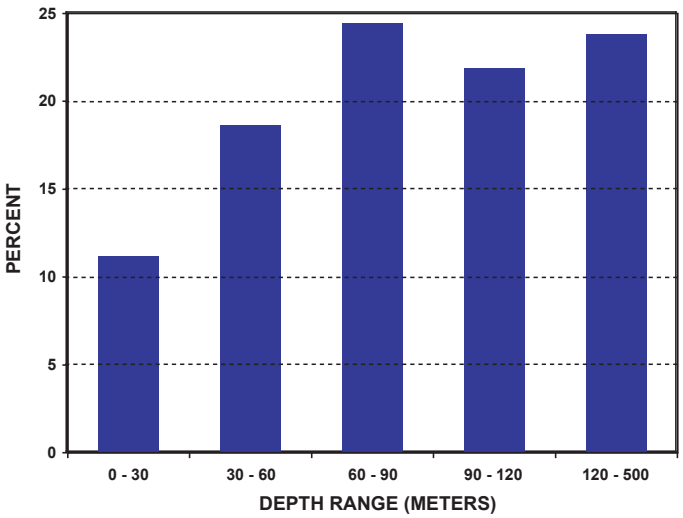

Figure 2. Distribution of bathymetry by depth range for the model domain down to 500-m water depth.

a rugged coastline characterized by a narrow continental shelf and coastal mountains cut with high seacliffs and narrow river valleys. The continental shelf, defined here as extending from the shoreline out to the 120-m isobath, varies significantly in width along the study area, ranging from more than 50 km off San Francisco to less than 1 km off of the Monterey Peninsula; although spatial area on the upper shoreface (depths 0-30 m) is narrow relative to the rest of the shelf, in general the distribution of shelf area by depth in the study area is relatively uniform (fig. 2).

The general offshore wave climate of California is characterized by four regimes (fig. 3): North Pacific swell, Northwest wind waves, Southern swell and local wind waves (National Marine Consultants, 1960; Storlazzi and Wingfield, 2005). The North Pacific swell is caused by extra-tropical lows and cold fronts in the North Pacific that generate long-period (T_{dom}) swell that impacts the study area from the west and northwest, with a general wave direction (WV_{dir}) of azimuth 290° and a WV_{dir} range of azimuths 210° to 330°. These waves have significant wave heights (H_{sig}) of 2 to 10 m and T_{dom} of 10 to 25 s, with the largest H_{sig} and longest T_{dom} during the winter (October-May). Northwest wind waves are generated by winds driven by the California High blowing over the open ocean and insolation-driven sea breezes that generate short T_{dom} waves; these waves impact the study area from the northwest, with a general WV_{dir} of azimuth 310° and a WV_{dir} range of azimuths 280° to 350°. Northwest wind waves have H_{sig} of 1 to 4 m and T_{dom} of 3 to 10 s. Although they occur throughout and common geochemical and geophysical parameters. It holds separately lab-determined numerical data ("extracted" or "EXT"), numerical data based on written descriptions ("parsed" or "PRS"), and estimated values for selected parameters from incompletely reported data ("calculated" or "CLC"), as given in existing publications, unpublished reports, theses, gray literature, and other unpublished data.

One prominent use for usSEABED data is in a regional view of sediment, rock, and biological information in areas without a single regional sampling regime such as the ones presented in this report. Several factors about usSEABED and extrapolation of its data in such a regional view should be considered in order to understand the inherent limitations of the resulting coverage.

The sediment grain-size data were derived from 32 original sources including those noted above, and are primarily from

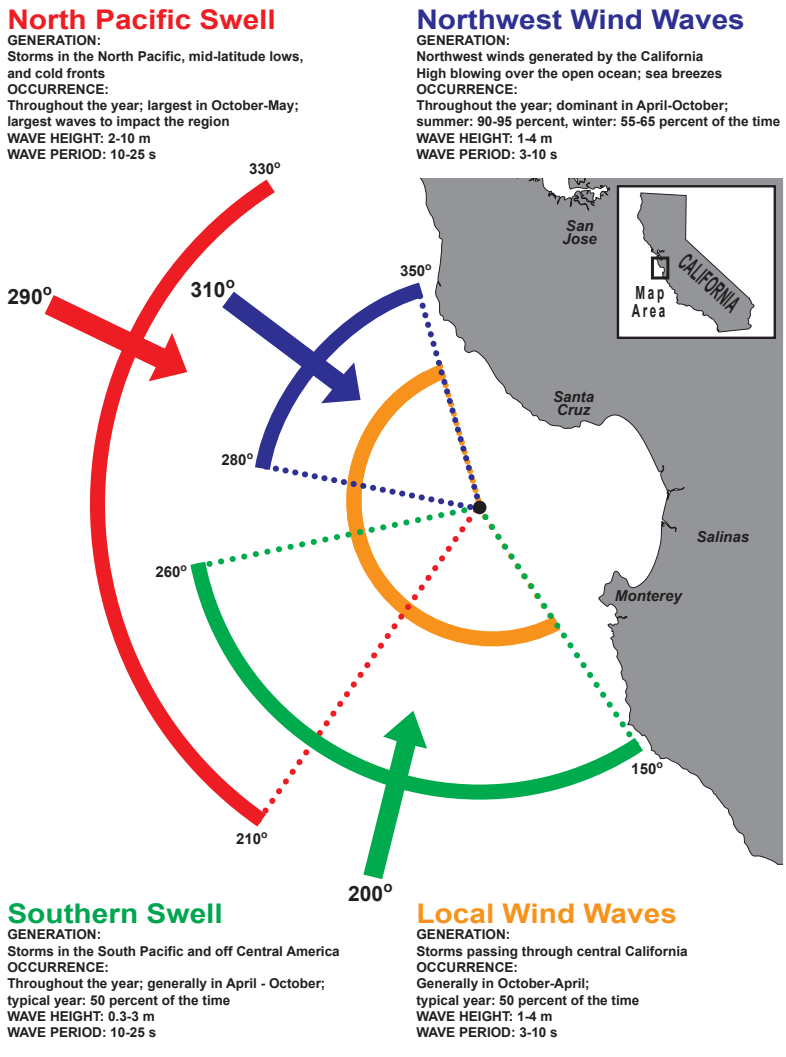

Figure 3. Wave rose for central California showing the four dominant wave patterns that impact the study area. Arcs show the range of direction for a given wave pattern, whereas arrows show the mean direction for a given wave pattern. Modified from Storlazzi and Wingfield (2005).

the year, they occur most consistently (90-95 percent of the time) from April to October and less frequently (55-65 percent of the time) in the winter. Southern swells are driven by storms in the South Pacific and off Central America that generate long T_{dom} waves that impact the study area from the south and southwest, with a general WV_{dir} of azimuth 290° and a WV_{dir} range of azimuths 150° to 260°. These waves have H_{sig} of 0.3 to 3 m and T_{dom} of 10 to 25 s. Although they occur throughout the year, they occur most consistently and with the largest H_{sig} from April to October when large storms occur in the South Pacific during the Southern Hemisphere's winter and when tropical cyclones develop off Central America. Local wind waves are driven by storms passing through central California that generate short T_{dom} waves that can impact the study area from all orientations, depending on the latitude of the storm's track. These waves have H_{sig} of 1 to 4 m and T_{dom} of 3 to 10 s; they are most frequent in the winter months (October-May).

Methods

Sediment Cover of the Central California Continental Shelf

Several regional and site-specific studies have investigated the surficial sediment along the central California Continental Shelf. Edwards (2002) presents detailed work in the Monterey Bay National Marine Sanctuary (MBNMS) and gives detailed descriptions of the locations, characteristics, and variabilities within the mid-shelf 'mud-belt'. He also describes the well-sorted, unimodal, generally very fine sand (0.125-0.063 mm) except near the San Lorenzo River mouth where they are polymodal, fine (0.250-0.125 mm) to very fine sand, along the nearshore, and slightly finer, less well-sorted, very fine sands along the shelf edge.

North of the MBNMS, Moore (1965), Schatz (1965), and Maher and others (1991) provide the largest published studies of the area between the Golden Gate and the Farallon Islands. The two earlier reports describe the ebb-tidal delta near the Golden Gate generally as medium (0.500-0.250 mm) to fine sands, fining outward to very fine sands. Maher and others (1991) describes the sediments east of the Farallon Islands as pockets of coarse (1.000-0.500 mm) and medium sand in a field of fine sand, with an overall coarsening trend towards the islands. Most of the samples reported by Maher and others (1991) have very little mud or gravel; however, a few scattered samples record as much as 65 percent as gravel-sized particles. These researchers also note a "tongue of silt" that curves around Point Reyes.

Data used to create the grain-size grids are from usSEABED, a U.S.-wide seabed characterization database, and are modified from the initial publication for the contiguous Pacific Coast (Reid and others, 2006). The usSEABED database, designed to provide point data for benthic habitat identification and geologic resource use, includes unified data on sediment size (gravel, sand, mud, clay) with standard statistical parameters, rock or seabed consolidation, constituent components, published and unpublished work by the USGS, the University of California at Berkeley Hydraulic Engineering Laboratory, and the U.S. Navy, with sampling dates generally from the 1960s to early 2000s (Reid and others, 2006). To gain the best coverage of the central California area, three data sets (EXT, PRS, and CLC) were combined and assumed the recorded subsample depths (here restricted to the upper 0.10 m of the sample) represent the water-sediment interface, regardless of sampler type. Rocks and rocky areas were excluded from the dataset, although rocky areas are well known along the nearshore area, the shelf edge, and in "Deep Reef" off Half Moon Bay (Eittreim and others, 2000, 2002; Orzech and others, 2001; Edwards, 2002; Reid and others, 2006; unpubl. usSEABED data).

The grain-size values in usSEABED are called "central" grain size; that is, determined from either the median (preferred) or mean values across the range of sediment analyzed or noted in a written description (see the FAQ section of Reid and others, 2006). For this work, where both a laboratory analysis and a written description of a sample exist, the EXT grain-size value was generally chosen; however, if the difference between the two was significant (>2 grain-size-class range), the original data were compared, modified as appropriate, or discarded. Modifications were usually due to the EXT value excluding noted larger objects, such as stones or shells. In these cases, the larger-object descriptors were combined with a verbal description of the granulometric analyses based on Folk and others (1970) ternary diagrams. The new description was reprocessed through dbSEABED, the processing software at the heart of usSEABED, to determine a better representative PRS grain-size value.

Of the resultant 3,438 data points used in the gridding, 90 percent were extracted from lab analyses (EXT) and are well distributed throughout the region (fig. 4, inset). PRS values contribute about 7 percent, and were primarily on Cordell Bank across the shelf to Point Reyes, east of the Farallon Islands, along the shelf edge, or well distributed throughout the shelf south of San Francisco. The remaining 4 percent of the data were calculated (CLC) from reported values for gravel, sand, silt, and clay fractions, and are located off northern Point Reyes or south of the Monterey Peninsula. Work by Field and others (1992) and Eittreim and others (2002) confirm the approximate grain sizes in the latter two areas, respectively.

Using solely the modified usSEABED-supplied ungridded data, approximately 57 percent of the Continental Shelf and upper slope down to 500 m in the study area is dominated by fine and very fine sand. Approximately 22 percent of the samples show coarser sediment, although current sampling locations, inherent limitations on sampling, and laboratory-induced bias towards finer sediment may under represent this value. Cordell Bank, for example, is notably underrepresented in usSEABED; sampling sediment much larger than pebbles in localities that may be part of the excluded rock or in rocky areas is difficult; pebbles and larger objects including shells may be discarded before laboratory analysis. The mud belts along central California consist primarily of silts with some clay (Edwards, 2002; Reid and others, 2006) and represent about 21 percent of the samples held in usSEABED for the area.

Gridded Coverage of Sediment Grain Size

The sediment grain-size grids shown here are considered preliminary and should not be used beyond the scope of this report. The gridding technique used (inverse-distance weighted [IDW] nearest-neighbor method provided by ESRI® ArcMap) forces coverage in areas of sparse or no data and ignores at least two notable issues. First, the spatial distribution of points varies from less than 0.2 km in the nearshore area off Santa Cruz to 12 km off northern Point Reyes (fig. 4, inset). This

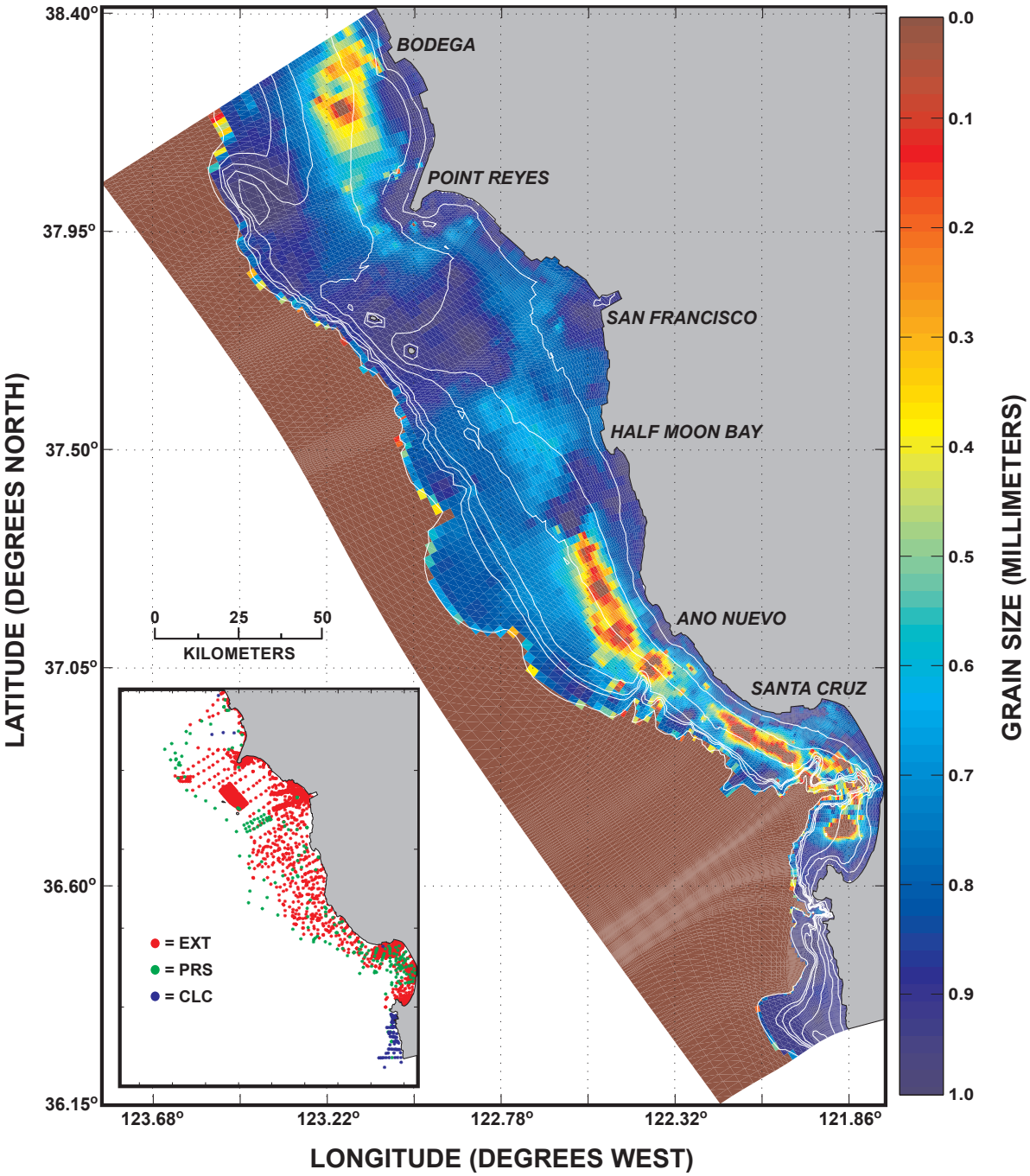

Figure 4. Grid of central grain-size data from the upper 0.1 m of the sediment cover on the central California Continental Shelf, using data modified from Reid and others (2006), presented in mm, for the model domain. Warm colors indicate areas of finer grained sediment. Gridded using Inverse Distance Weighting (IDW) method at 100-m grid-cell size with a variable radius and 12 nearest neighbors. Inset: Sample distributions along the central California coast from Reid and others (2006). Localities with extracted (EXT, laboratory analyses) data in red, with parsed (PRS, numeric data from written descriptions) data in green, and with calculated values (CLC, derived from incompletely reported data) in blue.

wide range in data spacing is because the data in usSEABED is derived from a number of disparate, noncoordinated sampling efforts spanning multiple decades. The grid cell size of 100 m was chosen to match the resolution of the wave data, and every cell may not have the same number of representative sediment samples or may lack a sample entirely.

Secondly, water depth is not included as a variable during the gridding process. Because water depth is an important

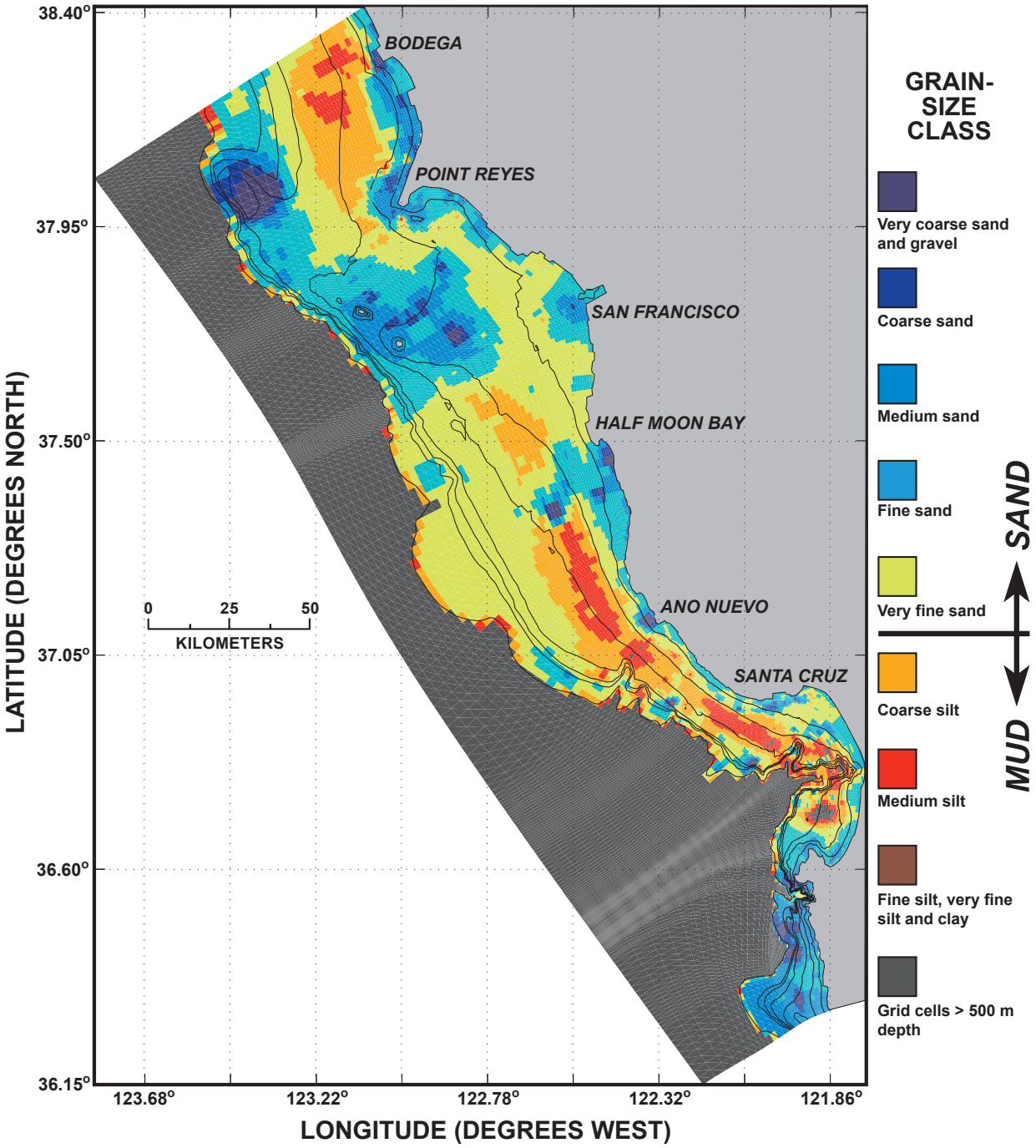

Figure 5. Grid of central grain-size data from the upper 0.1 m of the sediment cover on the central California Continental Shelf, using data modified from Reid and others (2006), presented by grain-size class (Wentworth, 1922). Note mid-shelf "mud belts" (orange and yellow) in pockets off Bodega, due west of Half Moon Bay, along much of the shelf south of Half Moon Bay as well as within Monterey Bay. Gridded using Inverse Distance Weighting (IDW) method at 100-m grid-cell size with a variable radius and 12 nearest neighbors.

factor in sediment deposition, erosion, and transport, the sediment patterns presented here are approximate. In particular, along areas of high bathymetric relief, such as the shelf edge or canyon breaks, the sediment patterns are poorly constrained in this gridded coverage. Caution should be used in using this coverage to strictly predict sediment grain size within one Udden-Wentworth class (Wentworth, 1922) at any given site.

Two gridded coverages are presented here to show the best estimate of sediment distributions along central California as modified from Reid and others (2006). Figure 4 presents a smooth continuum of surficial sediment grain size from 0.001 mm to more than 1.000 mm as used in the mobility model. Warmer colors show the areas of finer deposits in generally elongated pockets off Bodega and along the mid-shelf south of "Deep Reef" in water depths between 60 and 100 m.

Figure 5 presents the same data in textural categories of gravels, sands, silts, and clays. This figure shows the same mud belts (primarily coarse and medium silts) as figure 4 (here in orange, red, and brown) and emphasizes the coarse-silt dominated mud-belt pocket noted by Edwards (2002) north of "Deep Reef". Coarser sediments are found adjacent to San Francisco, surrounding the Farallon Islands, between Half Moon Bay and "Deep Reef", and in many areas along the near shore. Coarser sediments are also suggested along the outer shelf near the Farallon Islands north to the pebbly deposits of Cordell Bank and as relict deposits along the shelf edge (Edwards, 2002). Along the nearshore and the shelf break between Año Nuevo and Point Sur, some areas depicted here as fine to coarse sands roughly correlate with locations of rocky outcrops or relict gravels shown in backscatter imagery (Chin and others, 1988; Eittreim and others, 2000, 2002 and references therein; Anima and others, 2002); the size differences may be due either to thin sediment cover or to sampling bias against larger particles.

The IDW grid suggests that more than 75 percent of the central California Continental Shelf shallower than 500 m is covered by sand, with approximately 21 percent covered by mud (fig. 6*A*). Medium sand to silt dominate the shelf, with fine sand to very fine sand accounting for approximately 60 percent of the sediment (fig. 6*B*). A comparison of samples and the resulting grid suggests that areas of very fine sand are underrepresented in usSEABED.

Wave Data

Since the early 1980s, the NOAA National Data Buoy Center (NDBC) has deployed several buoys off the U.S. coast to monitor various oceanographic and atmospheric conditions. Data from the NDBC Monterey buoy (ID no. 46042) online data archive were used; these data are available online (National Data Buoy Center, 2006). This buoy, first deployed in December 1987, records hourly data for various oceanographic and meteorologic parameters, including significant wave height (H_{sig}), dominant wave period (T_{dom}), dominant wave direction (WV_{dir}), wind speed (WD_{spd}), and wind direction (WD_{dir}). The Monterey buoy did not obtain directional wave capability until July 1991. More than 150,000 hourly observations per parameter were extracted for the 07/1991–12/2005 time period investigated in this study.

The average time between events of a given magnitude can be estimated using extreme value statistics (Carter and others, 1986). For example, a 2-year recurrence interval for H_{sig} suggests that the probability of an occurrence of a given extreme value in any given year is 50 percent. The inverse of the recurrence interval is the probability of such an occurrence of a parameter's value equaling or exceeding the given extreme value. Return magnitudes were based on Fisher-Tippet type I distributions (Carter and others, 1986) of monthly maxima, and 2-, 10-, 50-, and 100-year return-magnitude projections were calculated for H_{sig}, T_{dom} and WD_{spd} (table 1). Note that these projections are for a maximum observed wave height for a given return period and thus might only be observed for one hour, as compared to the greater durations calculated for the monthly data discussed below.

The El Niño-Southern Oscillation (ENSO) cycle is an interannual phenomenon composed of episodic El Niño and La Niña climatic events at 2- to 7-year intervals. The multivariate ENSO index (MEI), devised by Wolter and Timlin (1998), incorporates multiple factors to give a weighted average of the main oceanic-atmospheric ENSO-related features. In addition to sea-level barometric pressure, other variables include sea-surface water temperature, surface air temperature, total cloudiness, and zonal (north-south) and meridional (east-west) components of surface winds. Negative values of the MEI (fig. 7) represent cold ENSO phases (La Niña), and positive values represent warm ENSO phases (El Niño).

To understand how these oceanographic and meteorologic parameters are influenced by ENSO events, we broke down the monthly statistics into three categories based on the corresponding MEIs for each specific month—all months of the study period, El Niño months, and La Niña months. Monthly MEIs before 1993 were normalized to an average MEI of 0.0 and a standard deviation of 1.0 (National Oceanic and Atmospheric Administration, Climate Diagnostics Center, 2006). Cutoff MEI values were used to separate index values of El Niño, La Niña, and "Normal" months, that is months when neither intense El Niño nor intense La Niña conditions were observed. In this case, all months with an MEI > 1.0 were defined as El Niño months (39 out of 174 total months [22.4 percent]); months when the MEI < -0.5 were defined as La Niña months (27 out of 174 total months [15.5 percent]); and months with –0.5 < MEI < 1.0 were defined as Normal months (108 out of 174 total months [62.1 percent]). These subsets, in conjunction with the high temporal resolution and long duration of data collection, made it possible to make statistically significant projections of each parameters' behavior under each of the three climatic conditions.

Because the MEI data are at a resolution of one month, it was necessary to compile the wave and wind data at a monthly rate to make meaningful conclusions on the nature of their temporal variability under the different climatic conditions. Because the ultimate goal was to understand if the seabed was

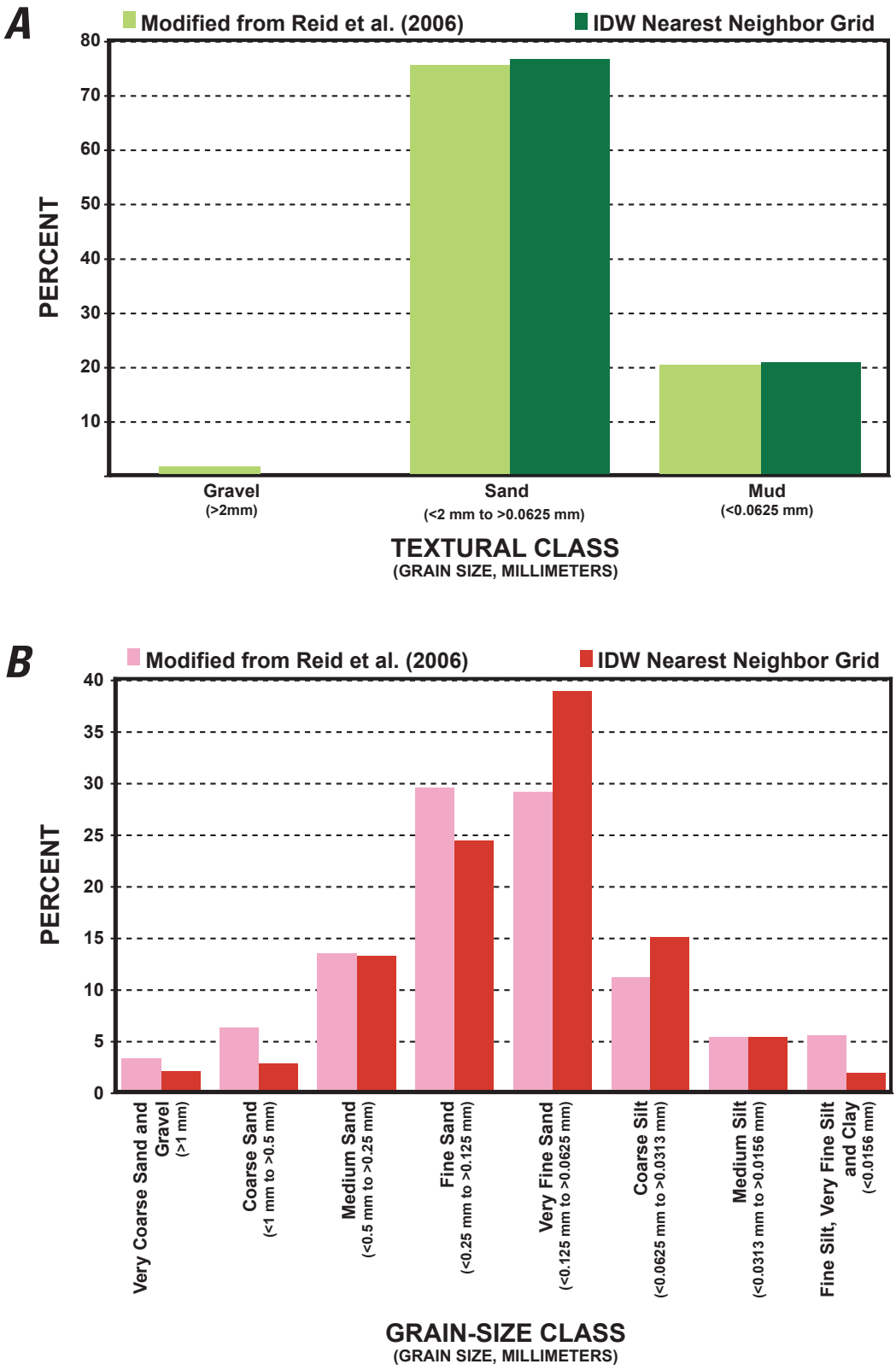

Figure 6. Histograms of surficial sediment distributions (upper 0.1 m) from gridded coverage of the Continental Shelf between Bodega and Point Sur, presented by grain-size class (Wentworth, 1922). Areas of rocky outcrops are excluded. *A*, Relative percentages of textural classes show the dominance of sand in the modeled domain. *B*, Relative percentages of single classes over the same area suggest that fine and very fine sand covers nearly 60 percent of the Continental Shelf along central California.

Table 1. Monthly climatic model run boundary conditions.

[H_{sig}, Significant wave height; T_{dom}, Dominant wave period; WV_{dir}, Wave direction; WD_{spd}, Wind speed; WD_{dir}, Wind direction]

RUN ID	Climate	Month	H_{sig} (m)	T_{dom} (s)	WV_{dir} (deg)	WD_{spd} (m/s)	WD_{dir} (deg)
N01	Normal	Jan	6.1	15	277	10	287
N02	Normal	Feb	6.6	14	288	10	294
N03	Normal	Mar	6.1	15	298	9	305
N04	Normal	Apr	4.5	14	303	11	320
N05	Normal	May	4.2	12	306	11	321
N06	Normal	Jun	4.3	10	310	10	319
N07	Normal	Jul	3.8	9	314	10	322
N08	Normal	Aug	3.3	9	311	9	323
N09	Normal	Sep	3.8	9	311	9	319
N10	Normal	Oct	4.3	12	302	8	320
N11	Normal	Nov	5.6	14	302	10	318
N12	Normal	Dec	6.0	15	295	10	274
E01	El Niño	Jan	6.5	15	273	5	252
E02	El Niño	Feb	7.5	14	276	9	274
E03	El Niño	Mar	6.2	15	288	8	303
E04	El Niño	Apr	4.9	13	300	9	325
E05	El Niño	May	3.9	11	305	11	324
E06	El Niño	Jun	4.5	11	307	8	322
E07	El Niño	Jul	4.0	9	314	7	322
E08	El Niño	Aug	3.3	9	313	7	323
E09	El Niño	Sep	3.8	9	308	7	319
E10	El Niño	Oct	4.3	12	300	4	326
E11	El Niño	Nov	5.5	13	297	4	319
E12	El Niño	Dec	6.4	14	292	6	283
L01	La Niña	Jan	5.7	15	280	9	281
L02	La Niña	Feb	5.9	14	299	9	309
L03	La Niña	Mar	6.0	15	299	10	316
L04	La Niña	Apr	4.1	14	306	11	315
L05	La Niña	May	4.4	12	307	10	313
L06	La Niña	Jun	4.1	10	316	7	316
L07	La Niña	Jul	3.7	9	314	10	322
L08	La Niña	Aug	3.3	9	311	10	323
L09	La Niña	Sep	3.9	10	312	8	317
L10	La Niña	Oct	4.4	12	306	8	312
L11	La Niña	Nov	5.8	15	306	11	310
L12	La Niña	Dec	5.7	15	297	8	289

being mobilized or not by surface waves during any given month, it was decided that the most useful statistical scenario would be the largest sustained wave height, in that a wave height that was observed for a minimum period of 7 hours each month rather than just the maximum wave height for a given month. This choice was made for two reasons. First, if a given wave height was only observed for 1 hour (actually one 20-minute period when the sensors were collecting data that hour), it might not be long enough in duration for the sea-floor sediment to be fully entrained by the surface wave orbital motions. Second, the 7-hour duration could be compiled statistically, being the mean plus three standard deviations from the 720 hours of wave data each month, which is statistically the mean of the top 1 percent of wave heights each month. For each climatic subset, monthly means, standard deviations and top one percent (mean + three standard deviations) statistics for the H_{sig} data were computed; monthly mean T_{dom}, WV_{dir}, WD_{spd}, and WD_{dir} that corresponded to these times of the top 1 percent of highest waves were also compiled (fig. 8; table 2).

Wave Modeling

Monthly statistics of NDBC buoy data (H_{sig}, T_{dom}, WV_{dir}, WD_{spd}, and WD_{dir}) provided boundary input to the Delft3D version 3.25.01 (Delft, 2006) SWAN wave model (Holthuijsen and others, 1989; Ris, 1997; Booij and others, 1999; Ris and others, 1999). SWAN is based on the discrete spectral action balance equation and is fully spectral in all directions and frequencies. This third-generation wave model incorporates wind-wave growth, whitecapping, quadruplets, frequency shifting, and nonlinear triad interactions. The model also incorporates shallow-water wave effects such as depth-induced breaking, refraction and JONSWAP (Hasselmann and others, 1980) bottom friction (C_d = 0.067). The frequency space was set from 0.04-1.00 Hz in 25 frequency bins with a standard deviation of 20 degrees in directional spreading. Parametric specification of the spectra used a JONSWAP shape with a 3.3 peak enhancing factor. The model domain extends from the shoreline out ~100 km into water depths greater than 2,000 m (fig. 9). The model grid cells are small and more densely spread in shallow water and around complex bathymetry so that the model can accurately handle wave refraction in shallow water.

Threshold for the Initiation of Sediment Transport

The SWAN wave model was used to calculate H_{sig}, T_{dom}, and WV_{dir} data for the entire model domain (fig. 10). From these data, the dispersion equation was solved iteratively to determine the wave number (k) and the radian frequency (σ), which were then used to solve the near-bed horizontal wave orbital velocity (u, fig. 11) via Stokes second-order waves theory (see for example, Komar, 1998). Grain roughness (r) was defined following Nielsen (1979) as 2.5 times the mean grain diameter, which varied spatially according to the usSEA-

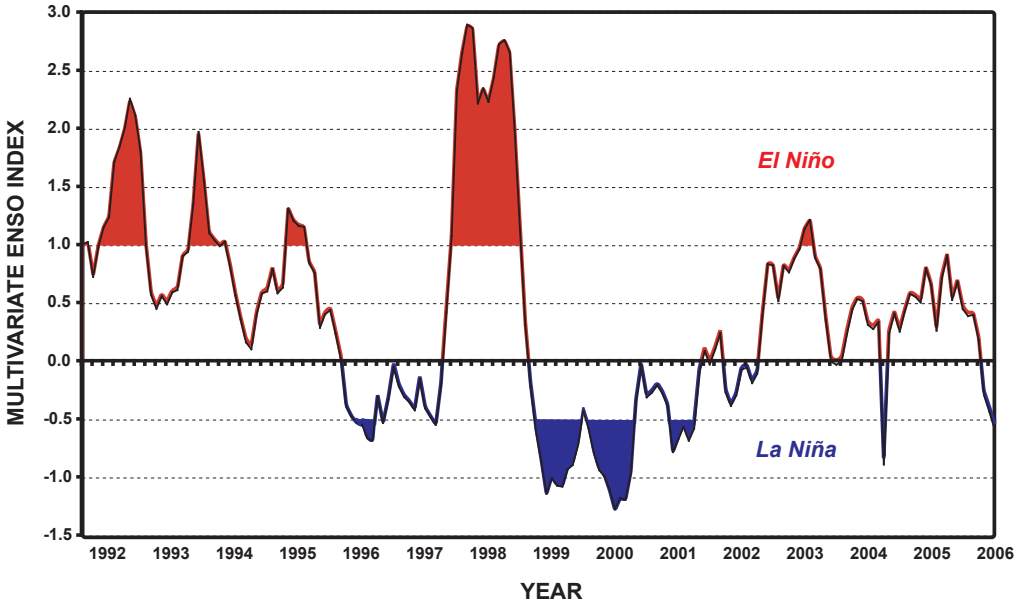

Figure 7. Multivariate El Niño-Southern Oscillation (ENSO) index (MEI; NOAA, 2006) during the time period when high-resolution direction wave and wind information for the study area were available. Red regions denote months with El Niño conditions, blue regions denote months with La Niña conditions, and the remaining months are classified as those with Normal conditions.

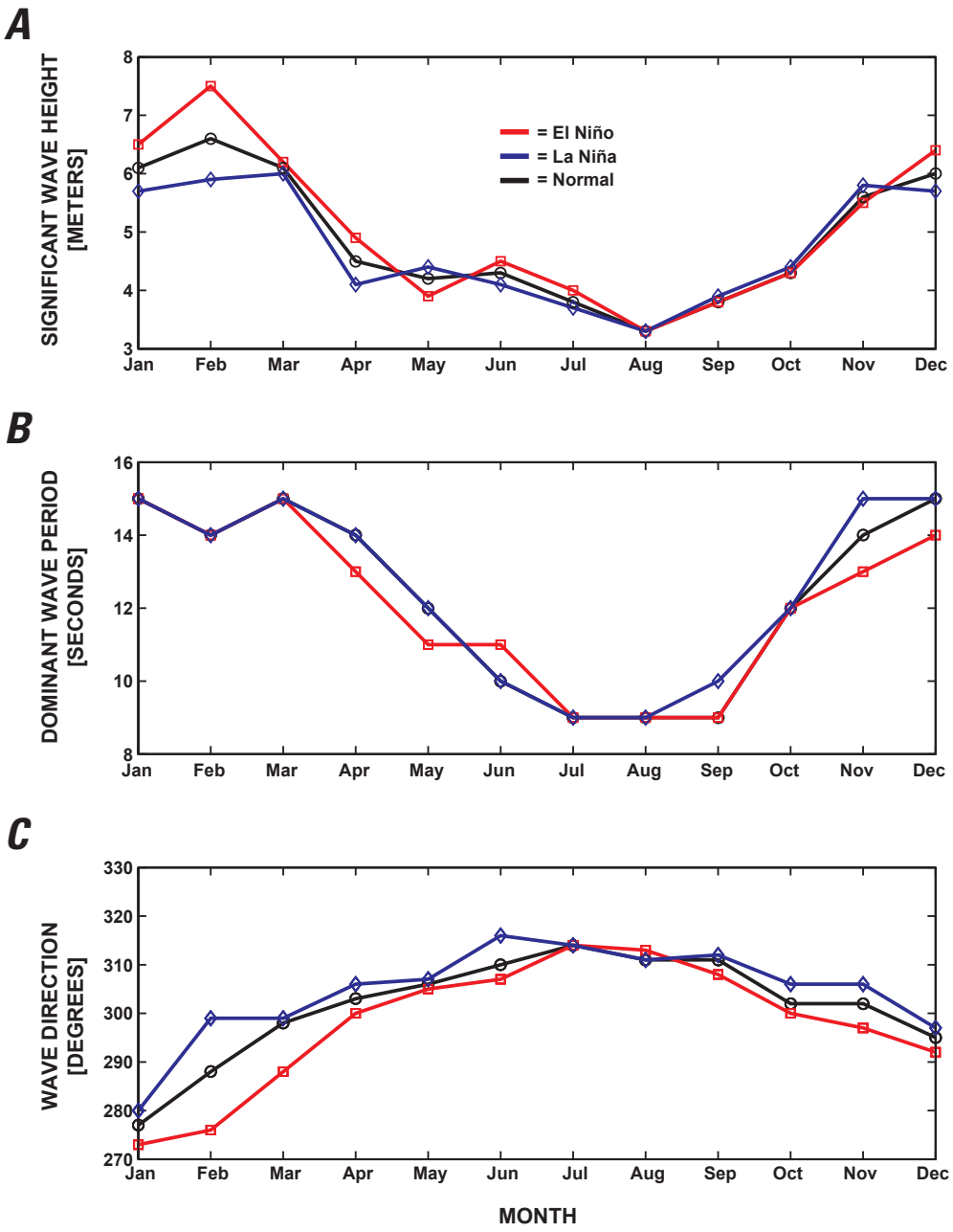

Figure 8. Temporal variability in the wave parameters for El Niño (red), La Niña conditions (blue), and Normal conditions (black) used as boundary input for the wave modeling. *A*, Top 1 percent (mean + 3 standard deviations) significant wave heights (H_{sig}). *B*, The corresponding monthly mean dominant wave periods (T_{dom}) for the top 1 percent wave heights. *C*, Mean wave directions (WV_{dir}) for the top 1 percent wave heights. The largest waves during La Niña events occur early in the winter (November), whereas the largest waves during El Niño events occur much later in the winter (February) and come from more westerly and southwesterly directions.

Table 2. Return interval model run boundary conditions.

[H_{sig}, Significant wave height; T_{dom}, Dominant wave period; WV_{dir}, Wave direction; WD_{spd}, Wind speed; WD_{dir}, Wind direction]

RUN ID	Return Interval (years)	H_{sig} (m)	T_{dom} (s)	WV_{dir} (deg)	WD_{spd} (m/s)	WD_{dir} (deg)
TWO	2	7.7	16	280	20	280
TEN	10	9.6	18	280	24	280
TFV	25	10.6	20	280	26	280
FIF	50	11.4	22	280	28	280
HUN	100	12.2	24	280	30	280

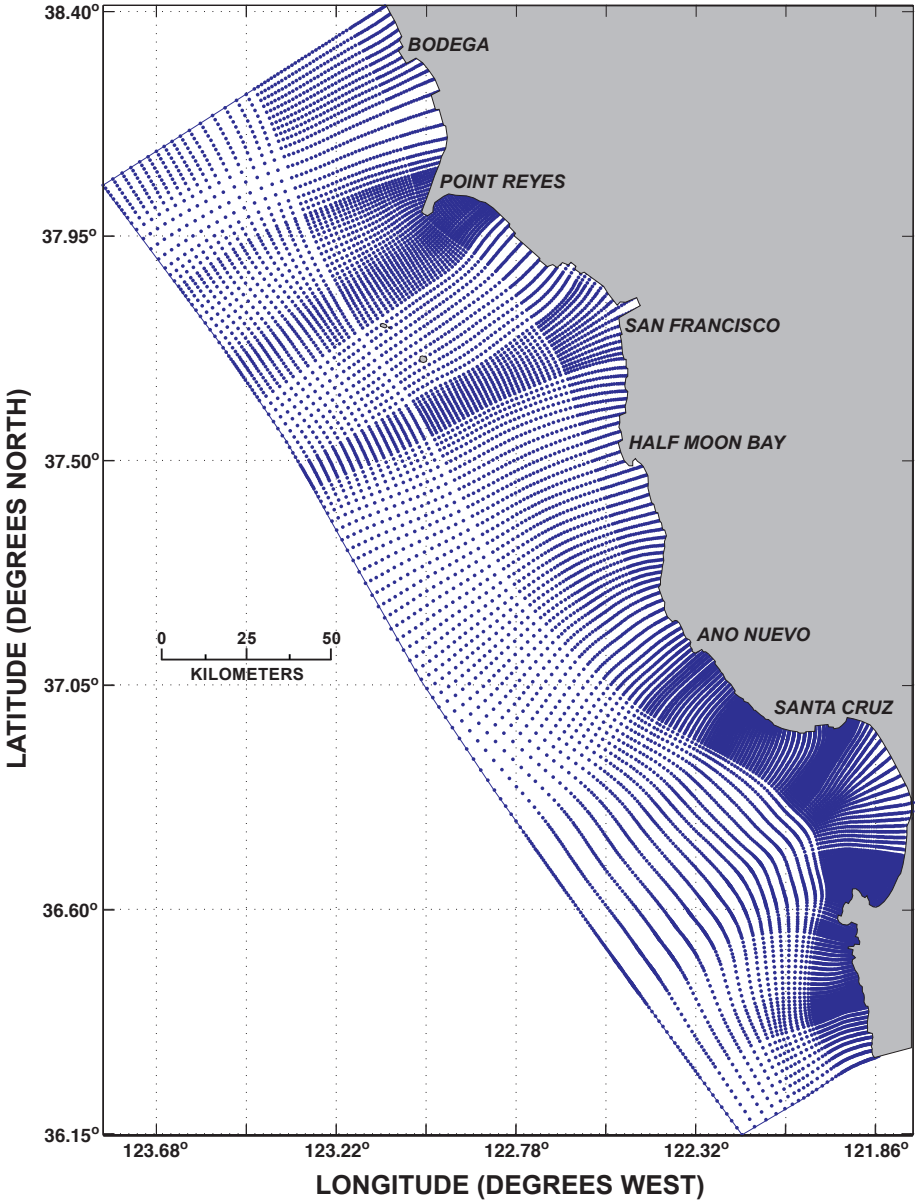

Figure 9. Delft3D curvilinear modeling grid for the study area, with dots denoting the grid cells vertices. The average cell size is approximately 100 m on a side. The grid extends out into deep (>1,000 m) water to propagate the wave field properly on to the upper slope and shelf. The higher density, and thus smaller cell size, of the grid on the shelf and upper slope was necessary for the model to accurately handle wave refraction in shallow water and around complex bathymetry.

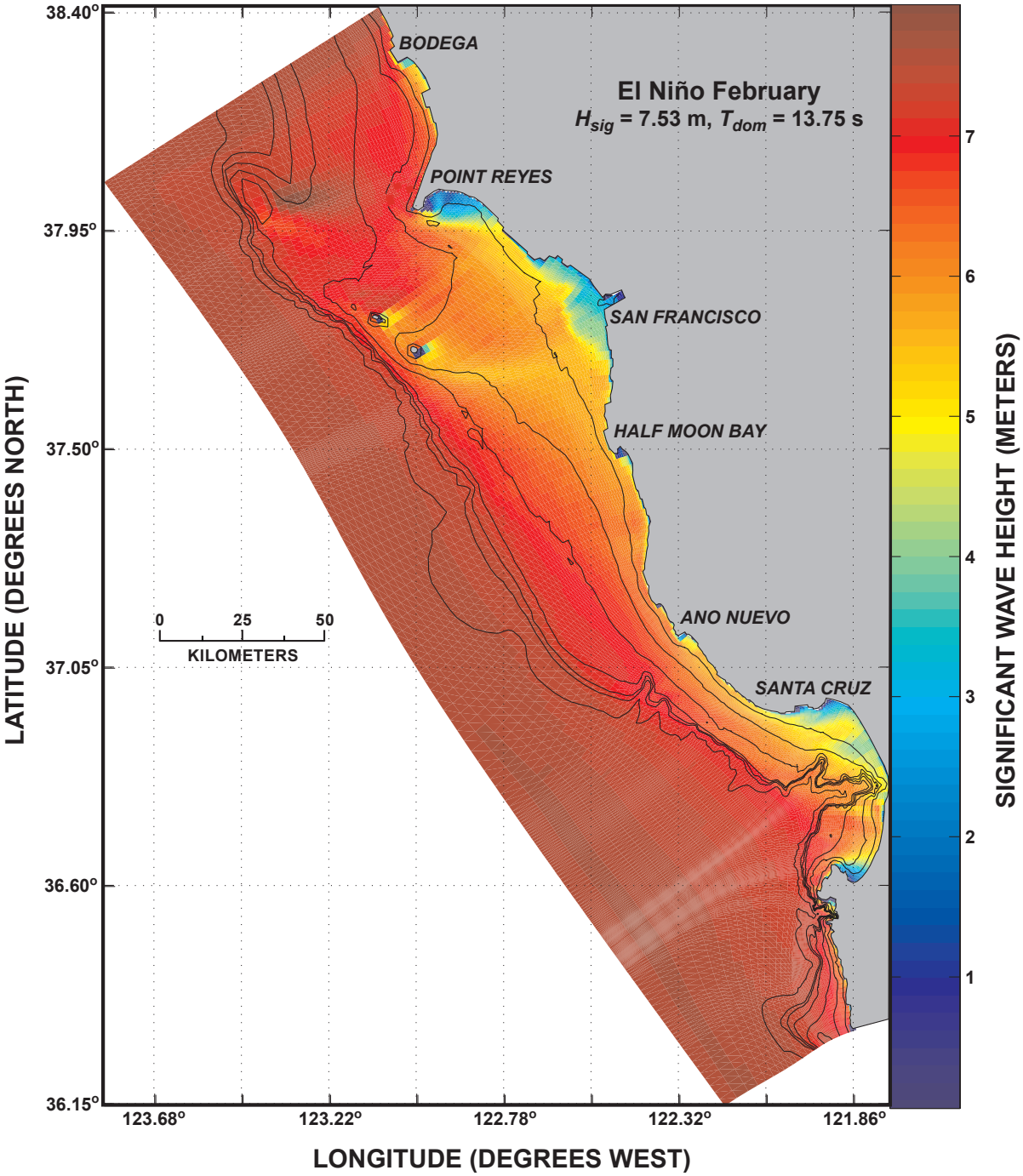

Figure 10. Example model run for the study area showing significant wave height (H_{sig}), in m, over the model domain for an El Niño February. Reduced wave heights are seen in the lee of the Farallon Islands, the ebb tidal delta off San Francisco, and the headlands at Bodega, Point Reyes, Half Moon Bay, Año Nuevo, Santa Cruz and Monterey. A subtle, but noticeable, decrease in wave heights across the shelf due to wave energy loss by frictional interactions with the sea floor is observed. The dominant wave period (T_{dom}) is 13.75 seconds.

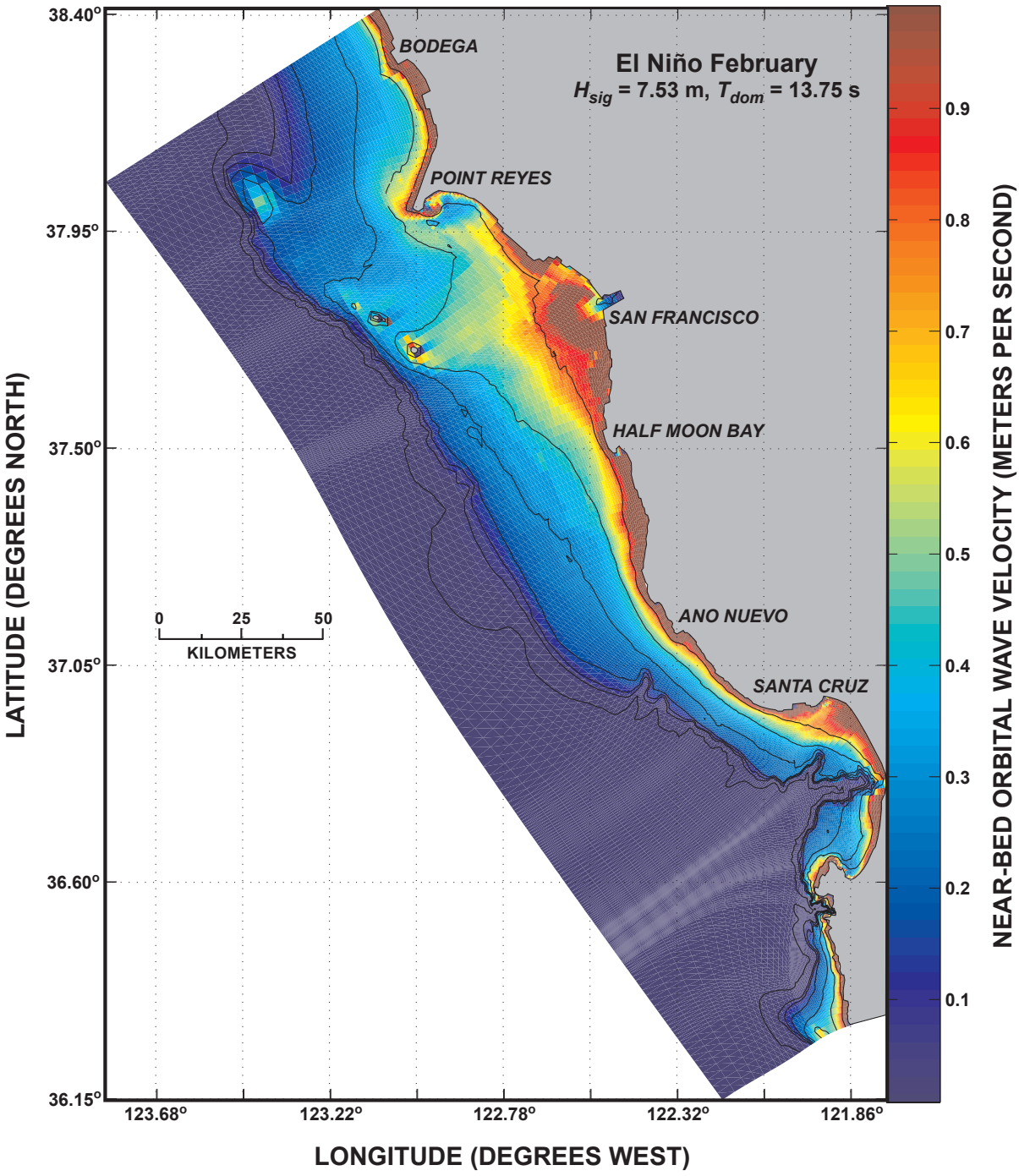

Figure 11. Same example model run shown in figure 10 displaying peak wave-induced near-bed orbital wave velocity (U_{orb}), in m/s, over the model domain for an El Niño February. The largest U_{orb} values are found in shallow regions where significant wave height (H_{sig}) is large, with substantial U_{orb} values observed all across the inner shelf and elevated U_{orb} values observed out to the shelf break in water depths exceeding 120 m. The dominant wave period (T_{dom}) is 13.75 seconds.

BED data. The wave friction factor, f_w, was defined using the Nielsen (1992) formulation:

$$f_w = \exp\left[5.5\left(\frac{r}{A}\right)^{0.2} - 6.3\right]$$

with the orbital amplitude excursion (A) defined as u/σ. The wave friction factor was then used to calculate the peak bed shear stress for oscillatory flow under waves (τ_{peak}) using the Fredsoe and Deigard (1992) formulation:

$$\tau_{peak} = \frac{1}{2}\rho_f f_w (A\sigma)^2$$

with p_f as the density of seawater (1,026 kg/m^3 at 34 PSU and 10 °C). These τ_{peak} values for each grid cell, in units of N/m^2 (fig. 12), were compared to the critical shear stresses for the initiation of sediment transport (τ_{crit}, fig. 13) calculated using the modified Shield parameter methodology of Madsen (1999) for each grid cell for the cell's grain size (fig. 4) and sediment density from the usSEABED database. If $\tau_{peak} < \tau_{crit}$, then the force per area applied by the waves is not great enough to mobilize the sea-floor sediment; if the $\tau_{peak} >= \tau_{crit}$, however, then the sea-floor sediment is entrained by the wave orbital velocities and thus the sea floor is mobilized. Because unidirectional currents are not being modeled, sediment fluxes, and thus the divergences or convergences that cause erosion or deposition of the sea floor cannot be computed. Therefore, these calculations can only determine if the seabed sediment is mobilized and entrained by the wave-orbital velocities and not provide information on sediment transport or depth of disturbance.

Since sea-floor sediment resuspension is driven by the total shear stress (wave + current) on the sea floor, these calculations, which only used the wave-induced shear stress, will likely under represent the true magnitude of sediment mobility on the outer shelf and upper slope due to the equal order of the magnitude of the wave-induced stresses and current-induced (internal, tidal or subtidal) stresses at these depths. Therefore, the results of this study will provide minimum forcing levels. The current-induced shear stresses and the resulting combined wave-current shear stresses in the study area will be addressed in subsequent reports.

Results

Examples of the influence of variations in oceanographic and meteorologic forcing on wave-induced sediment mobilization along the central California coast are shown in figures 14 and 15. Figure 14 displays regions of the study area that are mobilized (red) or are stable (blue) for the El Niño February model run shown in figures 10 through 12. The red regions indicate where the peak wave-induced near-bed shear stress (τ_{peak}, fig. 12) exceeds the critical shear stress for the initiation of sediment transport (τ_{crit}, fig. 13); the blue regions are where $\tau_{peak} < \tau_{crit}$. Almost the entire shelf, except for areas characterized by rock and boulders, is mobilized during an El Niño February due to the large H_{sig}, long T_{dom} and westerly WV_{dir}. Figure 15 displays which regions of the study area are mobilized (red) and which are stable (blue) during a La Niña October. La Niña Octobers are characterized by smaller H_{sig} and shorter T_{dom} than during an El Niño February, resulting in a much smaller proportion of the shelf mobilized (fig. 14).

Two general alongshore trends are visible in figure 15 that are common to many of the model runs. The first trend is a band of sediment mobility that extends from the shoreline out into water depths of 10 to 30 m. This region, although predominantly coarse (sand-sized) sediment (fig. 4), is commonly mobilized due to the shallow water depth relative to the H_{sig} and T_{dom}, resulting in τ_{peak} greater than the τ_{crit} for the sediment. Farther out on the shelf in water depths of 60 to 90 m, another region of finer-grained (silt and clay) sediment, termed the "mud belt," is more commonly mobilized than the coarser sediment in shallower water depths (30-60 m). Although the water depth is greater along the mud belt than the region of less frequent mobility inshore of it, the much smaller grain size lowers τ_{crit} and results in greater mobility than the shallower but coarser material inshore. The individual monthly model runs detailed in table 1 are shown in appendixes 1 through 36 and the return interval projections outlined in table 2 are shown in appendixes 37 through 41. The return interval projections suggest that the entire shelf (0-120 m) is suspended under these extreme events, and more than 97 percent of the entire study area shallower than 500 m is mobilized during a 100-year storm (table 3).

Modeled sediment mobility in the study area varies by depth range, but is also affected by location and time of year (fig. 16; table 4). Spatially, the shallower regions are generally more frequently mobilized than the deeper regions due to the dependence of τ_{peak} on water depth. Temporally, the greater storminess during the winter months (December–February) results in approximately 10 percent of the upper slope (120-500 m) in the study area being mobilized, whereas in the summer months (July-September) only 30 percent of the inner shelf (0-30 m) is mobilized by waves. During normal oceanic conditions, the regions with highest mobility occur along the inner shelf and the mud belt, and sections of the inner shelf with westerly exposures are more frequently mobilized than those with more southerly exposures due to wave energy loss resulting from wave refraction and energy dissipation (fig. 17).

ENSO events have a clear influence on sediment mobility along the central California shelf (table 4). Spatially, El Niño conditions cause greater mobilization on the upper slope (120-500 m) and the inner shelf (0-30 m), as shown in figure 18. Although 2 percent of the shelf between the 60 m and 90 m isobaths is more frequently disturbed during El Niño conditions than during Normal conditions (fig. 17), this relative increase in frequency of disturbance is offset by an almost equal decrease in frequency of disturbance throughout the rest of the shelf and upper slope in the study area. La Niña condi-

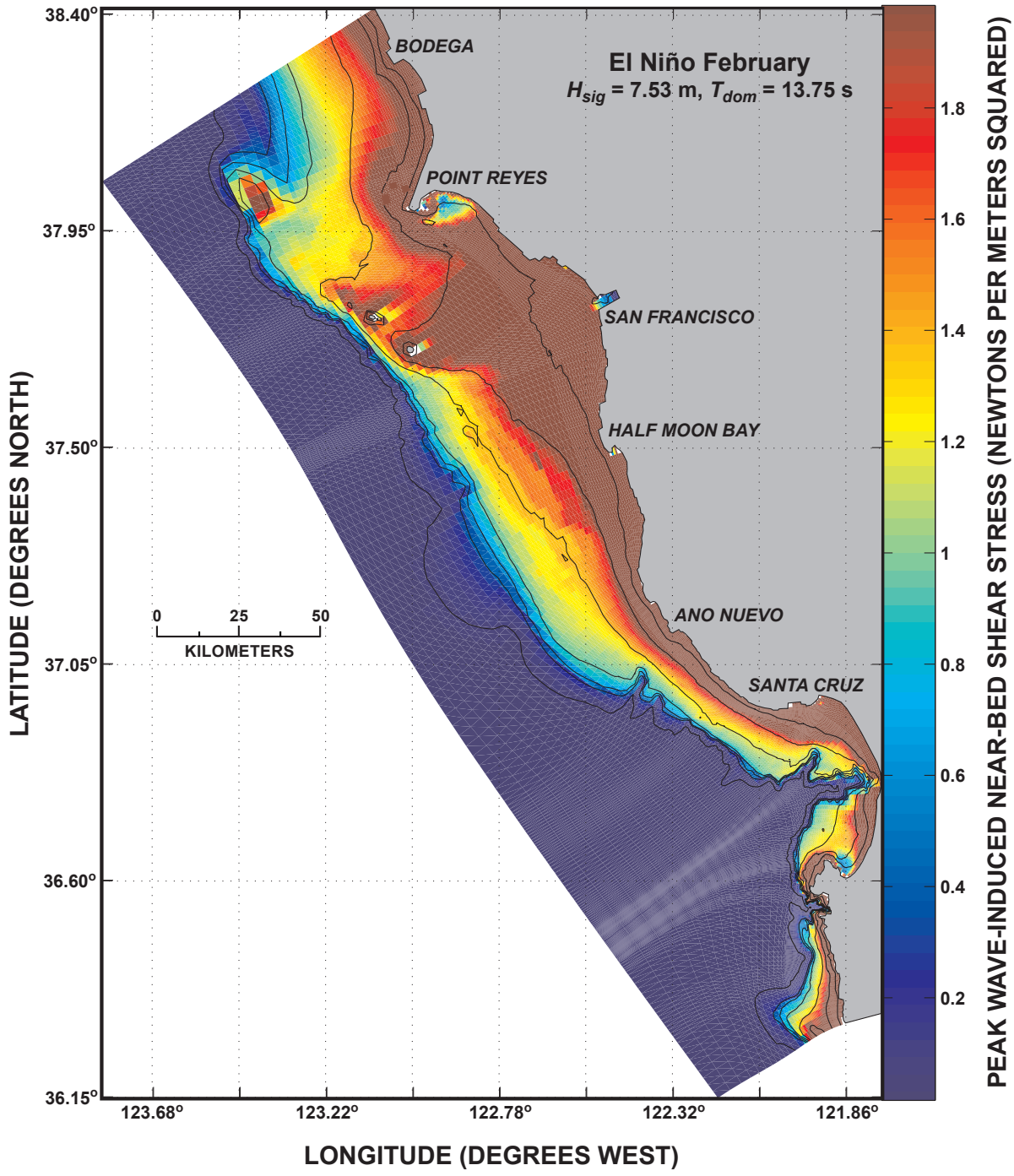

Figure 12. Same example model run shown in figures 10 and 11 displaying peak wave-induced near-bed shear stress (τ_{peak}), in N/m^2, over the model domain for an El Niño February. Substantial τ_{peak} values are observed all across the inner shelf and elevated τ_{peak} values are observed to the shelf break in water depths exceeding 120 m.

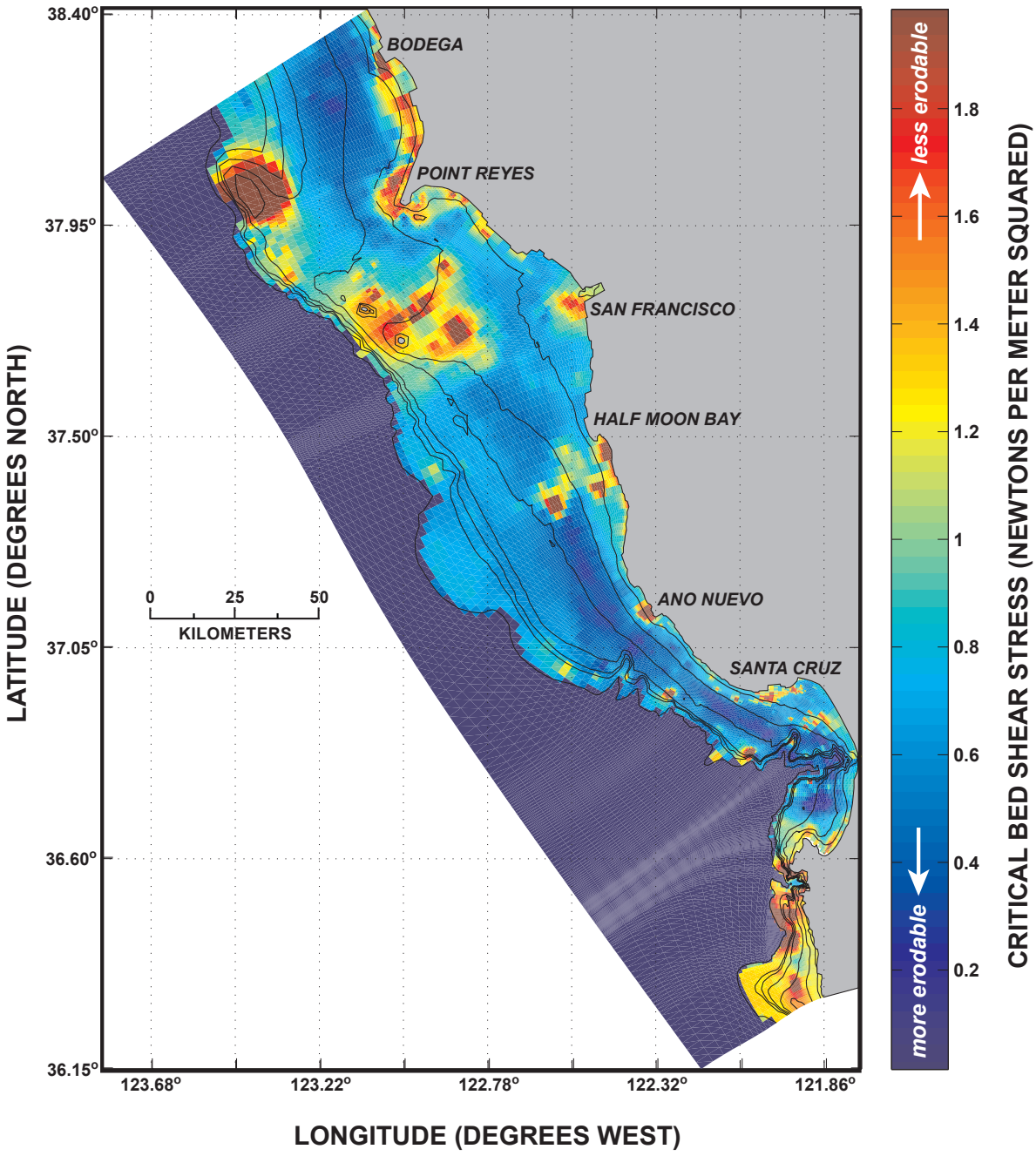

Figure 13. Critical shear stresses (τ_{crit}), in N/m^2, for the initiation of sediment transport in the study area calculated using the methodology defined by Madsen (1999) based on the grain size and sediment density from the usSEABED database. Sediments with higher critical shear stresses require greater force per area to mobilize and thus are less easily erodable.

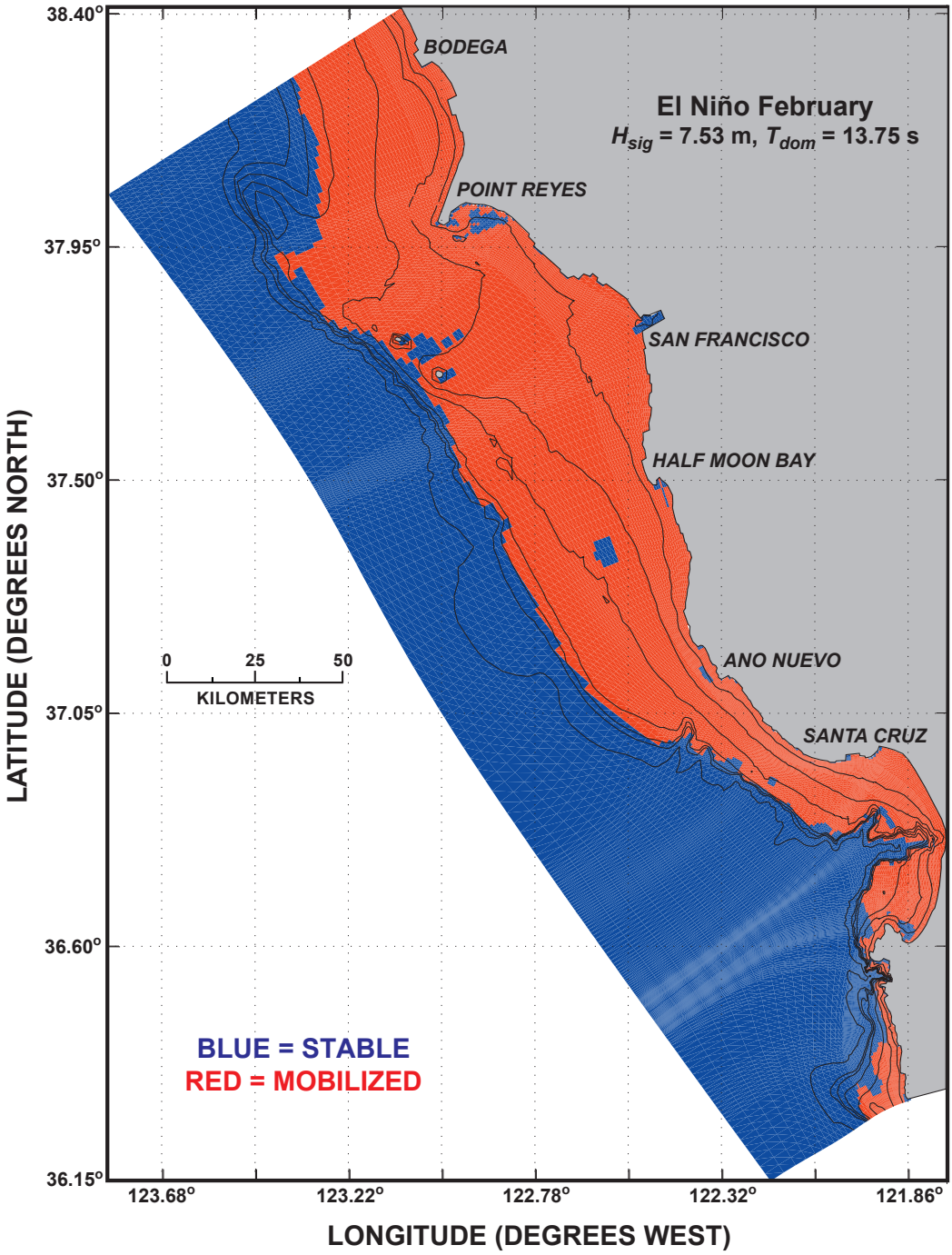

Figure 14. Same example model run shown in figures 10 through 12 displaying regions of the study area mobilized (red) and stable (blue) during an El Niño February due to wave forcing. The red regions are where the peak wave-induced near-bed shear stress ($\tau_{peak,}$ fig. 12) exceeds the critical shear stress for the initiation of sediment transport ($\tau_{crit,}$ fig. 13); the blue regions are where $\tau_{peak} < \tau_{crit.}$ Almost the entire shelf (depths <120 m), except for areas characterized by rock and boulders, is mobilized during an El Niño February. The significant wave height (H_{sig}) is 7.53 m and the dominant wave period (T_{dom}) is 13.75 seconds.

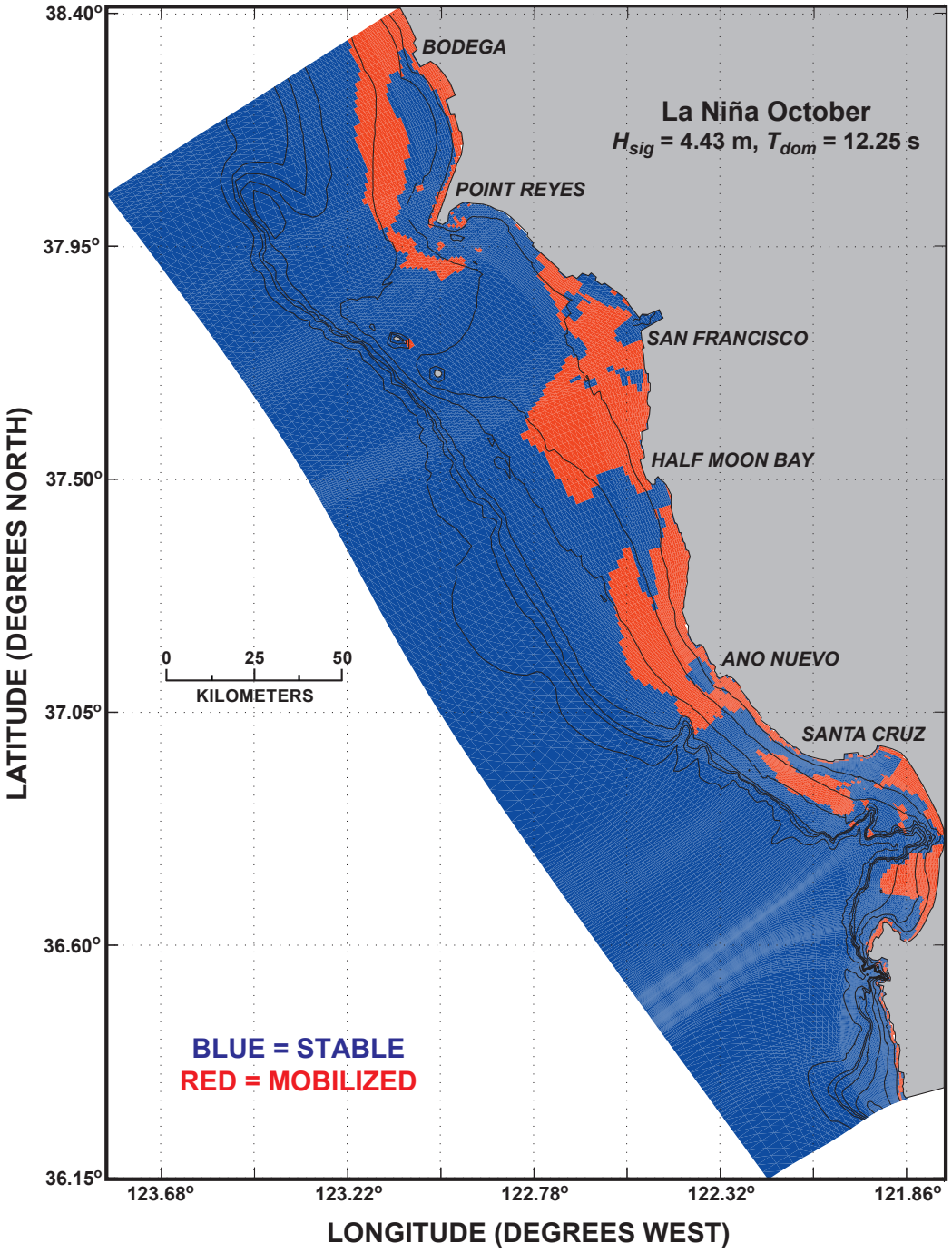

Figure 15. An example model run displaying regions of the study area mobilized (red) and stable (blue) during a La Niña October. The red regions are where the peak wave-induced near-bed shear stress (τ_{peak}) exceeds the critical shear stress for the initiation of sediment transport (τ_{crit}, fig. 13); the blue regions are where $\tau_{peak} < \tau_{crit}$. A much smaller proportion of the shelf is mobilized during a La Niña October than during an El Niño February (fig. 14). The significant wave height (H_{sig}) is 4.43 m and the dominant wave period (T_{dom}) is 12.25 seconds.

Table 3. Percent of sea floor disturbed by depth range for return interval model run boundary conditions.

Return Interval (years)	120 – 500 m	90 – 120 m	60 – 90 m	30 – 60 m	0 – 30 m
2	34.19	96.50	99.16	99.38	99.03
10	52.14	98.64	99.66	99.70	99.41
25	63.54	99.09	99.76	99.77	99.32
50	75.43	99.50	99.87	99.80	99.37
100	80.71	99.50	99.87	99.67	99.19

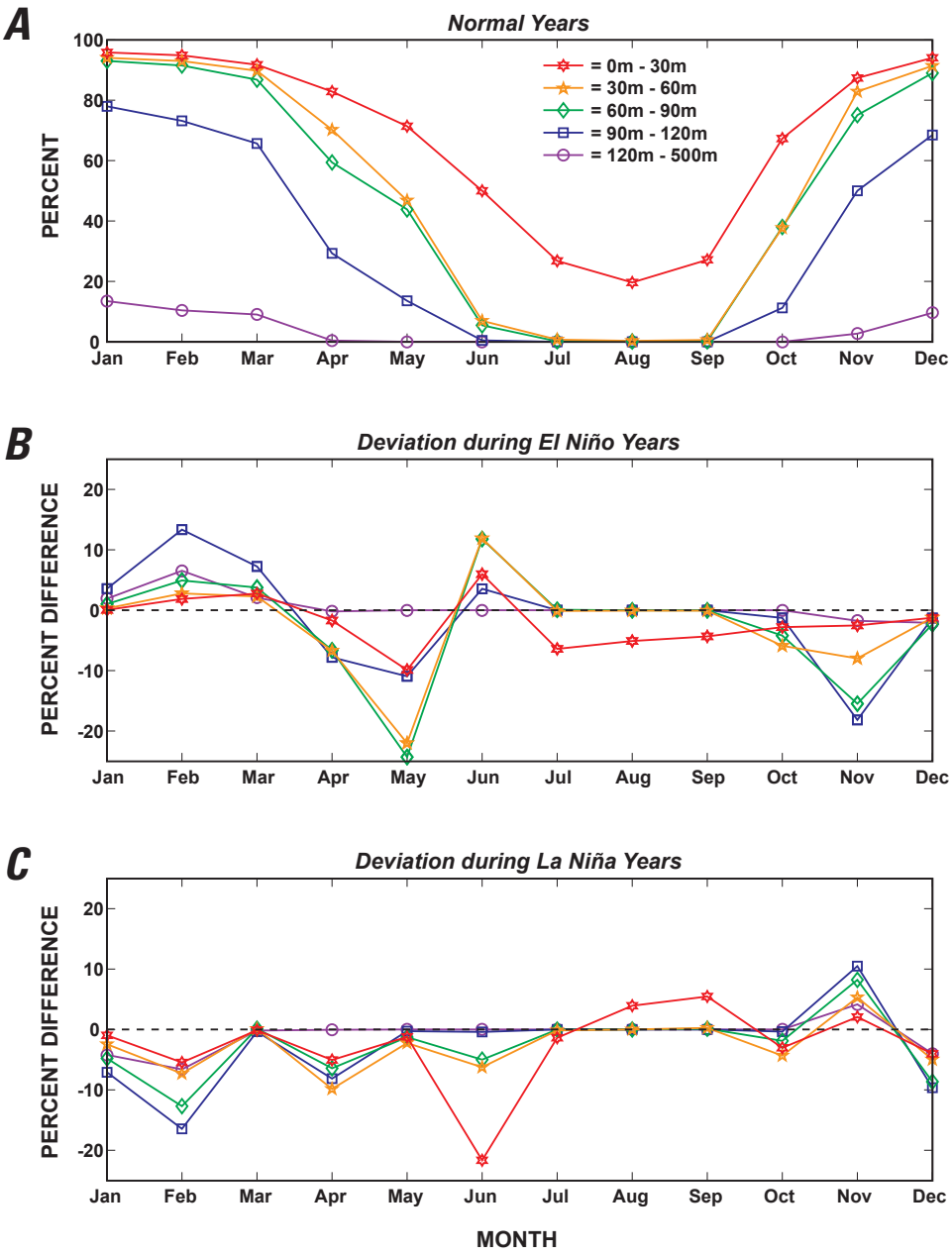

Figure 16. Plots showing the temporal variation in percent of sea floor in the study area disturbed by depth range. A, Normal years. B, Deviation from normal during El Niño conditions, with positive values showing a percentage increase in area disturbed compared to normal conditions and negative values showing a percentage decrease in area disturbed than during normal conditions. C, Deviation from normal during La Niña conditions. The greatest increase in percentage of sea floor mobilized during El Niño conditions occurs late in the winter during the month of February, whereas the greatest increase during La Niña conditions occurs earlier in the winter during the month of November.

Table 4. Percent of sea floor disturbed by depth range for climatic model run boundary conditions.

Climate	Month	120 – 500m	90 – 120m	60 – 90m	30 – 60m	0 – 30m
Normal	Jan	13.45	77.95	93.02	94.05	95.86
Normal	Feb	10.39	73.18	91.50	92.96	94.89
Normal	Mar	9.01	65.68	86.78	89.77	91.77
Normal	Apr	0.39	29.27	59.39	70.21	82.85
Normal	May	0.00	13.55	43.81	46.76	71.41
Normal	Jun	0.00	0.41	5.46	6.91	50.00
Normal	Jul	0.00	0.00	0.13	0.69	26.77
Normal	Aug	0.00	0.00	0.07	0.30	19.64
Normal	Sep	0.00	0.00	0.13	0.59	27.11
Normal	Oct	0.00	11.23	38.01	37.68	67.31
Normal	Nov	2.67	50.00	75.04	82.87	87.37
Normal	Dec	9.56	68.50	89.01	91.42	94.05
El Niño	Jan	15.34	81.50	94.03	94.34	95.90
El Niño	Feb	16.90	86.50	96.42	95.73	96.75
El Niño	Mar	11.06	72.91	90.52	92.04	94.51
El Niño	Apr	0.17	21.45	52.75	63.50	81.12
El Niño	May	0.00	2.59	19.49	24.73	61.49
El Niño	Jun	0.00	3.95	17.23	18.78	55.95
El Niño	Jul	0.00	0.00	0.20	0.56	20.35
El Niño	Aug	0.00	0.00	0.03	0.20	14.53
El Niño	Sep	0.00	0.00	0.10	0.49	22.76
El Niño	Oct	0.00	9.95	33.79	31.77	64.48
El Niño	Nov	0.89	31.82	59.53	74.88	84.84
El Niño	Dec	7.45	67.18	86.68	90.17	92.78
La Niña	Jan	9.23	70.86	88.23	91.61	94.89
La Niña	Feb	3.78	56.73	78.79	85.66	89.44
La Niña	Mar	8.84	65.32	86.91	89.84	91.64
La Nina	Apr	0.33	21.14	52.95	60.37	77.79
La Niña	May	0.00	13.27	42.53	44.52	70.19
La Niña	Jun	0.00	0.00	0.47	0.66	28.34
La Niña	Jul	0.00	0.00	0.10	0.53	25.38
La Niña	Aug	0.00	0.00	0.07	0.30	23.56
La Niña	Sep	0.00	0.00	0.27	0.85	32.56
La Niña	Oct	0.00	10.86	36.12	33.34	64.27
La Niña	Nov	6.84	60.50	83.27	88.19	89.44
La Niña	Dec	5.56	58.86	80.37	86.45	90.03

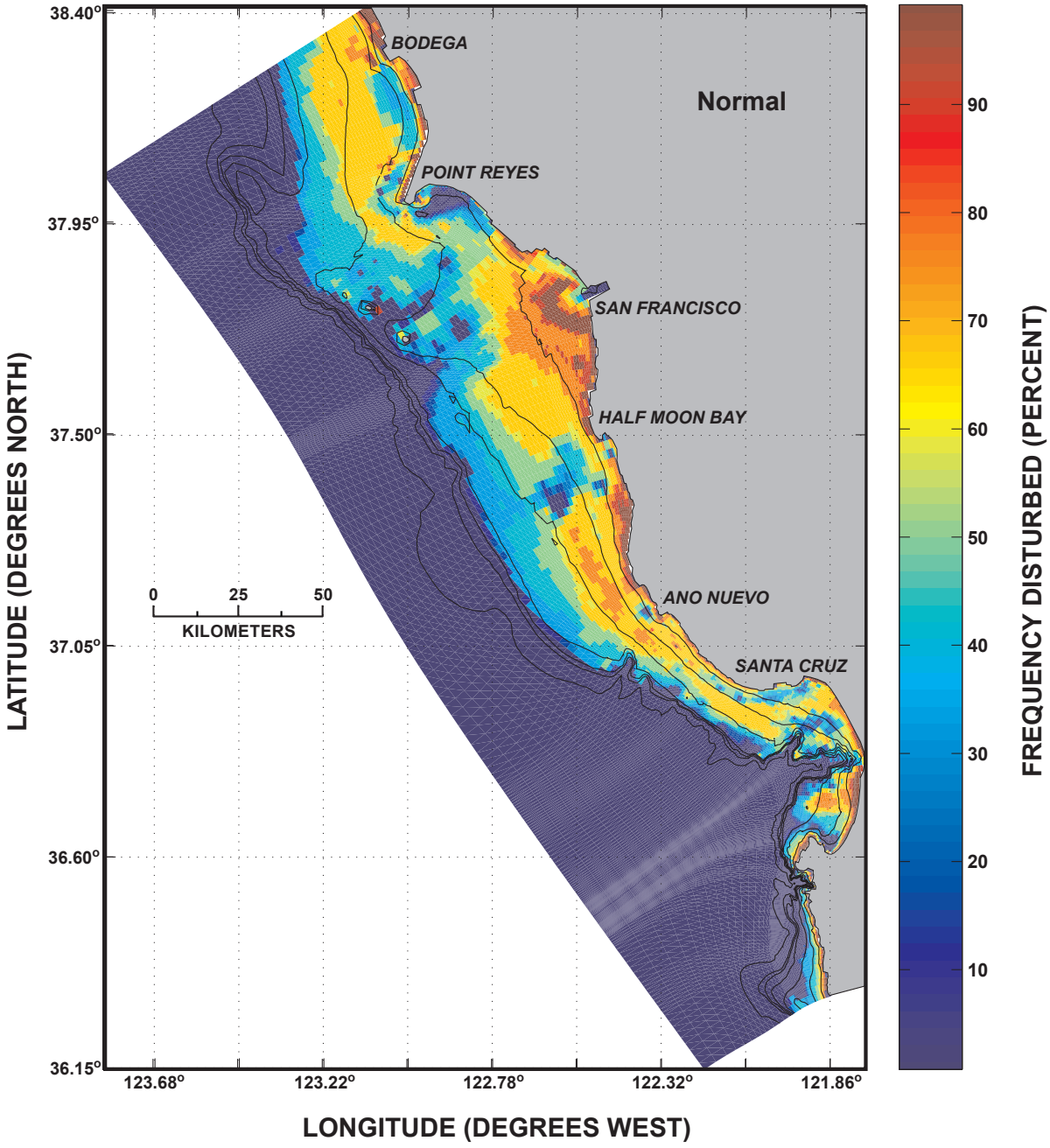

Figure 17. Map of the study area showing the frequency of sea-floor disturbance (as a percentage of months) during a year with normal conditions. Warm colors indicate higher frequencies of disturbance, whereas cool colors indicate less frequently disturbed areas. A general trend is seen of greater disturbance along the inner shelf, with lower frequency of disturbance along the outer shelf, upper slope, areas of the inner shelf in the lee of headlands, and regions of the sea floor characterized by rock outcrops or boulders.

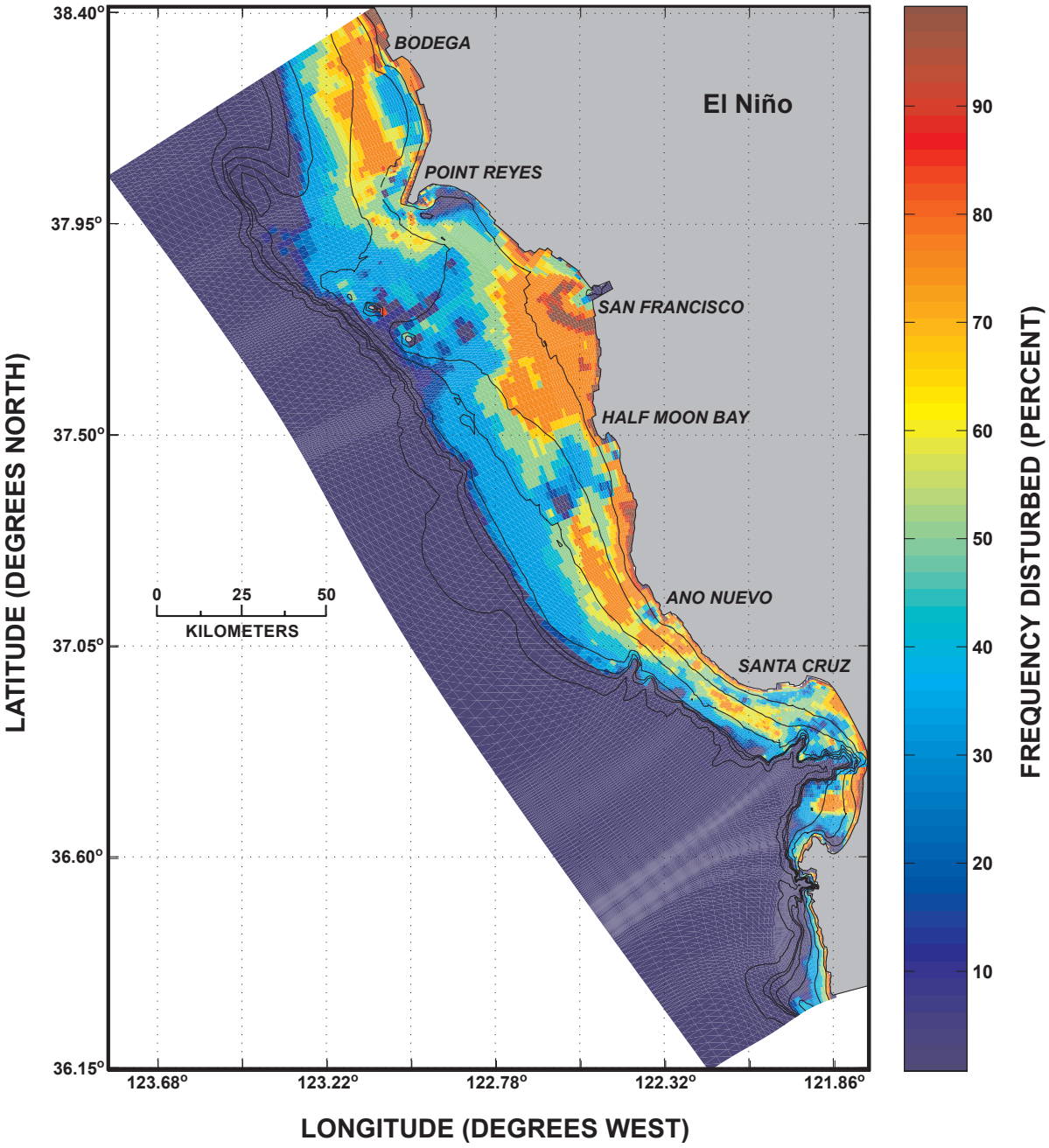

Figure 18. Map of the study area showing the frequency of sea-floor disturbance (as a percentage of months) during a year with El Niño conditions. Warm colors indicate higher frequencies of disturbance, whereas cool colors indicate less frequently disturbed areas. Although 2 percent of the shelf between the 60-m and 90-m isobaths is more frequently disturbed during El Niño conditions than during Normal conditions (fig. 17), this relative increase in frequency of disturbance is offset by an almost equal decrease in frequency of disturbance throughout the rest of the shelf and upper slope in the study area.

tions cause greater mobilization on the middle and outer shelf (30-120 m), as shown in figure 19. Although 10 percent of the shelf between the 60 m and 90 m isobaths is more frequently disturbed during El Niño conditions than during Normal conditions (fig. 17), an almost equal decrease in frequency of disturbance occurs over the rest of the shelf and upper slope in the study area. The difference in frequency of disturbance between El Niño and La Niña conditions is shown in figure 20. El Niño and La Niña conditions generate similar areas with the highest frequency of disturbance (31.6 percent and 32.7 percent of the study area, respectively). Approximately 8.4 percent and 3.5 percent more of the upper slope (120-500

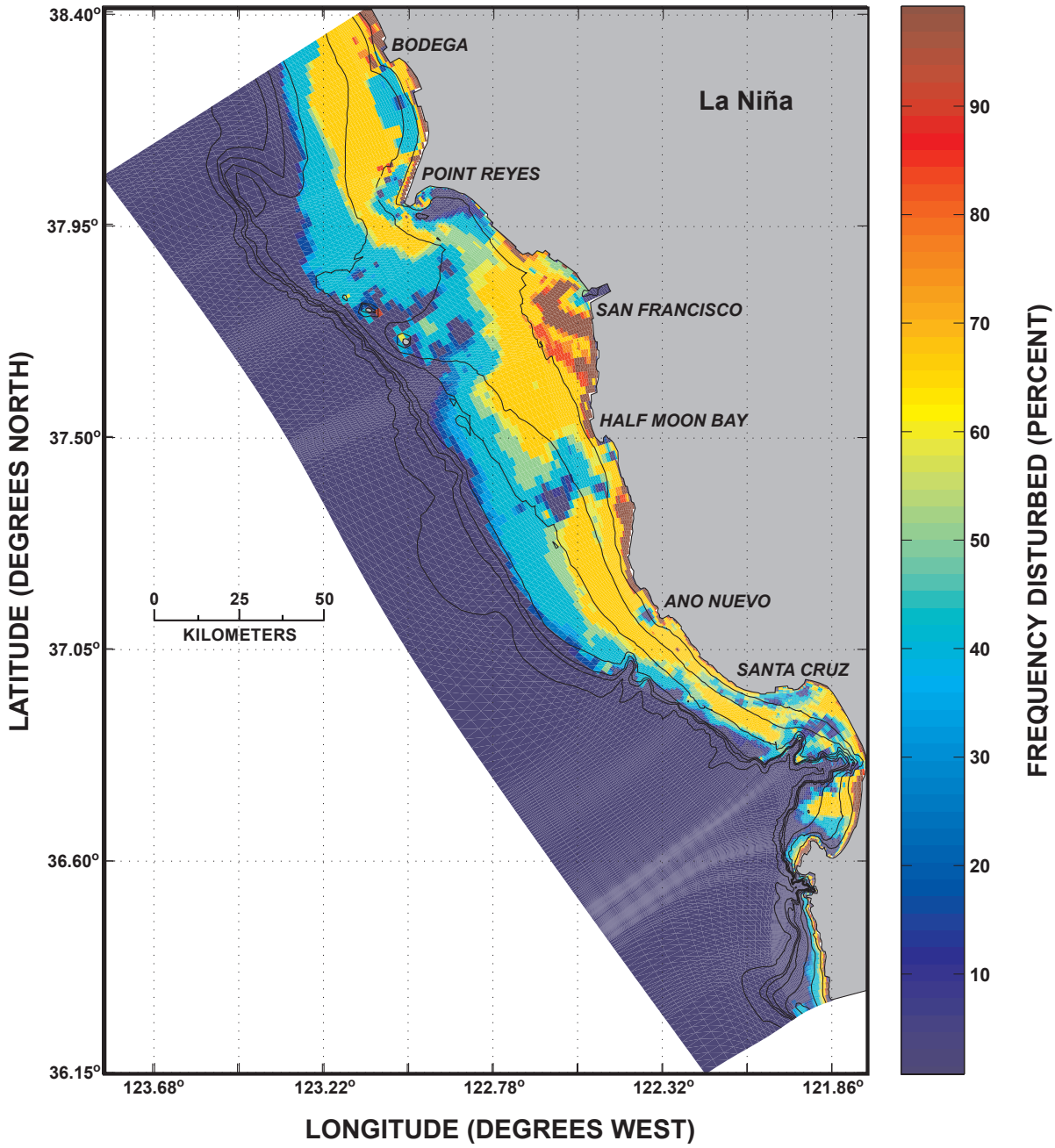

Figure 19. Map of the study area showing the frequency of sea-floor disturbance (as a percentage of months) during a year with La Niña conditions. Warm colors indicate higher frequencies of disturbance, whereas cool colors indicate less frequently disturbed areas. Although 10 percent of the shelf between the 60-m and 90-m isobaths is more frequently disturbed during El Niño conditions than during Normal conditions (fig. 17), an almost equal decrease in frequency of disturbance occurs over the rest of the shelf and upper slope in the study area.

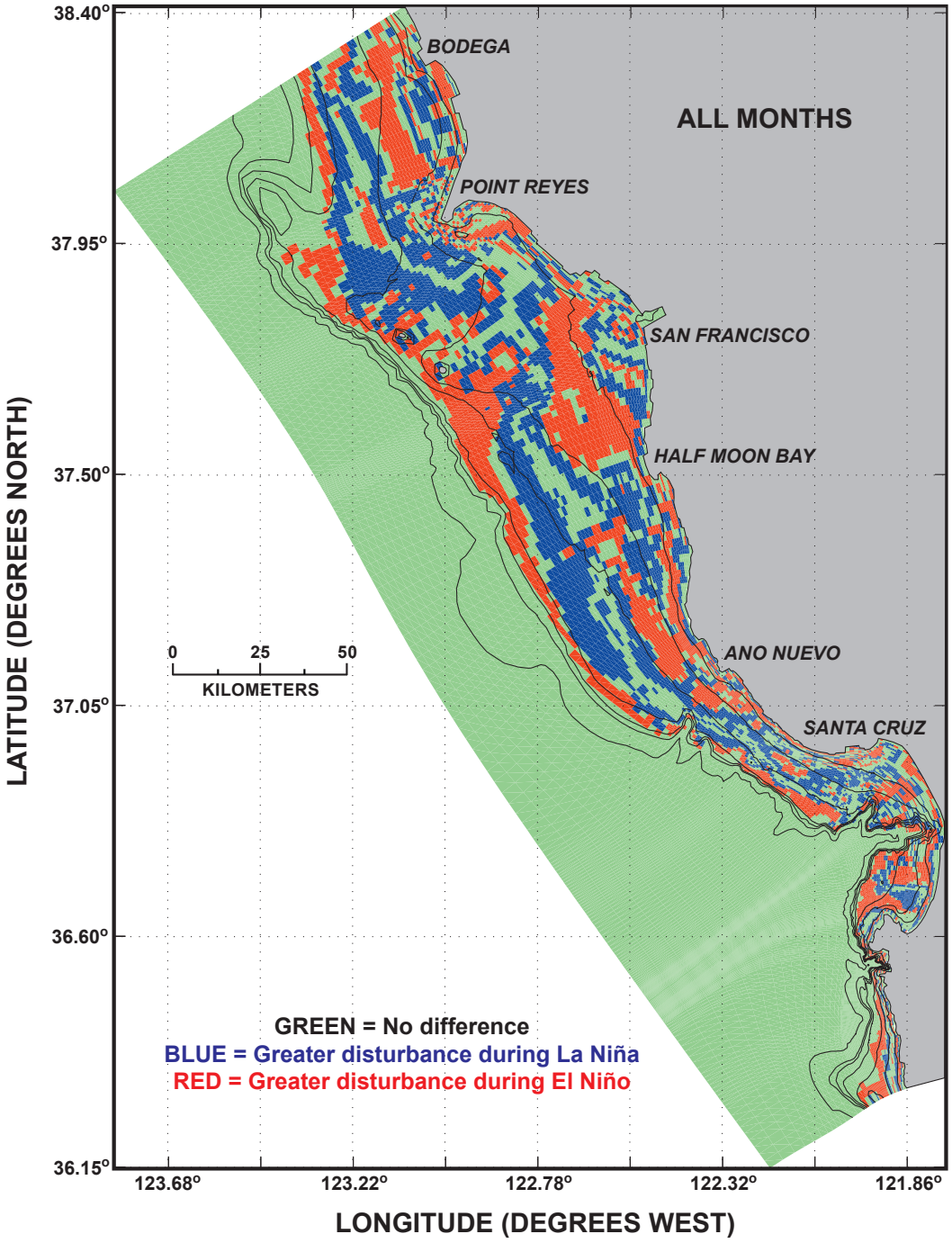

Figure 20. Map showing the difference in frequency that the sea floor in the study area is disturbed during El Niño and La Niña years. El Niño and La Niña conditions generate similar areas with the highest frequency of disturbance (31.6 percent and 32.7 percent of the study area, respectively). Approximately 8.4 percent and 3.5 percent more of the upper slope (120-500 m) and inner shelf (0-30 m), respectively, is disturbed more frequently during El Niño conditions, whereas La Niña conditions result in more frequent disturbances on 5.8 percent of the outer shelf (60-120 m).

m) and inner shelf (0-30 m), respectively, is disturbed more frequently during El Niño conditions, whereas La Niña conditions result in more frequent disturbances on 5.8 percent of the outer shelf (60-120 m).

There is substantial temporal variation in the influence of ENSO events on these general trends (figs. 21 through 24). The greatest increase in percentage of sea floor mobilized during El Niño conditions occurs during the winter (December-February),

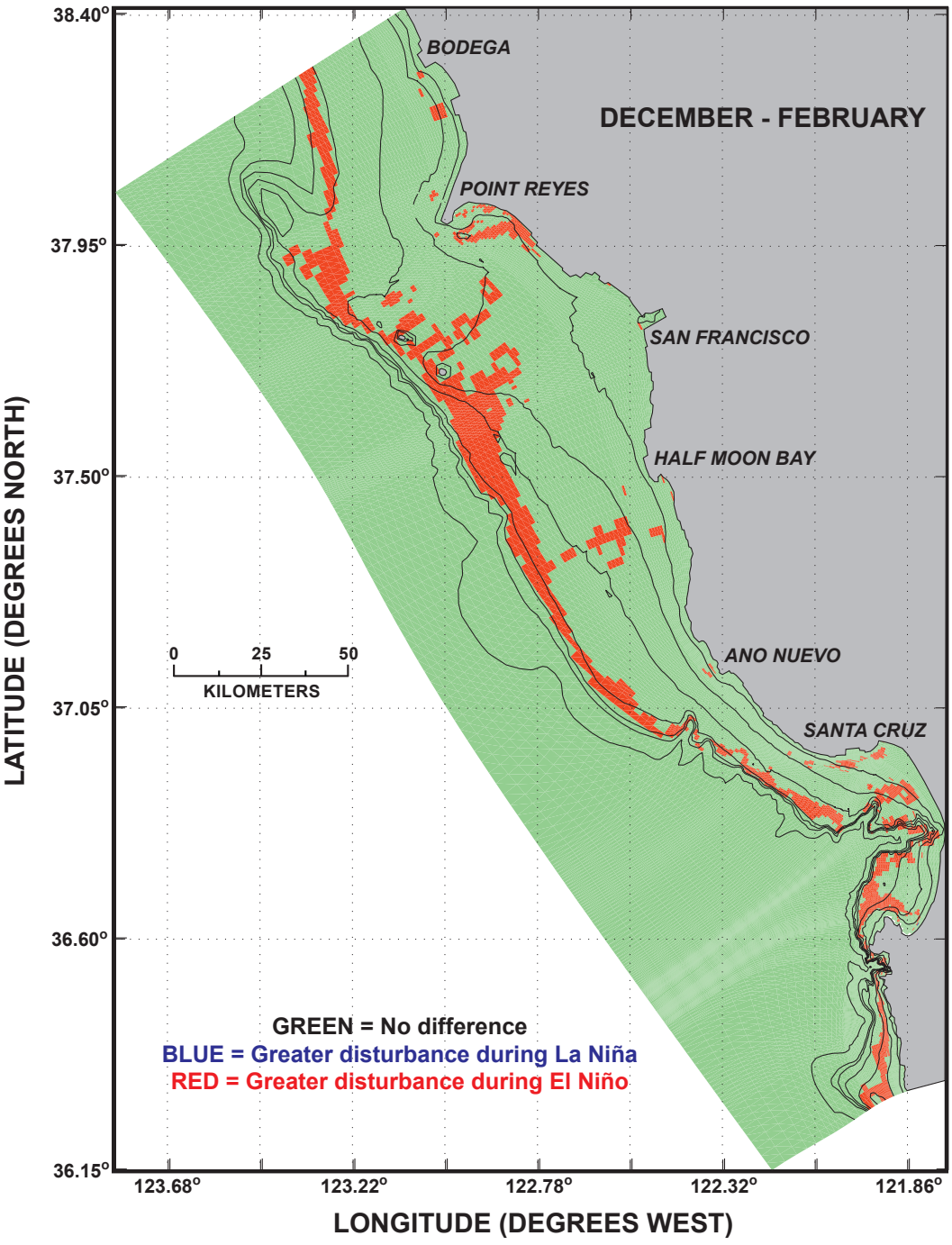

Figure 21. Map showing the difference in frequency that the sea floor in the study area is disturbed during El Niño and La Niña winter months (December-February). El Niño conditions resulted in a much larger area with more frequent disturbance (16.1 percent) than La Niña conditions (<0.1 percent), with 13.2 percent, 24.7 percent and 8.8 percent more of the upper slope (120-500 m), outer shelf (60-120 m), and inner shelf (0-30 m), respectively, disturbed during El Niño conditions.

as shown in figure 21. El Niño conditions resulted in a much larger area with more frequent disturbance (16.1 percent) than La Niña conditions (<0.1 percent), with 13.2 percent, 24.7 percent and 8.8 percent more of the upper slope (120-500 m), outer shelf (60-120 m) and inner shelf (0-30 m), respectively, disturbed during El Niño conditions. La Niña conditions resulted in a more than twice the area with more frequent disturbance (13.3 percent) than El Niño conditions (5.9 percent) during the spring

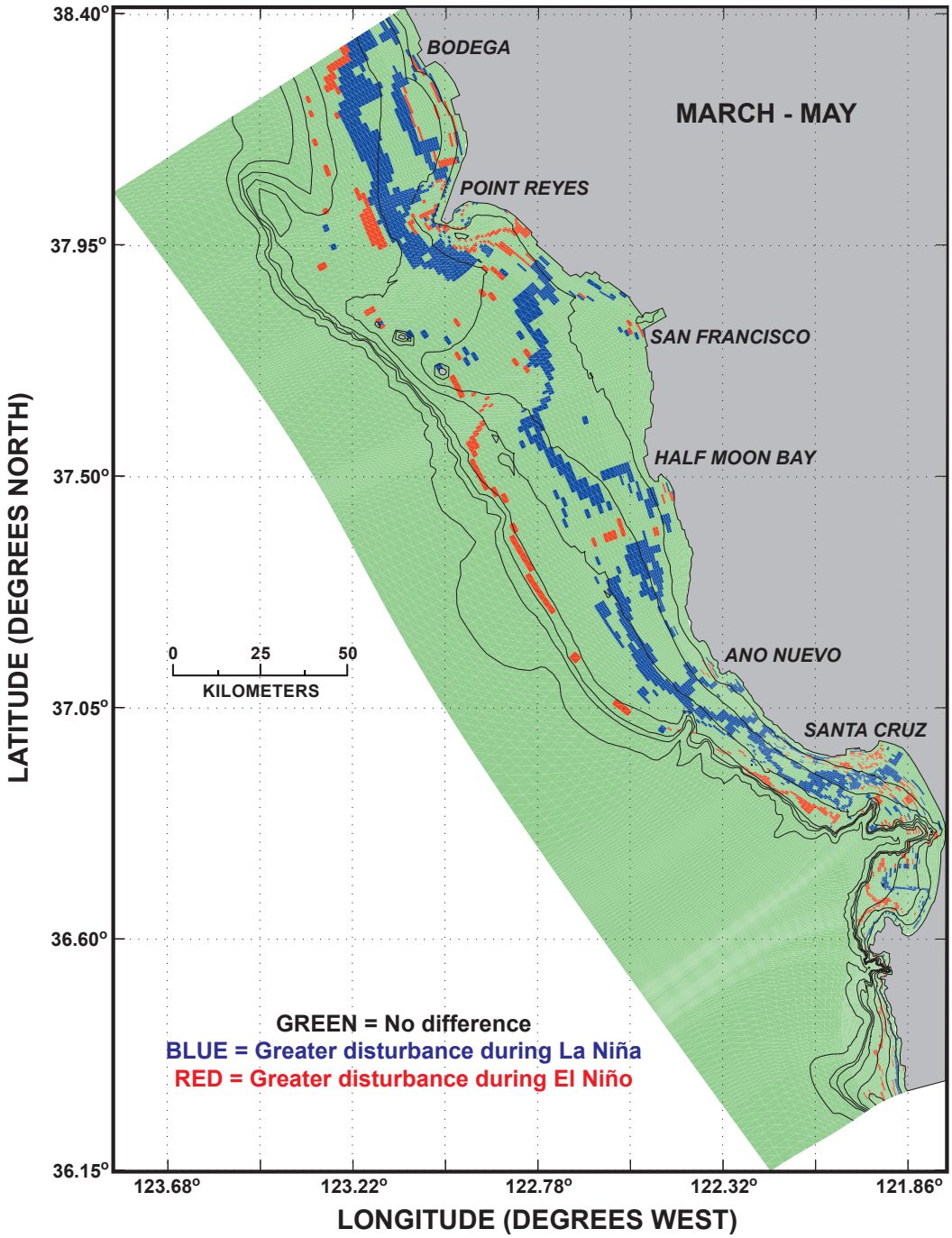

Figure 22. Map showing the difference in frequency that the sea floor in the study area is disturbed during El Niño and La Niña spring months (March-May). La Niña conditions resulted in a more than twice the area with more frequent disturbance (13.3 percent) than El Niño conditions (5.9 percent). Whereas El Niño conditions caused 2.1 percent more of the upper slope (120-500 m) to be more frequently disturbed, La Niña conditions resulted in 24.7 percent and 8.8 percent more of the outer shelf (60-120 m) and inner shelf (0-30 m), respectively, to be more frequently disturbed.

months (March-May), as shown in figure 22. Whereas El Niño conditions caused 2.1 percent more of the upper slope (120-500 m) to be more frequently disturbed, La Niña conditions resulted in 24.7 percent and 8.8 percent more of the outer shelf (60-120 m) and inner shelf (0-30 m), respectively, to be more frequently mobilized. El Niño conditions resulted in a more than six times the area with a higher frequency of disturbance (13.1 percent) than La Niña conditions (2.0 percent) during the summer

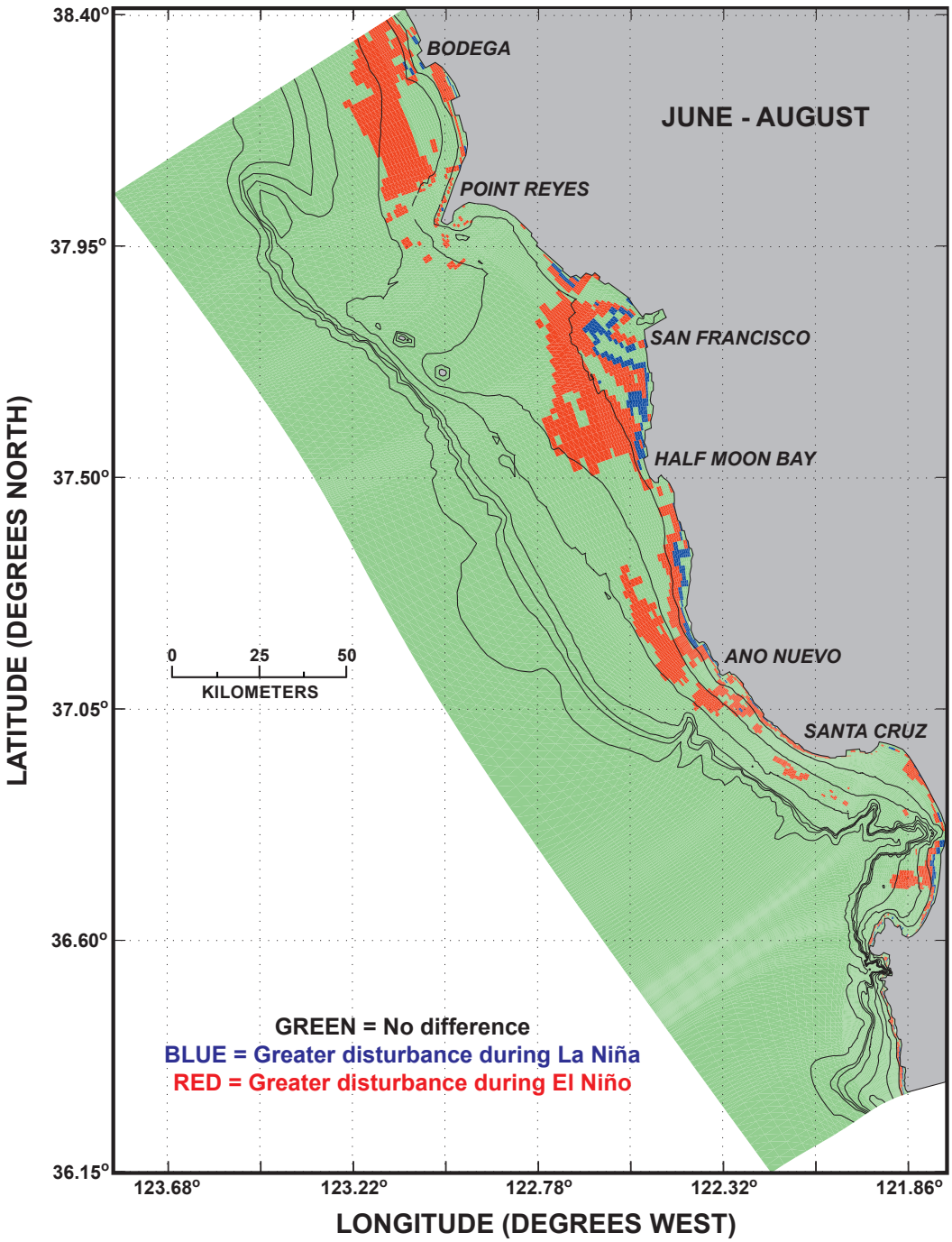

Figure 23. Map showing the difference in frequency that the sea floor in the study area is disturbed during El Niño and La Niña summer months (June-August). El Niño conditions resulted in a more than six times the area with a higher frequency of disturbance (13.1 percent) than La Niña conditions (2.0 percent). Whereas neither set of end-member conditions caused increased mobility on the upper slope (120-500 m), El Niño conditions resulted in 10.4 percent and 17.2 percent more of the outer shelf (60-120 m) and inner shelf (0-30 m), respectively, to be more frequently disturbed.

months (June-August), as shown in figure 23. Although neither set of end-member conditions caused increased mobility on the upper slope (120 to 500 m), El Niño conditions resulted in 10.4 percent and 17.2 percent more of the outer shelf (60 to 120 m) and inner shelf (0 to 30 m), respectively, to be more frequently disturbed. The greatest increase in percentage of sea floor mobilized during La Niña conditions occurs in the fall (September-November), as shown in figure 24. La Niña conditions resulted

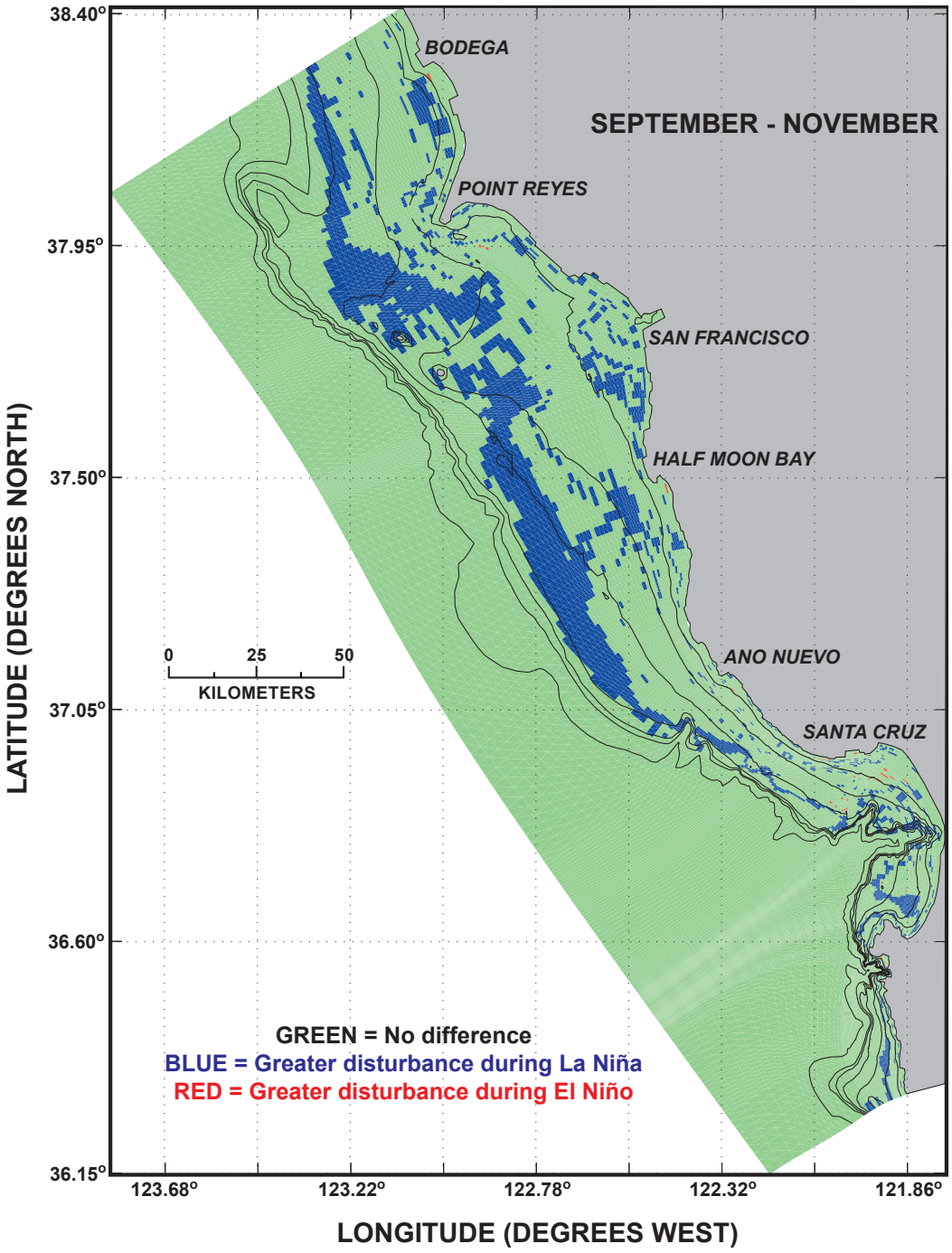

Figure 24. Map showing the difference in frequency that the sea floor in the study area is disturbed during El Niño and La Niña fall months (September-November). La Niña conditions resulted in a much larger area with greater disturbance (18.5 percent) than El Niño conditions (0.3 percent), with 6.0 percent, 27.9 percent and 14.7 percent more of the upper slope (120-500 m), outer shelf (60-120 m), and inner shelf (0-30 m), respectively, disturbed during La Niña conditions.

in a much larger area with greater disturbance (18.5 percent) than El Niño conditions (0.3 percent), with 6.0 percent, 27.9 percent and 14.7 percent more of the upper slope (120-500 m), outer shelf (60-120 m), and inner shelf (0-30 m), respectively, disturbed during La Niña conditions.

The differences in frequency of disturbance between El Niño and La Niña conditions are delineated spatially and by depth range in figure 25. Spatially, El Niño conditions result in greater mobility on the upper slope (120-500 m) and the inner shelf (0-30 m), and La Niña conditions cause greater mobility on the middle and outer shelf (60-120 m). Temporally, El Niño conditions result in more frequent mobility in the winter (December-February) and summer (June-August) months, and La Niña conditions cause greater mobility in the spring (March-May) and fall (September-November) months. An important point is that the entire shelf is being mobilized under both El Niño and La Niña conditions, just at different locations at different times.

Discussion

The results of this study suggest that, on a given month, just under half of the shelf (0-120 m) and 4 percent of the upper slope (120-500 m) is mobilized 1 percent of time. While these results do not attempt to address to what depth this mobilization occurs, they do show wave-induced shear stresses large enough to resuspend the surface sediment layer. These findings indicate that these factors have significant consequences for both geological and biological processes.

Geological Implications

One of the important concepts incorporated into numerical models (Hanson and Kraus, 1989; Larson and Kraus, 1989) used by engineers and coastal scientists is that of "closure depth," or the depth below which no sediment is transported in significant volumes (Hallemeier, 1981; Pilkey and others, 1993). Although the definition of "significant volumes" is loosely constrained, much of the recent work trying to better define the depth of closure has shown that this is not a fixed boundary but varies temporally. Our investigation of sediment mobility along the central California shelf similarly suggests that sediment mobility varies significantly both in space and time due to temporal variations in meteorologic and oceanographic forcing, spatial variations in wave properties (H_{sig} and WV_{dir}), and sea-floor sediment material properties.

The relatively high frequency of mobilization along the inner shelf of the study area, except in the lee of headlands at Point Reyes, Half Moon Bay, Santa Cruz, and the Monterey Peninsula, correlates well with the presence of coarser-grained material in these locations, suggesting that finer-grained material is unstable in these locations and shallow water depths, and thus is likely transported offshore into deeper, more quiescent water depths. This has implications on the terrestrial input of material to the coastal ocean. Most of the precipitation and fluvial discharge along central California occurs during the winter months when 90 percent or more of the coarse material on the inner shelf is being mobilized. Hence, the fine-grained sediment inputs from coastal streams and rivers are probably short lived on the inner shelf and are likely quickly transported offshore into greater water depths where the shear stresses are low enough to allow deposition. Similarly, fine-grained sedimentary material naturally deposited by small coastal landslides into the nearshore or dredged to maintain harbor access during the stormy winter months is likely not stable for substantial periods of time on most of the inner shelf (<30 m depth) of central California.

Conversely, the presence of fine-grained material on the middle shelf that is frequently mobilized a good portion of the year suggests that the supply of this fine-grained sediment from terrestrial sources is greater than the ability of waves to remove the fine-grained material from the mud belt, as suggested by McCave (1972) and Grove and others (1982). This suggests that although most of the streams and rivers draining central California are small by global standards, their steep nature results in them supplying much more material to the coastal zone for the size of their drainage basins relative to many larger river systems, agreeing with the basic tenets found in Milliman and Syvitski (1992). This has significant implications on the flux of biologically important materials (iron, carbon, others) delivered by rivers and streams to the coastal ocean that strongly influence coastal ecosystem dynamics.

Biological Implications

The relatively high percentage (>50 percent) of the central California Continental Shelf that is mobilized at least 1 percent of the time in a given month suggests that the benthic infauna and epifauna along the shelf are adapted to a dynamic hydrodynamic and sedimentary environment. Even along the coarse-grained or rocky sections of the study area, such as Cordell Bank off Point Reyes, "Deep Reef" off Half Moon Bay, and Portuguese Ledge in southern Monterey Bay, the high frequency of mobilization in these regions suggests that many of the deeper bedrock reefs are frequently subjected to moderate wave-orbital velocities (>0.2 m/s; fig. 26) and abraded by mobilized seabed sediment. Furthermore, all of the shallow bedrock reefs on the inner most portions of the Continental Shelf (<10 m depth) except those in the lee of headlands are frequently subjected to strong wave-orbital velocities (>0.5 m/s). The critical velocities for the entrainment of coarse sand and fine sand are 0.5 m/s and 0.2 m/s, respectively, and these wave-orbital velocities will cause the bedrock reefs to be abraded by mobilized interstitial sediment.

Benthic communities' structure is typically determined by the sea-floor composition. Research by Grant and others (1991) on the Scotian Shelf showed that oxygen demand was approximately 2.7 times higher and carbon consumption was approximately 1.5 times higher in surficial fine-grained sediment than in coarser sediment, suggesting links between sea-floor grain size and productivity. Recently, to better describe animal-sedi-

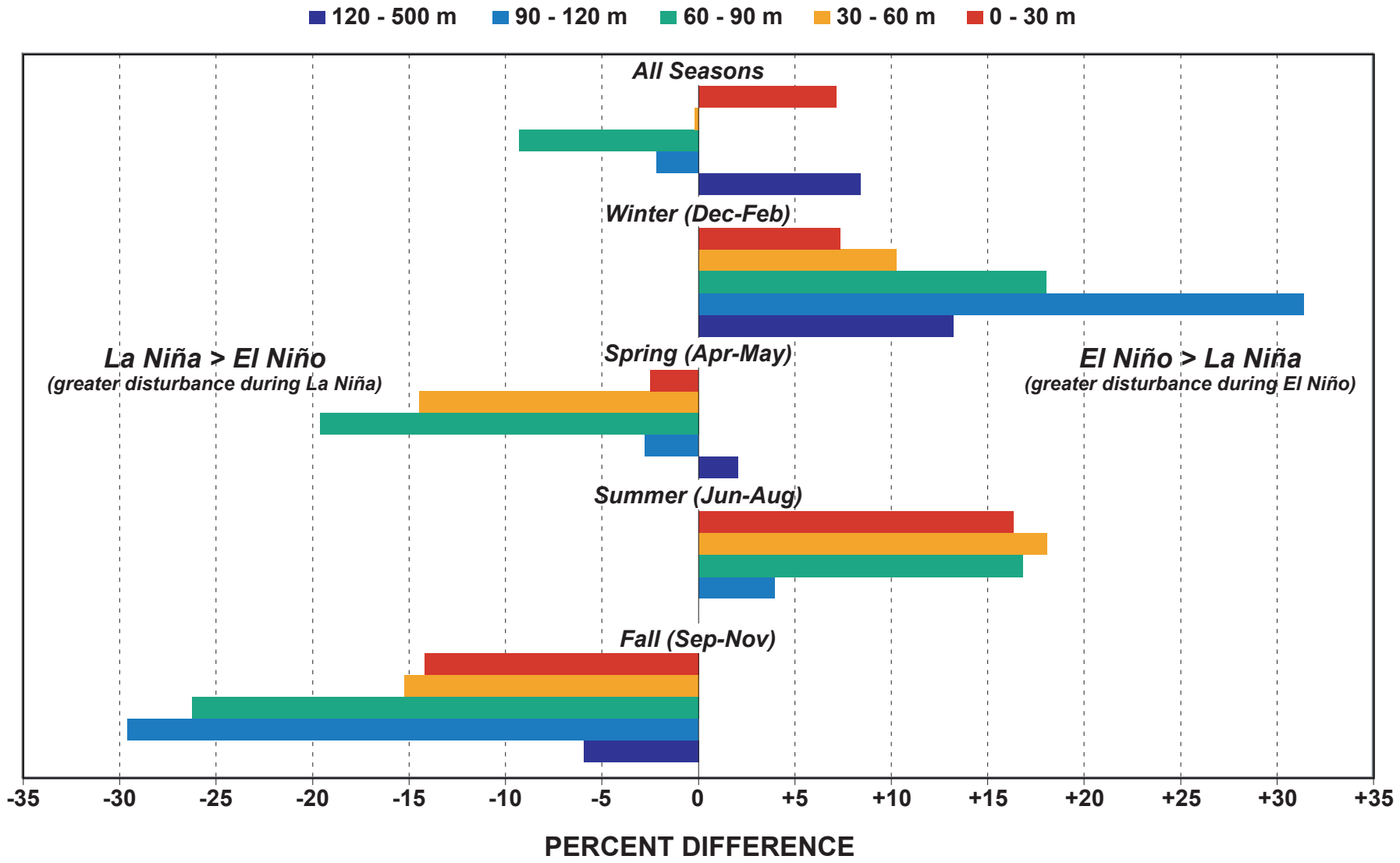

Figure 25. Plot synthesizing the data on the spatial and temporal variations in sea-floor mobility between El Niño and La Niña conditions shown in figures 20 through 24. The colors represent the different depth ranges and the data are plotted for the entire year and each season. Positive values represent the percentage of the sea floor for a given depth range that is mobilized more during El Niño conditions than during La Niña conditions; negative values indicate the frequency of disturbance was greatest during La Niña conditions. Spatially, El Niño conditions result in greater mobility on the upper slope (120-500 m) and the inner shelf (0-30 m), and La Niña conditions cause greater mobility on the middle and outer shelf (60-120 m). Temporally, El Niño conditions result in more frequent mobility in the winter (December-February) and summer (June-August) months, and La Niña conditions cause greater mobility in the spring (March-May) and fall (September-November) months.

ment relationships, Snelgrove and Butman (1994) suggested that hydrodynamics and sediment mobilization be incorporated into habitat classification. Their work suggested that sediment mobilization helped to better constrain species distribution. Potential future climate change, and the resulting changes in storm patterns and intensity, could modify the sediment distribution and mobilization patterns shown here, and thus alter benthic community structure.

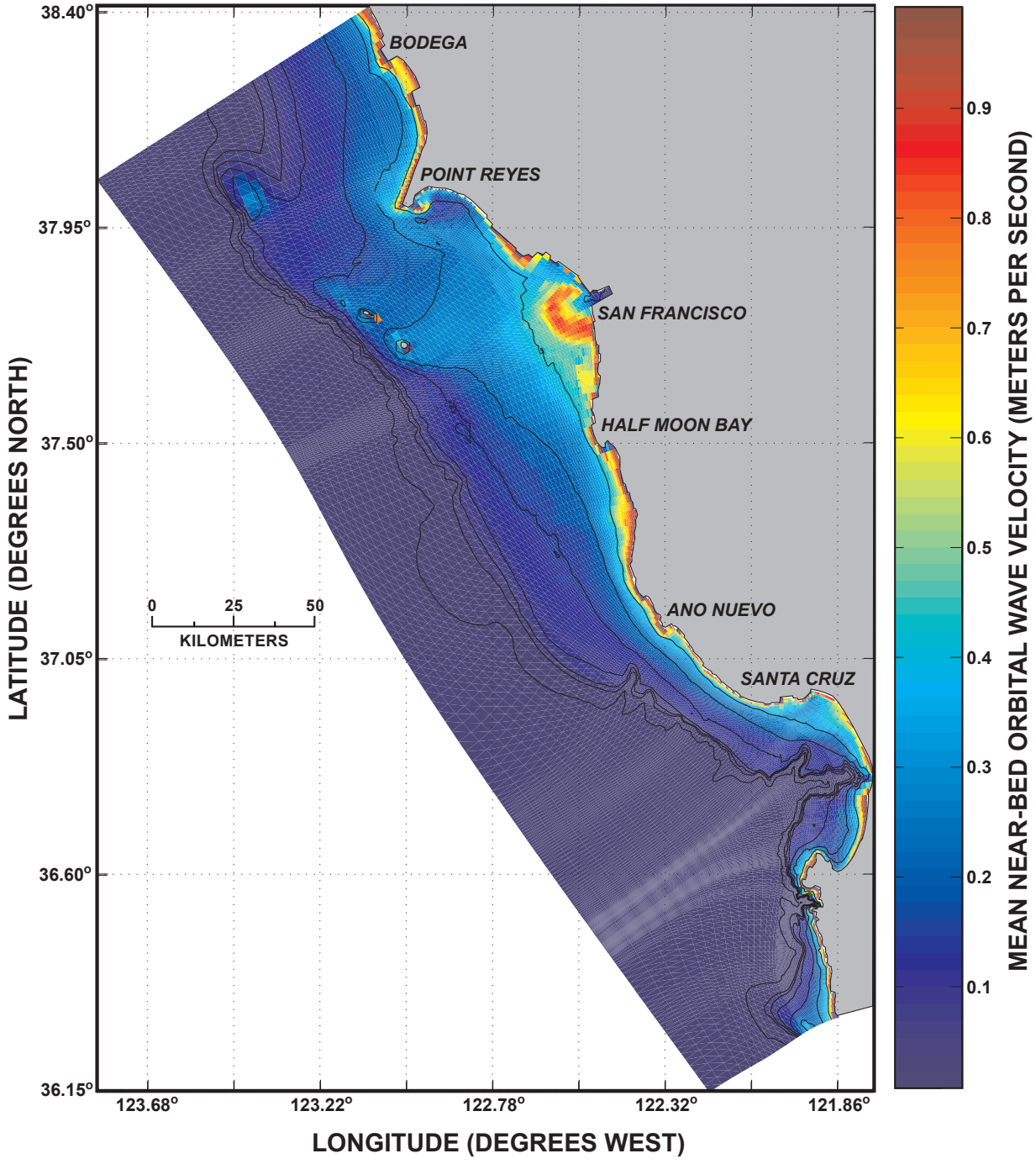

Figure 26. Map of the study area displaying the mean peak near-bed wave orbital velocity (U_{orb}), in m/s, over the model domain for all months and conditions. Warmer colors denote regions that experience faster wave-driven oscillatory near-bed currents. The greatest U_{orb} values are found in shallow regions where significant wave height (H_{sig}) is large, with substantial U_{orb} values observed all across the inner shelf and elevated U_{orb} values observed out into water depths exceeding 90 m

Conclusions

Oceanographic and meteorologic data were combined with bathymetry and gridded grain-size data held in the USGS usSEABED database to predict the mobilization of the unconsolidated sea floor on the Continental Shelf and upper slope off central California. Sediment resuspension was investigated under different climatic regimes and statistical projections. Spatially, the shallower regions are generally more frequently mobilized than the deeper regions. Temporally, the greater storminess during the winter months (December–February) results in approximately 10 percent of the upper slope (120-500 m) in the study area being mobilized, whereas in the summer months (July-September) only the inner shelf (0-30 m) is mobilized by waves. El Niño conditions cause greater mobilization on the upper slope (120-500 m) and the inner shelf (0-30 m); La Niña conditions cause greater mobilization on the middle and outer shelf (30-120 m). There is substantial temporal variation in the influence of ENSO events on these general trends, with the greatest increase in percentage of sea floor mobilized during the winter (December-February) of an El Niño, whereas the greatest increase during La Niña conditions occurs in the fall (September-November). By understanding the spatial and temporal variability in the disturbance of the sea floor, managers and planners can use this information when considering offshore activities such as trawling, dredging, and the emplacement of sea-floor engineering structures (cables, pipelines, others).

Acknowledgments

This research was conducted as part of the USGS Benthic Habitats Project's effort to better understand the impact of geologic and oceanographic processes on central California's shoreline and nearshore ecosystems. We would like to thank Monica Tydlaska (University of California, Santa Cruz), who compiled all of the figures presented in the appendices. We also thank Steve Lonhart (Monterey Bay National Marine Sanctuary), Katie Farnsworth (USGS) and Doug George (USGS), who contributed numerous excellent suggestions and timely reviews of the manuscript. James Hendley in the USGS Menlo Park Publications Service Center worked diligently with the authors to get this report into the correct style, grammar, and format and deserves special thanks.

References

Allan, J., and Komar, P.D., 2000, Are ocean wave heights increasing in the eastern North Pacific?: EOS, Transactions of the American Geophysical Union, v. 81, p. 561-567.

Anima, R.J., Eittreim, S.L., Edwards, B.D., and Stevenson, A.J., 2002, Nearshore morphology and late Quaternary geologic framework of the northern Monterey Bay Marine Sanctuary, California: Marine Geology, v. 181, no. 1-3, p. 35-54.

Booij, N., Ris, R.C., and Holthuijsen, L.H., 1999, A third generation model for coastal regions, Part I—Model description and validation: Journal of Geophysical Research, v. 104, no. C4, p. 7649-7666.

Bromirski, P.D., Cayan, D.R., Flick, R.E., 2005, Wave spectral energy variability in the Northeast Pacific: Journal of Geophysical Research, v. 110, C03005, doi:10.1029/2004JC002398.

Carter, D.J.T., Challenor, P.G., Ewing, J.A., Pitt, E.G., Srokosz, M.A. and Tucker, M.J., 1986, Estimating wave climate parameters for engineering applications (Offshore technology report 86-228): London, Her Majesty's Stationery Office, 130 p.

Chin J.L., Clifton, H.E. and Mullins, H.T., 1988, Seismic stratigraphy and late Quaternary shelf history, south-central Monterey Bay, California: Marine Geology v. 81, no. 1-3, p. 137-157.

Delft Hydraulics, 2006, Delft3D-WAVE web page: [http://www.wldelft.nl/soft/d3d/mods/wave/index.html].

Edwards, B.D., 2002, Variations in sediment texture on the northern Monterey Bay National Marine Sanctuary contin-ental shelf: Marine Geology, v. 181, no. 1-3, p. 83-100.

Eittreim, S.L., Anima, R.J., Stevenson, A.J., and Wong, F.L., 2000, Seafloor rocks and sediments of the continental shelf from the Monterey Bay to Point Sur, California: U.S. Geological Survey Miscellaneous Field Studies Map M-2345, scale 1:100,000.

Eittreim, S.L., Anima, R.J. and Stevenson, A.J., 2002, Seafloor geology of the Monterey Bay area continental shelf: Marine Geology, v. 181, no. 1-3, p. 3-34.

Field, M.E., Barber, Jr., J.H., Cacchione, D.A., Drake, D.E. and Wong, F.L., 1992, Holocene sediment map of the central California continental shelf: U.S. Geological Survey Open-file Report 92-338, scale 1:250,000.

Folk, R.L., Andrews, P.B. and Lewis, D.W., 1970, Detrital sedimentary rock classification and nomenclature for use in New Zealand: New Zealand Journal of Geology and Geophysics, v. 13, p. 937-968.

Fredsoe, J. and Deigard, R., 1992, Mechanics of Coastal Sediment Transport: Singapore, World Scientific Publishing Co., World Scientific Advanced Series on Ocean Engineering, v. 3, 369 p.

Grant, J., Emerson, C.W., Hargrave, B.T., and Shortle, J.L., 1991, Benthic oxygen consumption on continental shelves off Eastern Canada: Continental Shelf Research, v. 11, p. 1083-1097.

Grove, K.A., Pilkey, O.H., and Trumbull, J.V.A., 1982, Mud transportation on a steep shelf, Rio de la Plata Shelf, Puerto Rico: Geo-Marine Letters, v. 2, no. 1-2, p. 71-75.

Hallemeier, R.J., 1981, Seaward limit of significant sand transport by waves – An annual zonation for seasonal profiles: Technical Aid No. 81, U.S. Army Coastal Engineering Research Center, Vicksburg, Miss., 218 p.

Hanson, H., and Kraus, N.C., 1989, GENESIS—Generalized Model for Simulating Shoreline Change, Report 1—Technical Reference: Technical Report CERC-89-19, U.S. Army Coastal Engineering Research Center, Vicksburg, Miss.

Hasselmann, D.E., Dunckel, M., and Ewing, J.A., 1980, Directional wave spectra observed during the Joint North Sea Wave Project (JONSWAP) 1973: Journal of Physical Oceanography, v. 10, no. 8, p. 1264–1280.

Holthuijsen, L.H., Booij, N., and Herbers, T.H.C., 1989, A prediction model for stationary, short-crested waves in shallow water with ambient currents: Coastal Engineering, v. 13, p. 23-54.

Inman, D.L. and Jenkins, S.A., 1997, Changing wave climate and littoral drift: California and World Ocean, '97, Conference Proceedings, chap. 73, p. 539-549.

Komar, P.D., 1998, Beach Processes and Sedimentation (2nd ed): New Jersey, Prentice-Hall, Inc., 544 p.

Larson, M., and Kraus, N.C., 1989, SBEACH – Numerical model to simulate storm-induced beach change: Technical Report CERC-89-9. U.S. Army Coastal Engineering Research Center, Vicksburg, Miss.

Maher, N.M., Karl, H.A., Chin, J.L., and Schwab, W.C., 1991, Station locations and grain-size analysis of surficial sediment samples collected on the continental shelf, Gulf of the Farallones during cruise F2-89-NC, January 1989: U.S. Geological Survey Open-file Report 91-375a, 42 p.

Madsen, O.S., 1999, Coastal Sediment Transport Processes: New York, American Society of Civil Engineers Short Course, Coastal Sediments '99 Conference.

McCave, I.N., 1972, Transport and escape of fine-grained sediment from shelf areas, *in* Swift, D.J.P., Duane, D., and Pilkey, O.H., eds., Shelf Sediment Transport: Stroudsburg, Pa., Dowden, Hutchinson and Ross, p. 225–248.

Milliman, J.D., and Syvitski, J.P.M., 1992, Geomorphic/tectonic control of sediment discharge to the ocean—The importance of small mountainous rivers: Journal of Geology, v. 100 no. 5, p. 525-544.

Moore, D.B., 1965, Recent coastal sediments Double Point to Point San Pedro, California: Berkeley, University of California, Hydraulic Engineering Laboratory Technical Report HEL 2-14, 86 p.

National Data Buoy Center, 2006, Station 46042 – Monterey data: National Oceanic and Atmospheric Administration [http://www.ndbc.noaa.gov/station_page.php?station=46042 (last accessed Sept., 3, 2007)].

National Marine Consultants, 1960, Wave statistics for seven deep water stations along the California coast: report prepared for U.S. Army Corps of Engineers, Los Angeles and San Francisco Districts, 20 p.

National Oceanic and Atmospheric Administration, Climate Diagnostics Center, 2006, Multivariate ENSO index: [http://www.cdc.noaa.gov/people/klaus.wolter/MEI/].

Nielsen, P., 1979, Some basic concepts of wave sediment transport: Denmark, Institute of Hydrodynamic and Hydraulic Engineering, Technical University of Denmark, Series Paper 20, 160 p.

Nielsen, P. 1992, Coastal Bottom Boundary Layers and Sediment Transport: Singapore, World Scientific Publishing Co., World Scientific Advanced Series on Ocean Engineering, v. 4, 324 p.

Orzech, Kevin M., Dahl, Wendy E., and Edwards, Brian D., 2001, Core descriptions, core photographs, physical property logs and surface textural data of sediment cores recovered from the continental shelf of the Monterey Bay National Marine Sanctuary during the research cruises M196MB, P295MB, and P197MB: U.S. Geological Survey Open-file Report 01-107, CD-ROM.

Pilkey, O.H., Young, R.S., Riggs, S.R., Smith, A.W.S., Wu, H., and Pilkey, W.D., 1993, The concept of shoreface profile equilibrium – A critical review: Journal of Coastal Research, v. 9 no. 1, p. 255-278.

Reid, J.A., Reid, J.M., Jenkins, C.J., Zimmermann, M., Williams, S.J., and Field, M.E., 2006, usSEABED – Pacific Coast (California, Oregon, Washington) offshore surficial-sediment data release: U.S. Geological Survey Data Series 182, version 1.0 [http://pubs.usgs.gov/ds/2006/182/].

Ris, R.C., 1997, Spectral modeling of wind waves in coastal areas: Delft, The Netherlands, Ph.D. dissertation, Delft University of Technology, Department of Civil Engineering, Communications on Hydraulic and Geotechnical Engineering, Report No. 97-4.

Ris, R.C., Booij, N., and Holthuijsen, L.H., 1999, A third-generation wave model for coastal regions, Part II –Verification: Journal of Geophysical Research, v. 104, no. C4, p. 7667-7682.

Seymour, R.J., Strange, R.R., Cayan, D.R. and Nathan, R.A., 1984, Influence of El Niños on California's wave climate: Proceedings of the 19th Coastal Engineering Conference, American Society of Civil Engineers, vol. 1, p. 577-592.

Schatz, B., 1963, A restudy of bottom sediments near the entrance of the Golden Gate: Berkeley, University of California, Hydraulic Engineering Laboratory, Wave Research Project, Technical Report HEL 4-3, 8 p. with appendices.

Snelgrove, P.V.R., and Butman, C.A., 1994, Animal-sediment relationships revisited – Cause versus effect: Oceanography and Marine Biology Annual Review, v. 32, 111-177.

Storlazzi, C.D. and Wingfield, D.K., 2005, The spatial and temporal variability in oceanographic and meteorologic forcing along Central California – 1980-2002: U.S. Geological Survey Scientific Investigations Report 2005-5085, 39 p.

Wentworth, C.K., 1922, A scale of grade and class terms used for clastic sediments: Journal of Geology, v. 30, p. 377-392.

Wolter, K., and Timlin, M., 1998, Measuring the strength of ENSO – How does 1997/98 rank?: Weather, v. 53, p. 315-324.

Appendixes 1-41

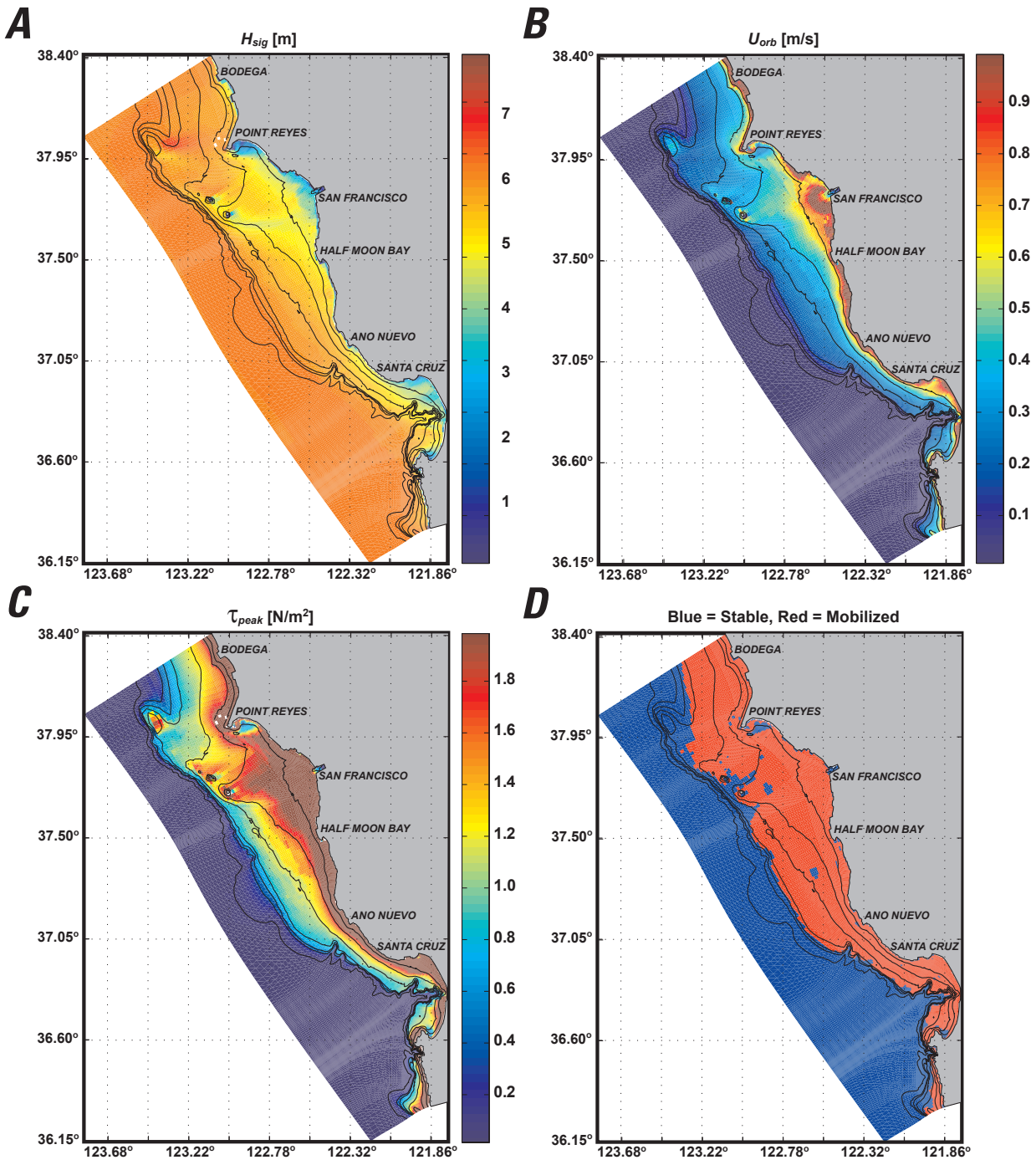

Appendix 1. Model run for a Normal January. *A*, Map of significant wave height (H_{sig}), in m. *B*, Map of peak wave-induced near-bed orbital wave velocity (U_{orb}), in m/s. *C*, Map of peak wave-induced near-bed shear stress (τ_{peak}), in N/m^2. *D*, Map displaying which regions of the study area are mobilized (red) and which are stable (blue) for the modeled conditions. See table 2 for information on model run boundary conditions.

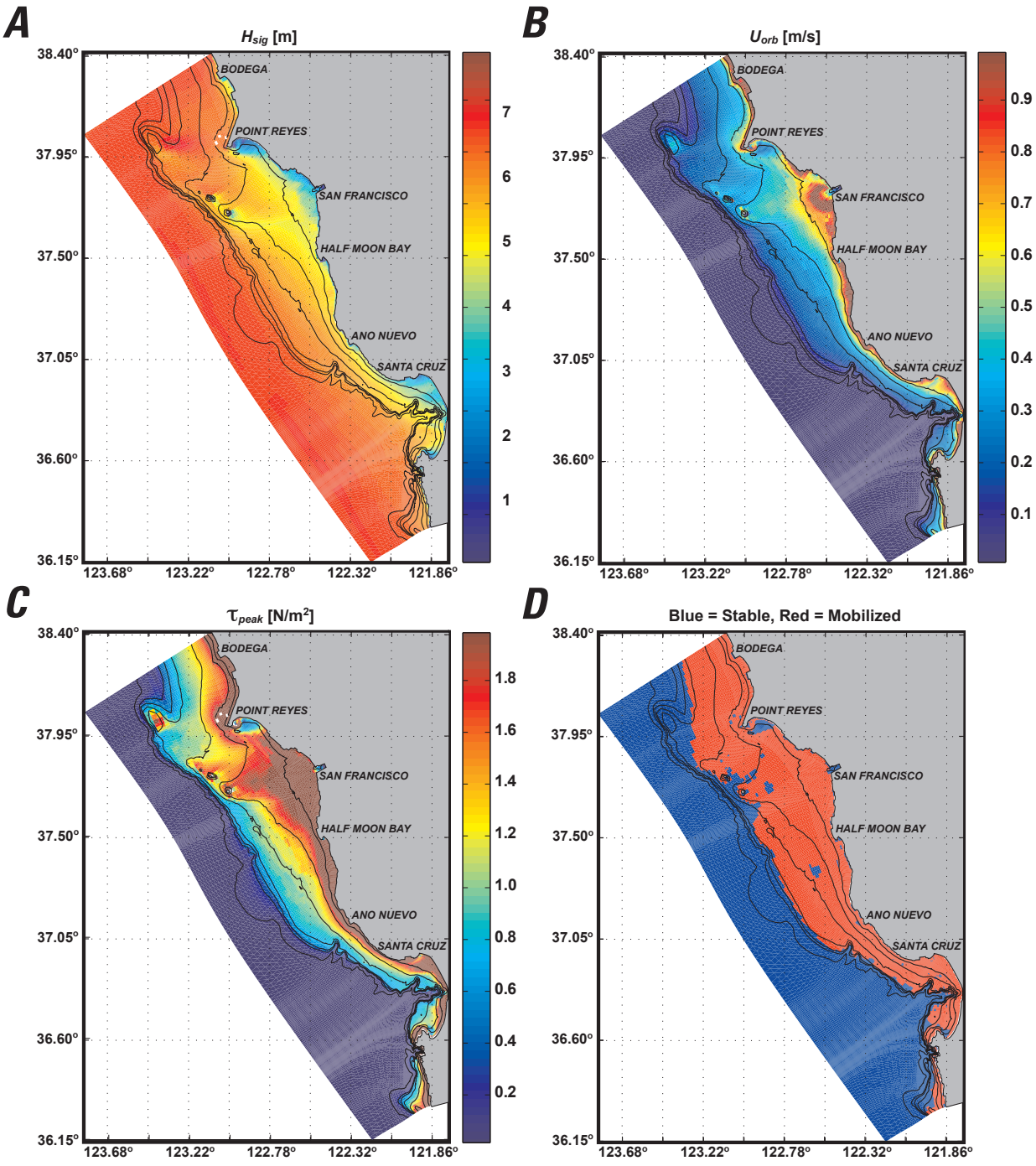

Appendix 2. Model run for a Normal February. *A*, Map of significant wave height (H_{sig}), in m. *B*, Map of peak wave-induced near-bed orbital wave velocity (U_{orb}), in m/s. *C*, Map of peak wave-induced near-bed shear stress (τ_{peak}), in N/m^2. *D*, Map displaying which regions of the study area are mobilized (red) and which are stable (blue) for the modeled conditions. See table 2 for information on model run boundary conditions.

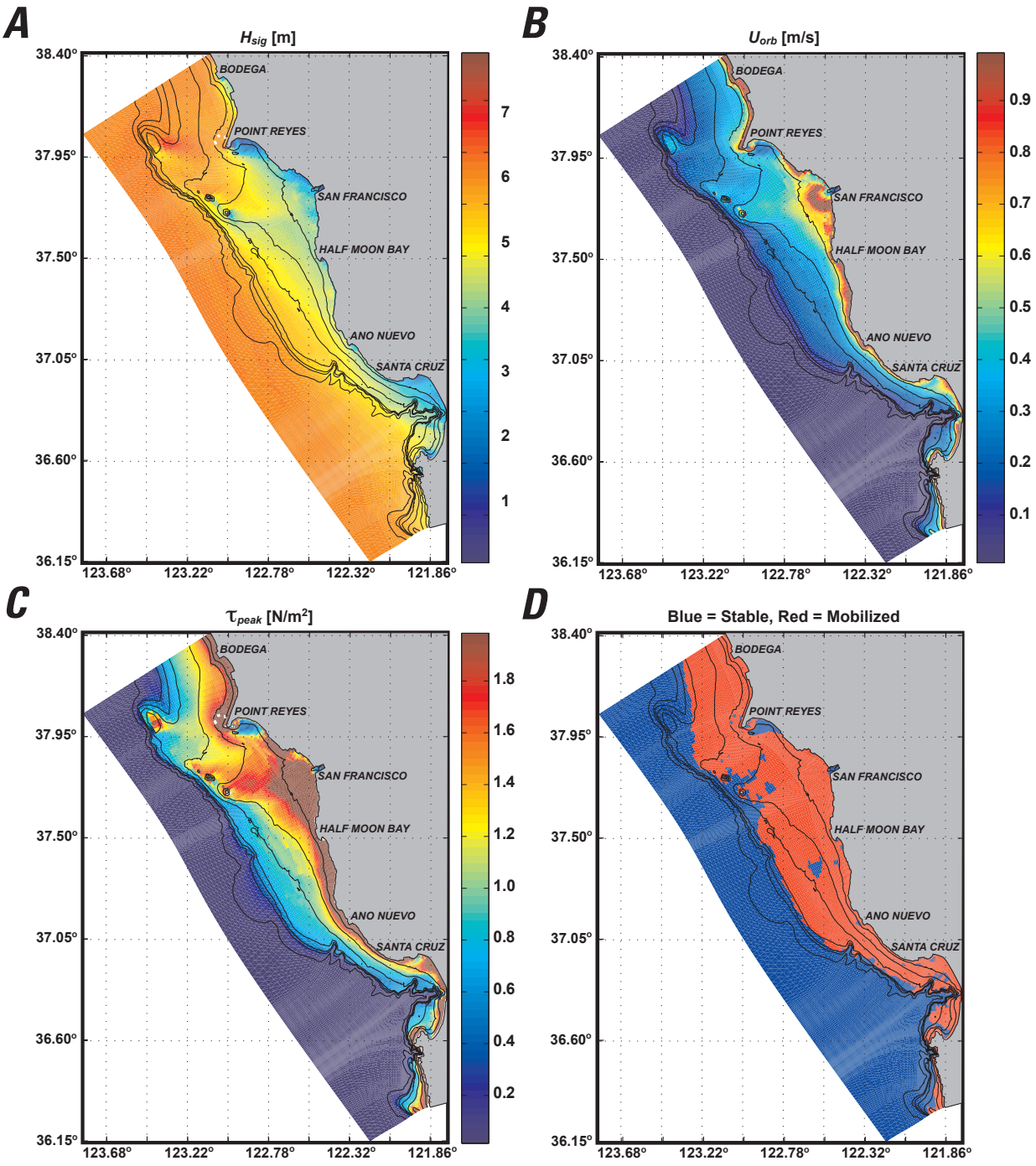

Appendix 3. Model run for a Normal March. *A*, Map of significant wave height (H_{sig}), in m. *B*, Map of peak wave-induced near-bed orbital wave velocity (U_{orb}), in m/s. *C*, Map of peak wave-induced near-bed shear stress (τ_{peak}), in N/m^2. *D*, Map displaying which regions of the study area are mobilized (red) and which are stable (blue) for the modeled conditions. See table 2 for information on model run boundary conditions.

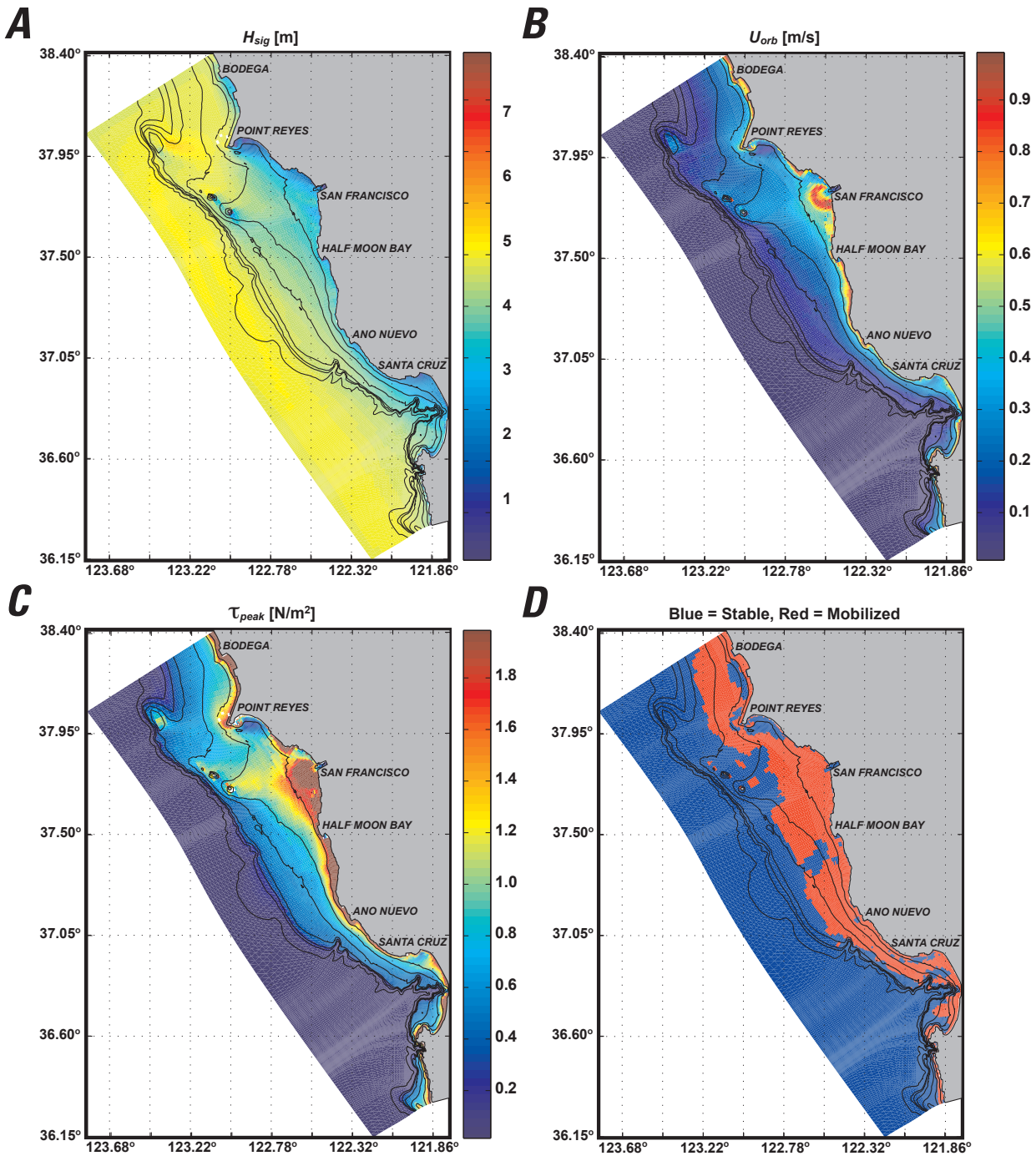

Appendix 4. Model run for a Normal April. *A*, Map of significant wave height (H_{sig}), in m. *B*, Map of peak wave-induced near-bed orbital wave velocity (U_{orb}), in m/s. *C*, Map of peak wave-induced near-bed shear stress (τ_{peak}), in N/m^2. *D*, Map displaying which regions of the study area are mobilized (red) and which are stable (blue) for the modeled conditions. See table 2 for information on model run boundary conditions.

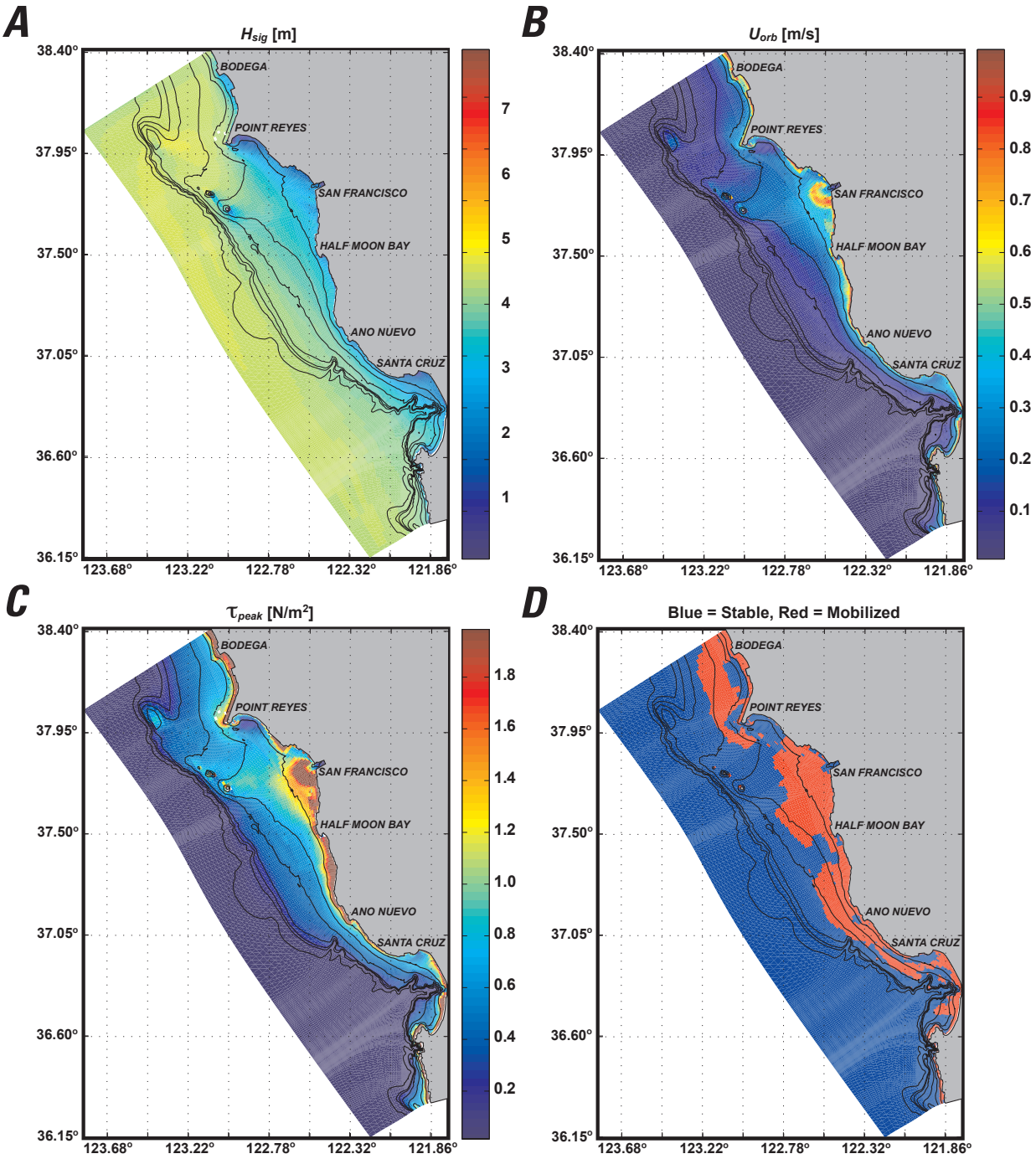

Appendix 5. Model run for a Normal May. *A*, Map of significant wave height (H_{sig}), in m. *B*, Map of peak wave-induced near-bed orbital wave velocity (U_{orb}), in m/s. *C*, Map of peak wave-induced near-bed shear stress (τ_{peak}), in N/m^2. *D*, Map displaying which regions of the study area are mobilized (red) and which are stable (blue) for the modeled conditions. See table 2 for information on model run boundary conditions.

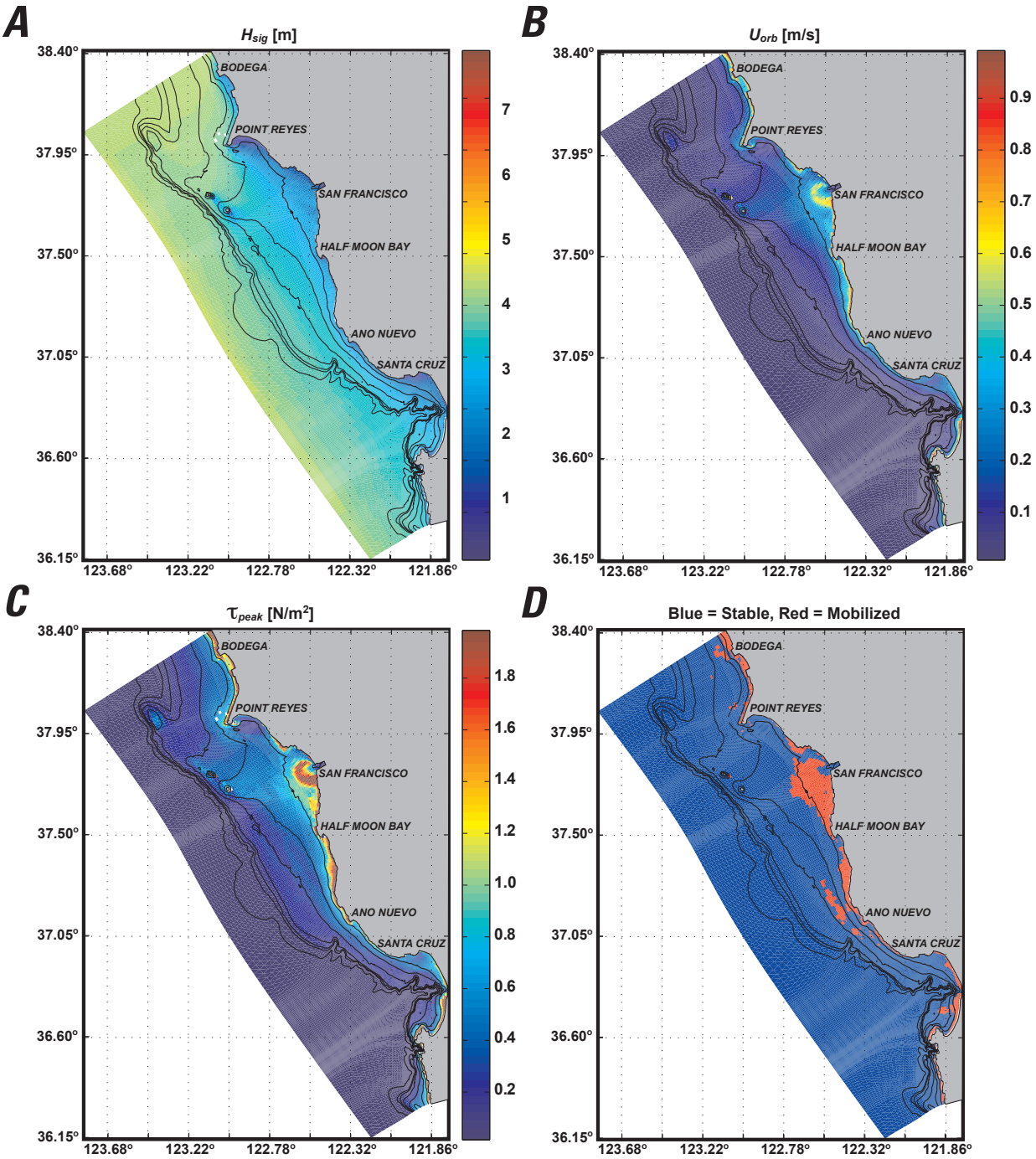

Appendix 6. Model run for a Normal June. *A*, Map of significant wave height (H_{sig}), in m. *B*, Map of peak wave-induced near-bed orbital wave velocity (U_{orb}), in m/s. *C*, Map of peak wave-induced near-bed shear stress (τ_{peak}), in N/m^2. *D*, Map displaying which regions of the study area are mobilized (red) and which are stable (blue) for the modeled conditions. See table 2 for information on model run boundary conditions.

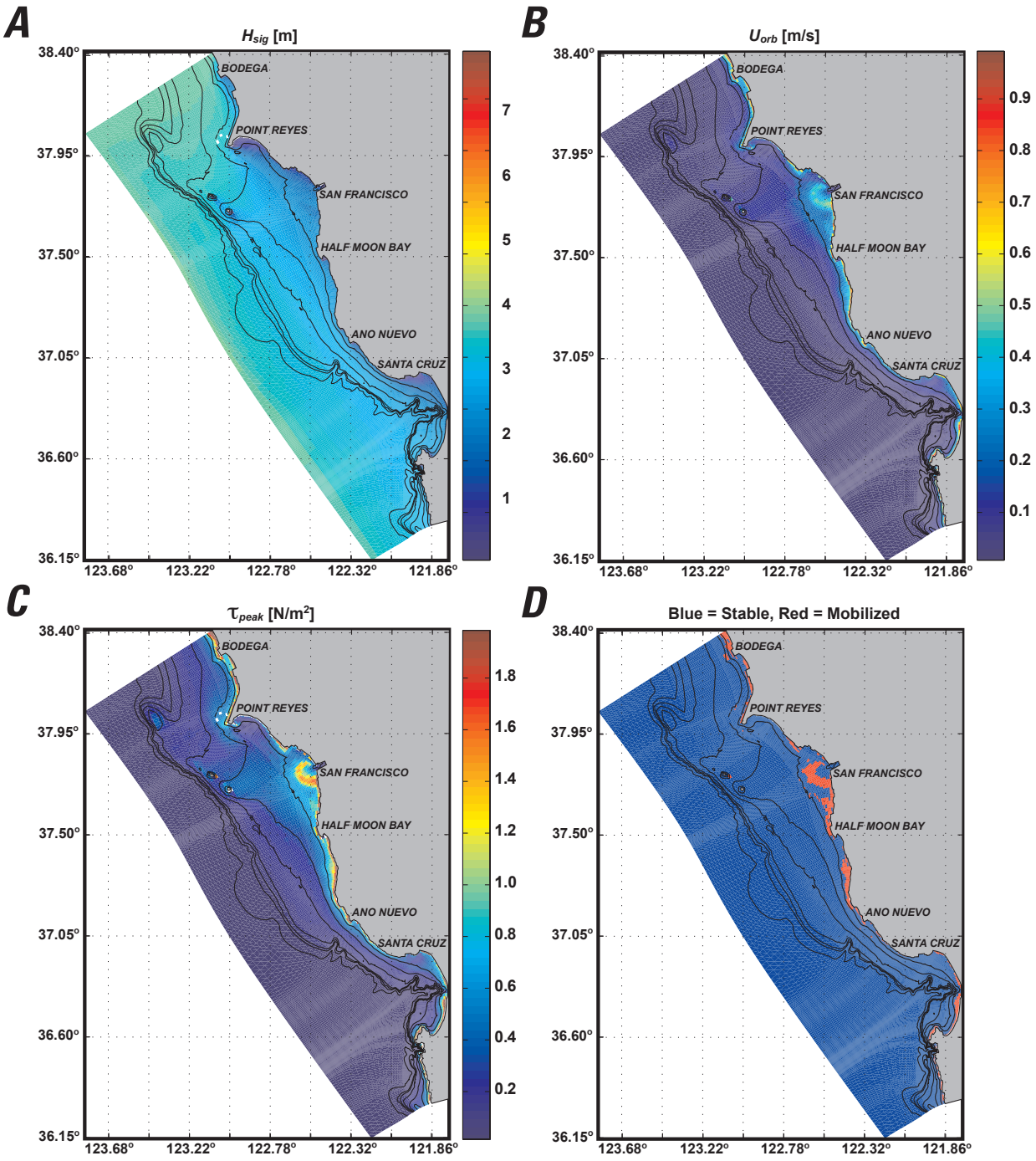

Appendix 7. Model run for a Normal July. *A*, Map of significant wave height (H_{sig}), in m. *B*, Map of peak wave-induced near-bed orbital wave velocity (U_{orb}), in m/s. *C*, Map of peak wave-induced near-bed shear stress (τ_{peak}), in N/m^2. *D*, Map displaying which regions of the study area are mobilized (red) and which are stable (blue) for the modeled conditions. See table 2 for information on model run boundary conditions.

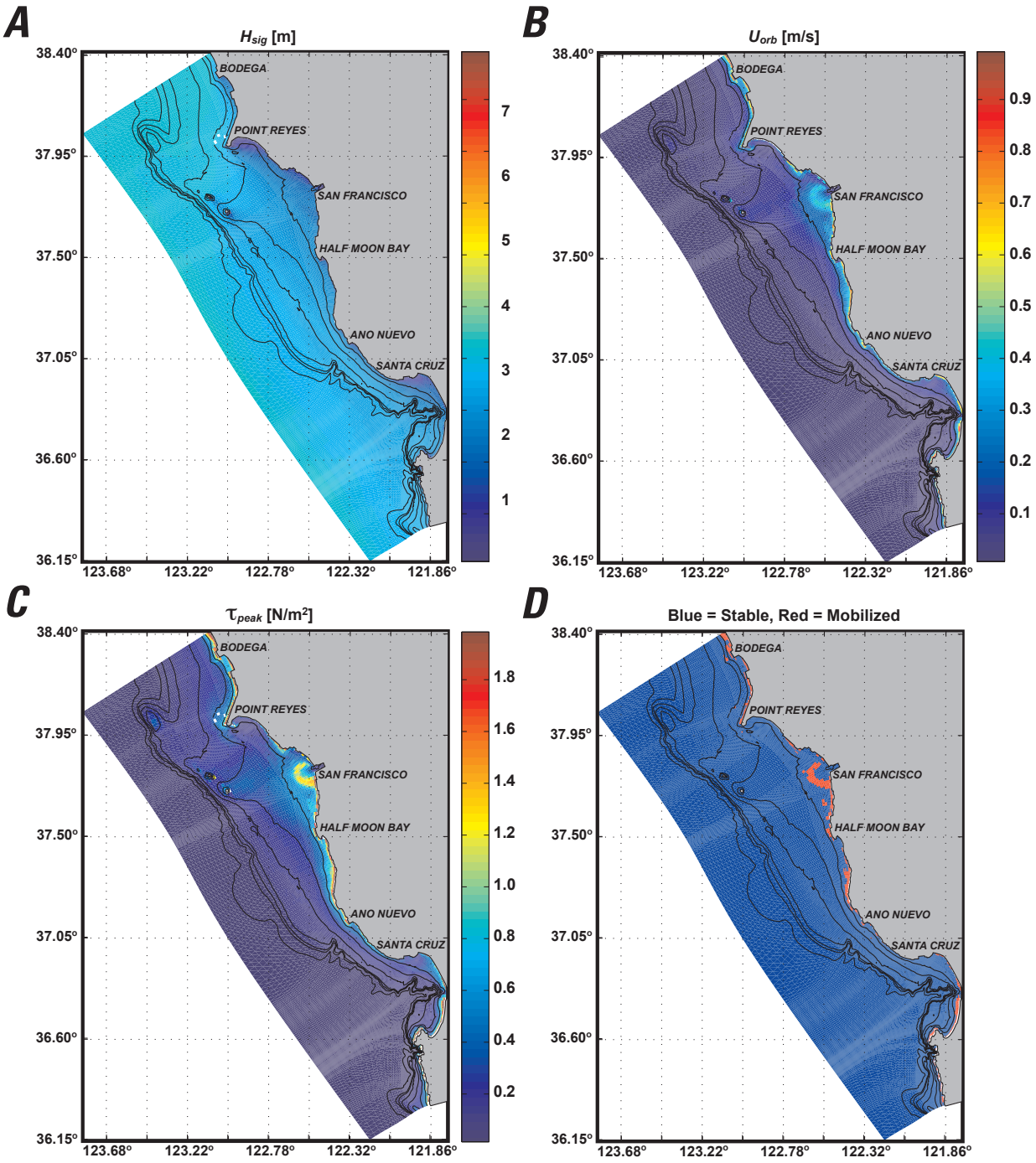

Appendix 8. Model run for a Normal August. *A*, Map of significant wave height (H_{sig}), in m. *B*, Map of peak wave-induced near-bed orbital wave velocity (U_{orb}), in m/s. *C*, Map of peak wave-induced near-bed shear stress (τ_{peak}), in N/m^2. *D*, Map displaying which regions of the study area are mobilized (red) and which are stable (blue) for the modeled conditions. See table 2 for information on model run boundary conditions.

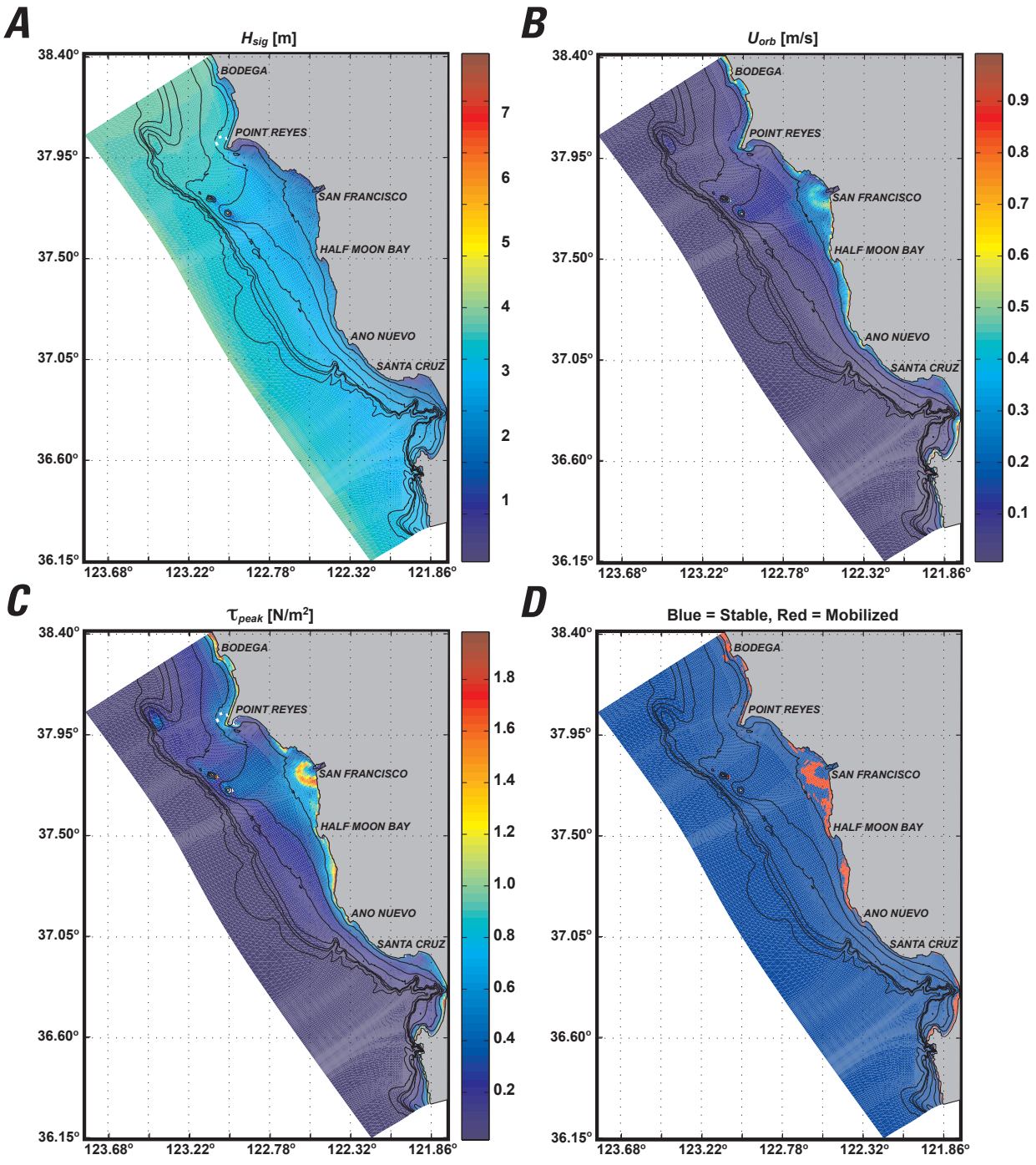

Appendix 9. Model run for a Normal September. *A*, Map of significant wave height (H_{sig}), in m. *B*, Map of peak wave-induced near-bed orbital wave velocity (U_{orb}), in m/s. *C*, Map of peak wave-induced near-bed shear stress (τ_{peak}), in N/m^2. *D*, Map displaying which regions of the study area are mobilized (red) and which are stable (blue) for the modeled conditions. See table 2 for information on model run boundary conditions.

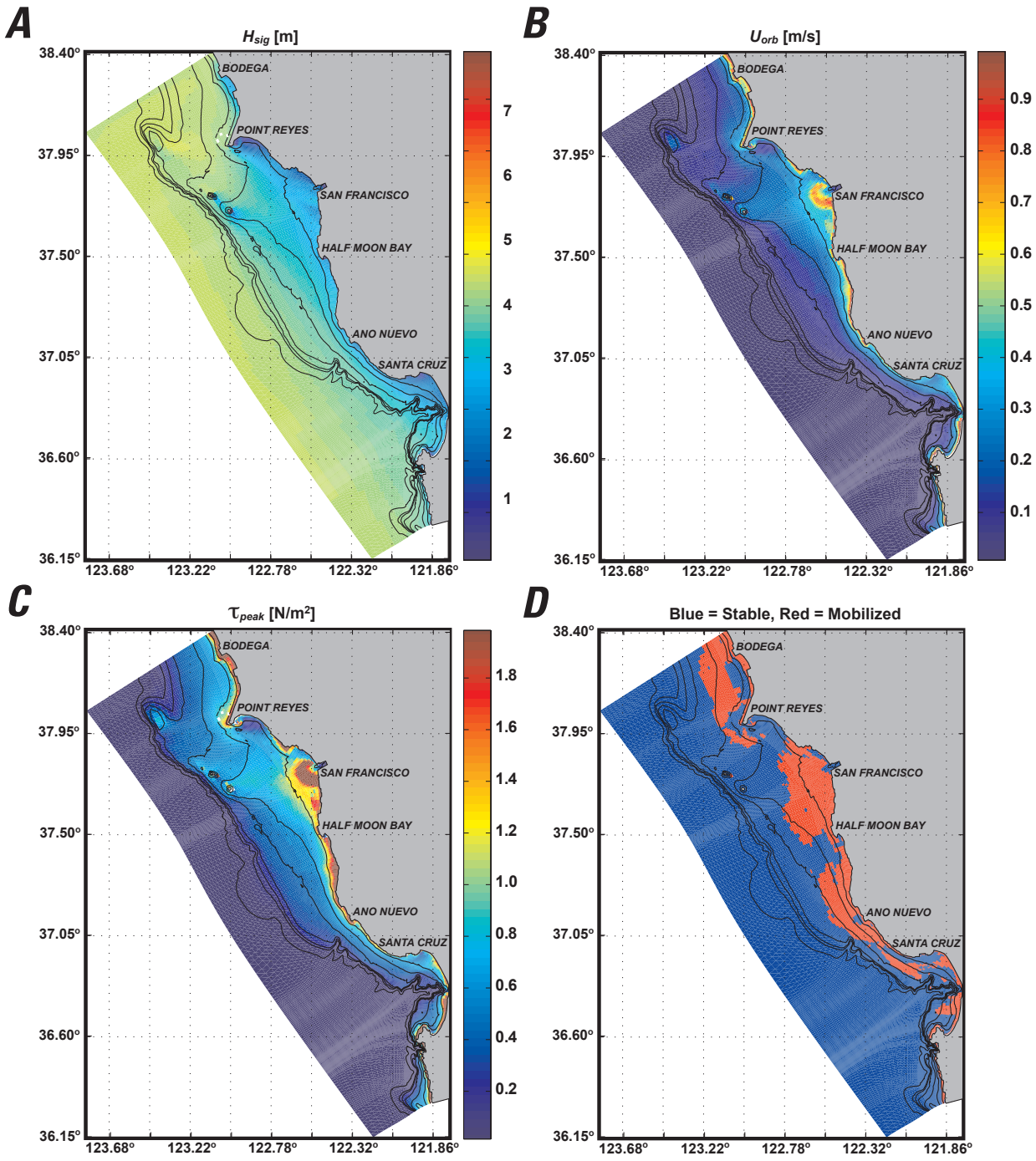

Appendix 10. Model run for a Normal October. *A*, Map of significant wave height (H_{sig}), in m. *B*, Map of peak wave-induced near-bed orbital wave velocity (U_{orb}), in m/s. *C*, Map of peak wave-induced near-bed shear stress (τ_{peak}), in N/m^2. *D*, Map displaying which regions of the study area are mobilized (red) and which are stable (blue) for the modeled conditions. See table 2 for information on model run boundary conditions.

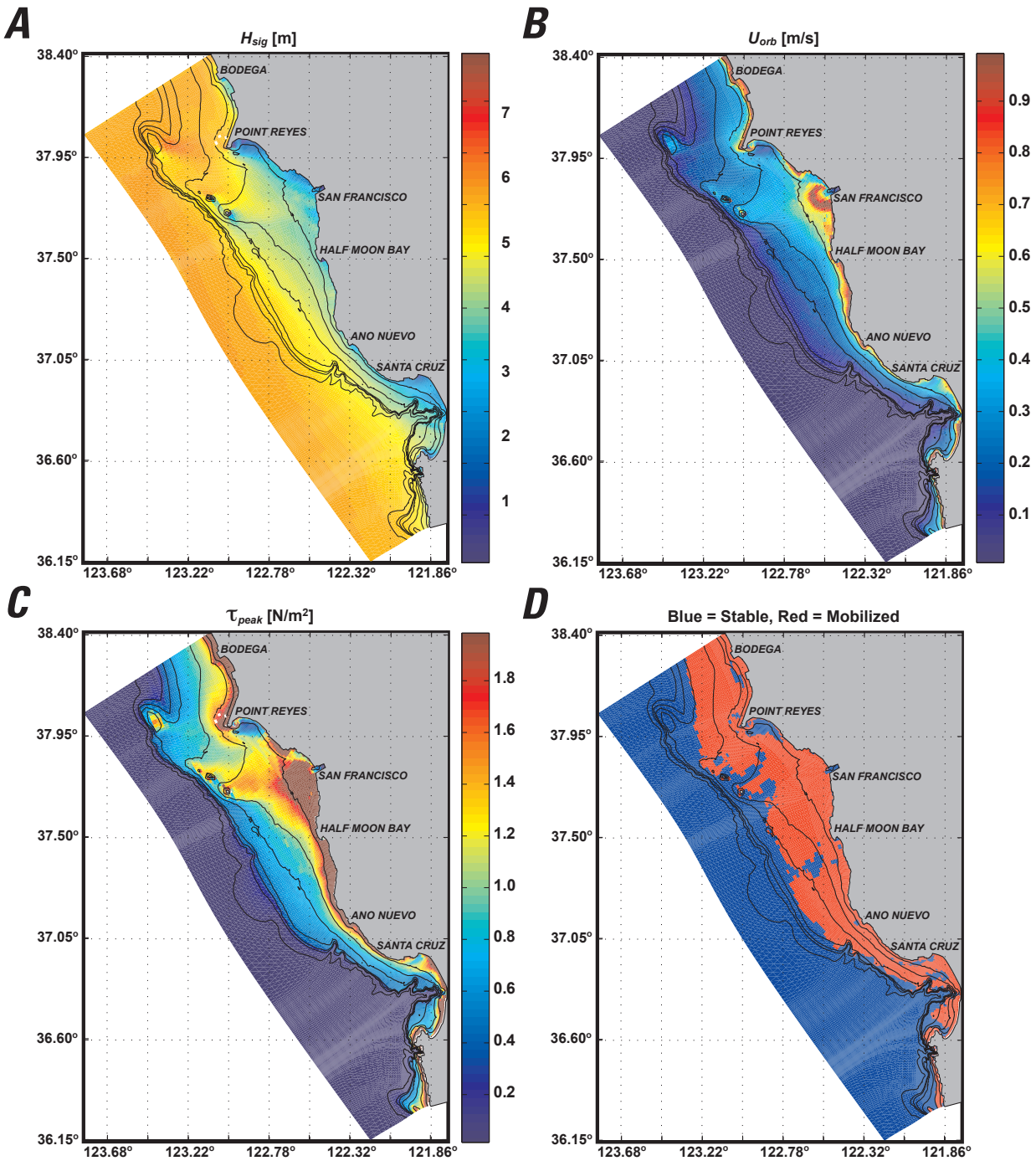

Appendix 11. Model run for a Normal November. *A*, Map of significant wave height (H_{sig}), in m. *B*, Map of peak wave-induced near-bed orbital wave velocity (U_{orb}), in m/s. *C*, Map of peak wave-induced near-bed shear stress (τ_{peak}), in N/m^2. *D*, Ma p displaying which regions of the study area are mobilized (red) and which are stable (blue) for the modeled conditions. See table 2 for information on model run boundary conditions.

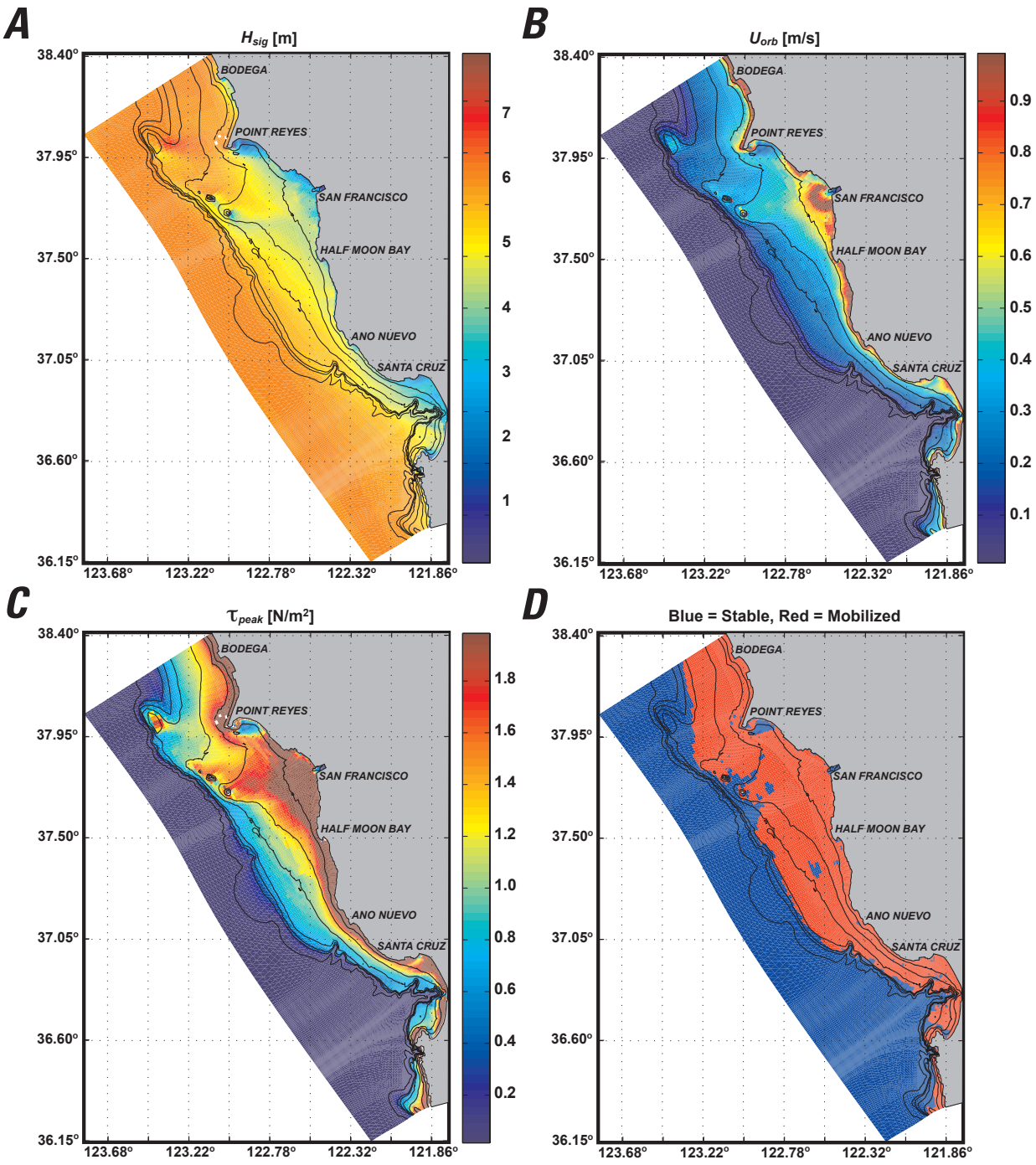

Appendix 12. Model run for a Normal December. *A*, Map of significant wave height (H_{sig}), in m. *B*, Map of peak wave-induced near-bed orbital wave velocity (U_{orb}), in m/s. *C*, Map of peak wave-induced near-bed shear stress (τ_{peak}), in N/m^2. *D*, Map displaying which regions of the study area are mobilized (red) and which are stable (blue) for the modeled conditions. See table 2 for information on model run boundary conditions.

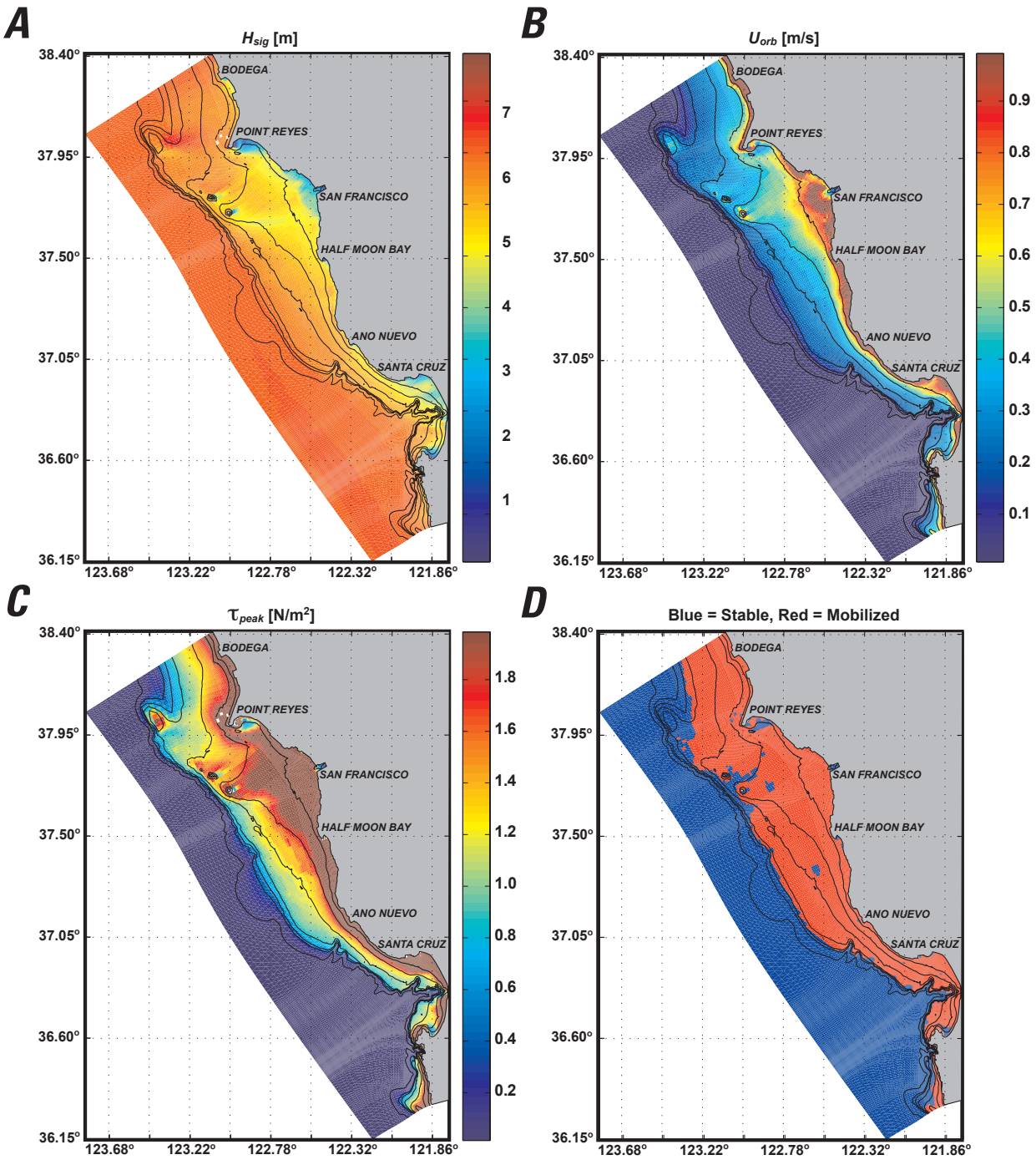

Appendix 13. Model run for an El Niño January. *A*, Map of significant wave height (H_{sig}), in m. *B*, Map of peak wave-induced near-bed orbital wave velocity (U_{orb}), in m/s. *C*, Map of peak wave-induced near-bed shear stress (τ_{peak}), in N/m^2. *D*, Map displaying which regions of the study area are mobilized (red) and which are stable (blue) for the modeled conditions. See table 2 for information on model run boundary conditions.

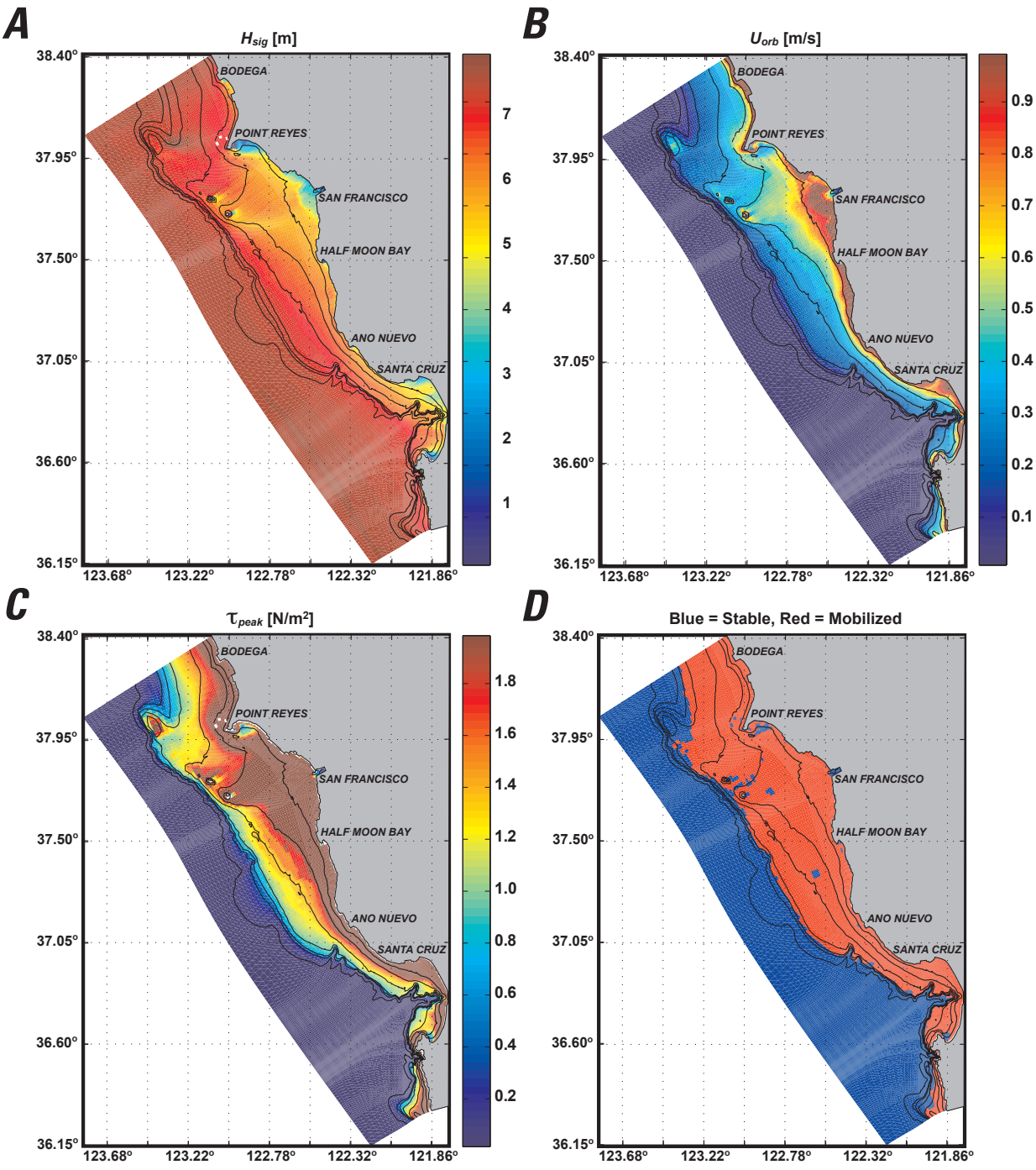

Appendix 14. Model run for an El Niño February. *A*, Map of significant wave height (H_{sig}), in m. *B*, Map of peak wave-induced near-bed orbital wave velocity (U_{orb}), in m/s. *C*, Map of peak wave-induced near-bed shear stress (τ_{peak}), in N/m^2. *D*, Map displaying which regions of the study area are mobilized (red) and which are stable (blue) for the modeled conditions. See table 2 for information on model run boundary conditions.

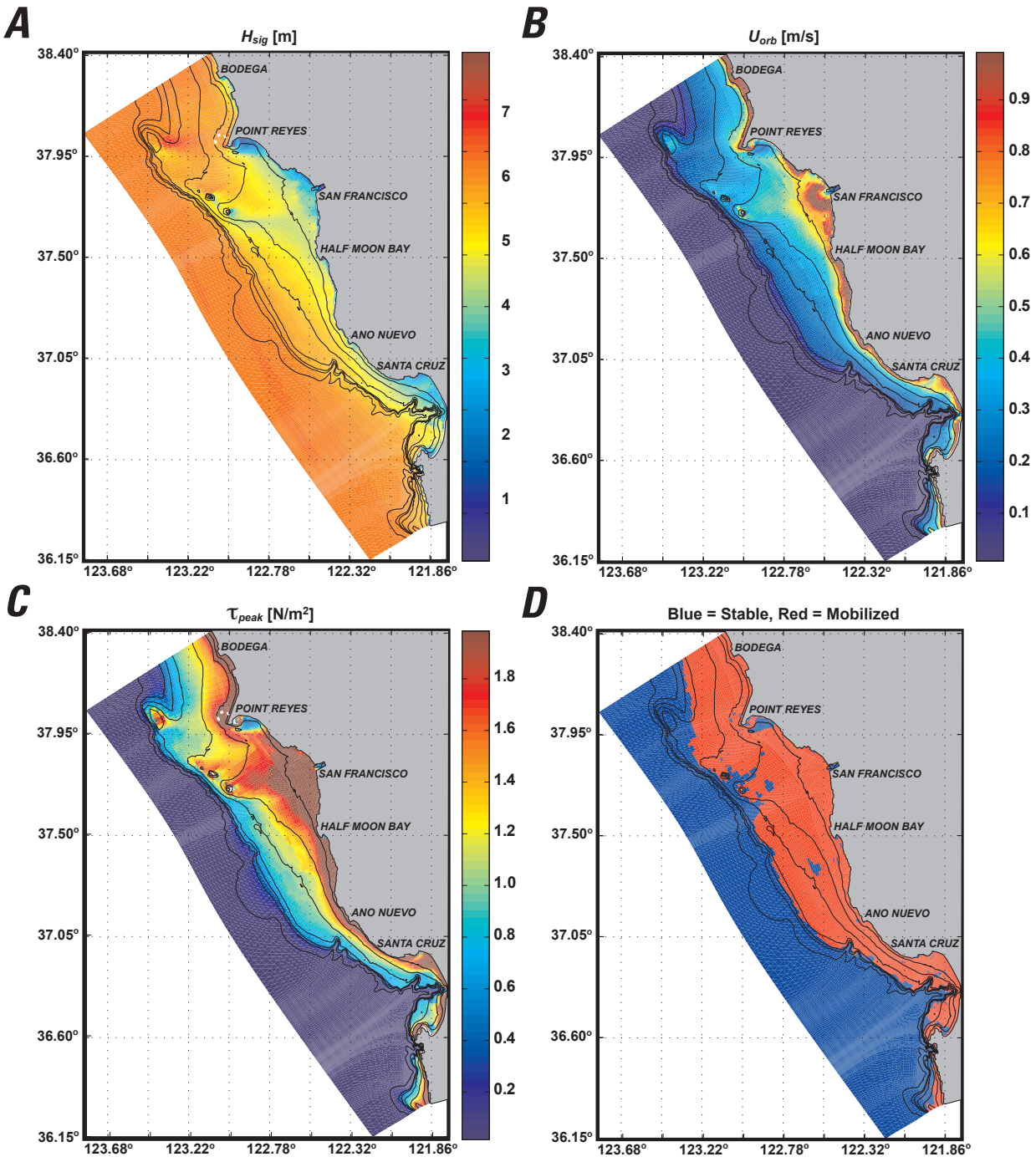

Appendix 15. Model run for an El Niño March. *A*, Map of significant wave height (H_{sig}), in m. *B*, Map of peak wave-induced near-bed orbital wave velocity (U_{orb}), in m/s. *C*, Map of peak wave-induced near-bed shear stress (τ_{peak}), in N/m^2. *D*, Map displaying which regions of the study area are mobilized (red) and which are stable (blue) for the modeled conditions. See table 2 for information on model run boundary conditions.

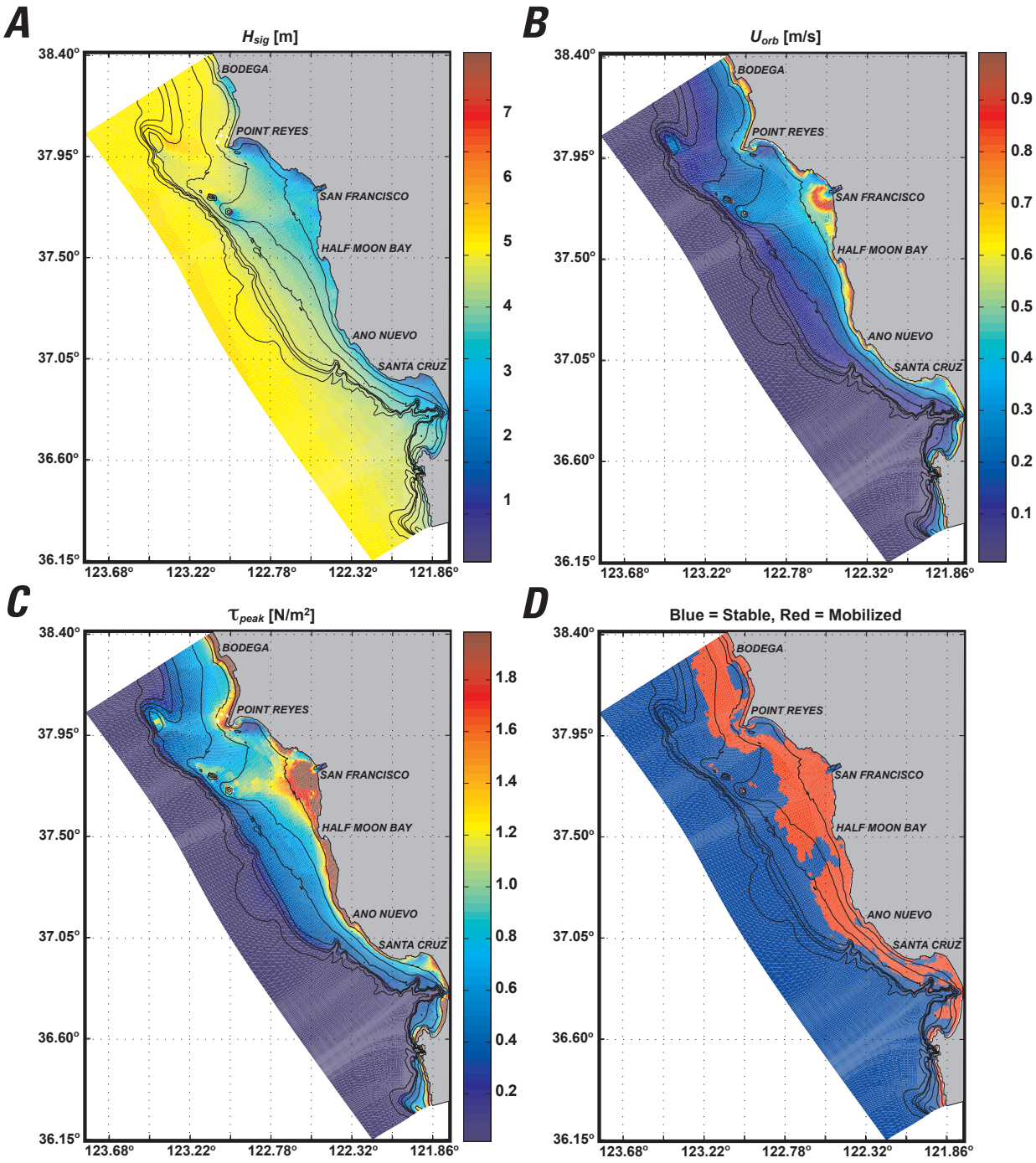

Appendix 16. Model run for an El Niño April. *A*, Map of significant wave height (H_{sig}), in m. *B*, Map of peak wave-induced near-bed orbital wave velocity (U_{orb}), in m/s. *C*, Map of peak wave-induced near-bed shear stress (τ_{peak}), in N/m^2. *D*, Map displaying which regions of the study area are mobilized (red) and which are stable (blue) for the modeled conditions. See table 2 for information on model run boundary conditions.

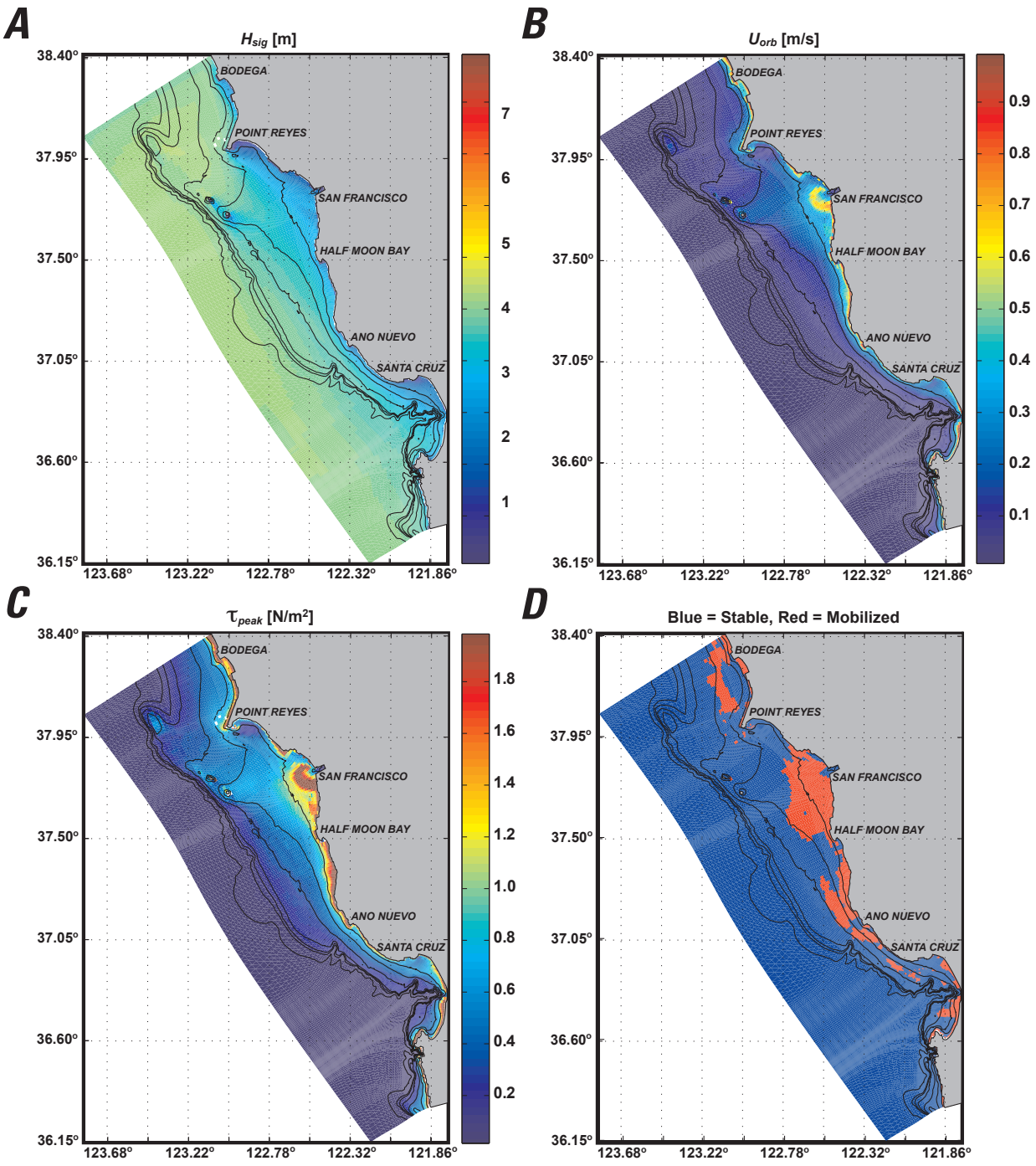

Appendix 17. Model run for an El Niño May. *A*, Map of significant wave height (H_{sig}), in m. *B*, Map of peak wave-induced near-bed orbital wave velocity (U_{orb}), in m/s. *C*, Map of peak wave-induced near-bed shear stress (τ_{peak}), in N/m^2. *D*, Map displaying which regions of the study area are mobilized (red) and which are stable (blue) for the modeled conditions. See table 2 for information on model run boundary conditions.

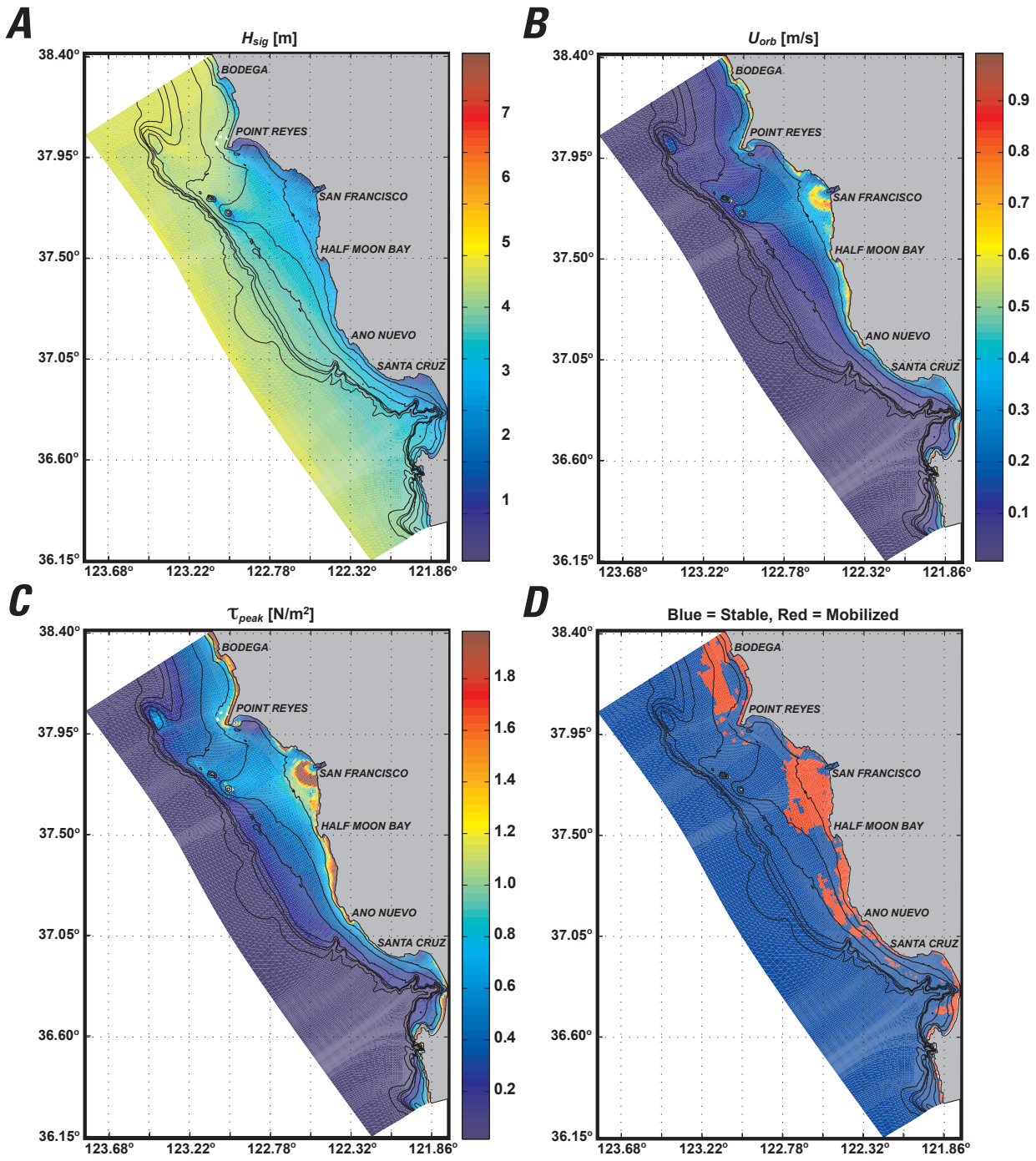

Appendix 18. Model run for an El Niño June. *A*, Map of significant wave height (H_{sig}), in m. *B*, Map of peak wave-induced near-bed orbital wave velocity (U_{orb}), in m/s. *C*, Map of peak wave-induced near-bed shear stress (τ_{peak}), in N/m^2. *D*, Map displaying which regions of the study area are mobilized (red) and which are stable (blue) for the modeled conditions. See table 2 for information on model run boundary conditions.

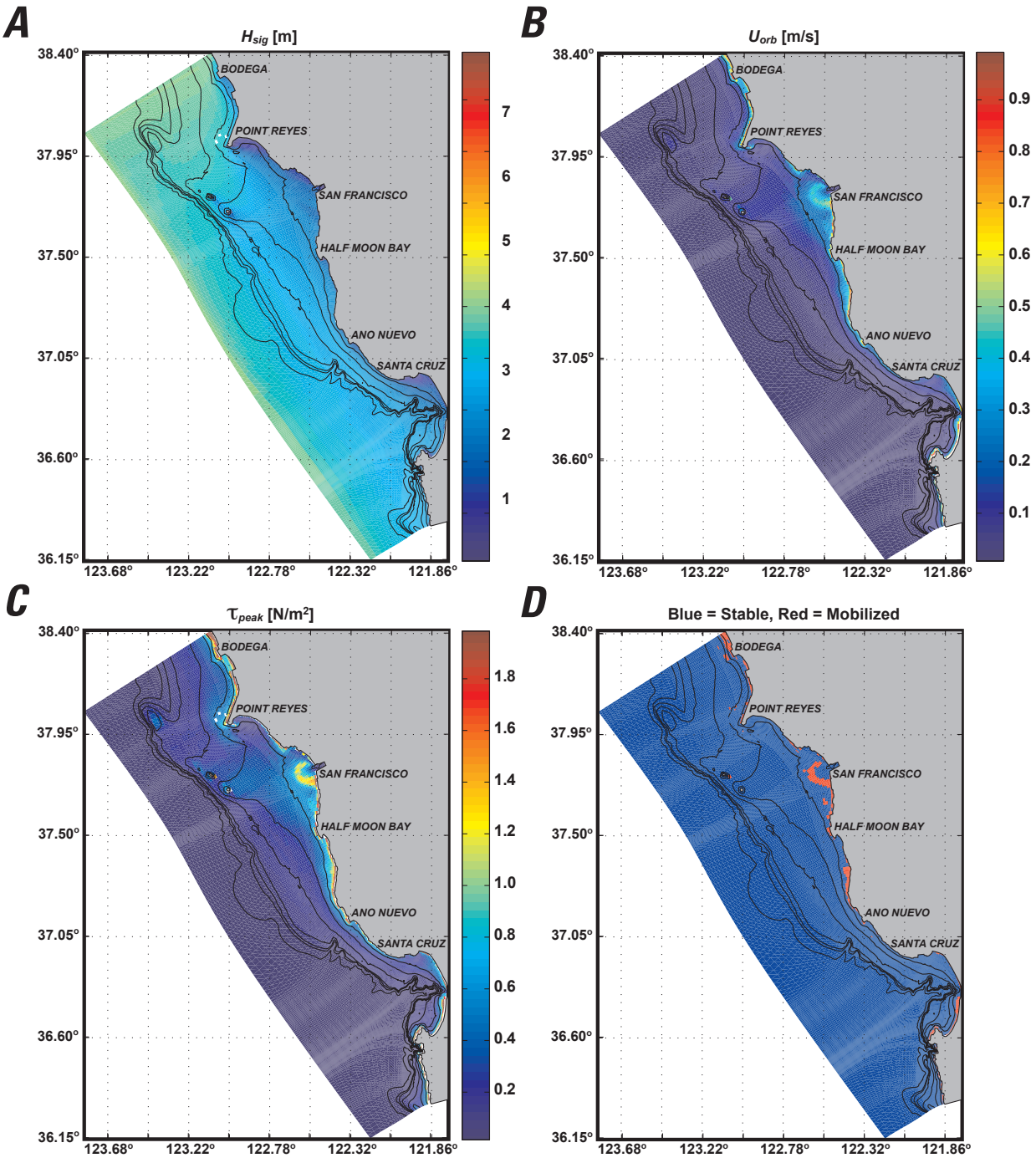

Appendix 19. Model run for an El Niño July. *A*, Map of significant wave height (H_{sig}), in m. *B*, Map of peak wave-induced near-bed orbital wave velocity (U_{orb}), in m/s. *C*, Map of peak wave-induced near-bed shear stress (τ_{peak}), in N/m^2. *D*, Map displaying which regions of the study area are mobilized (red) and which are stable (blue) for the modeled conditions. See table 2 for information on model run boundary conditions.

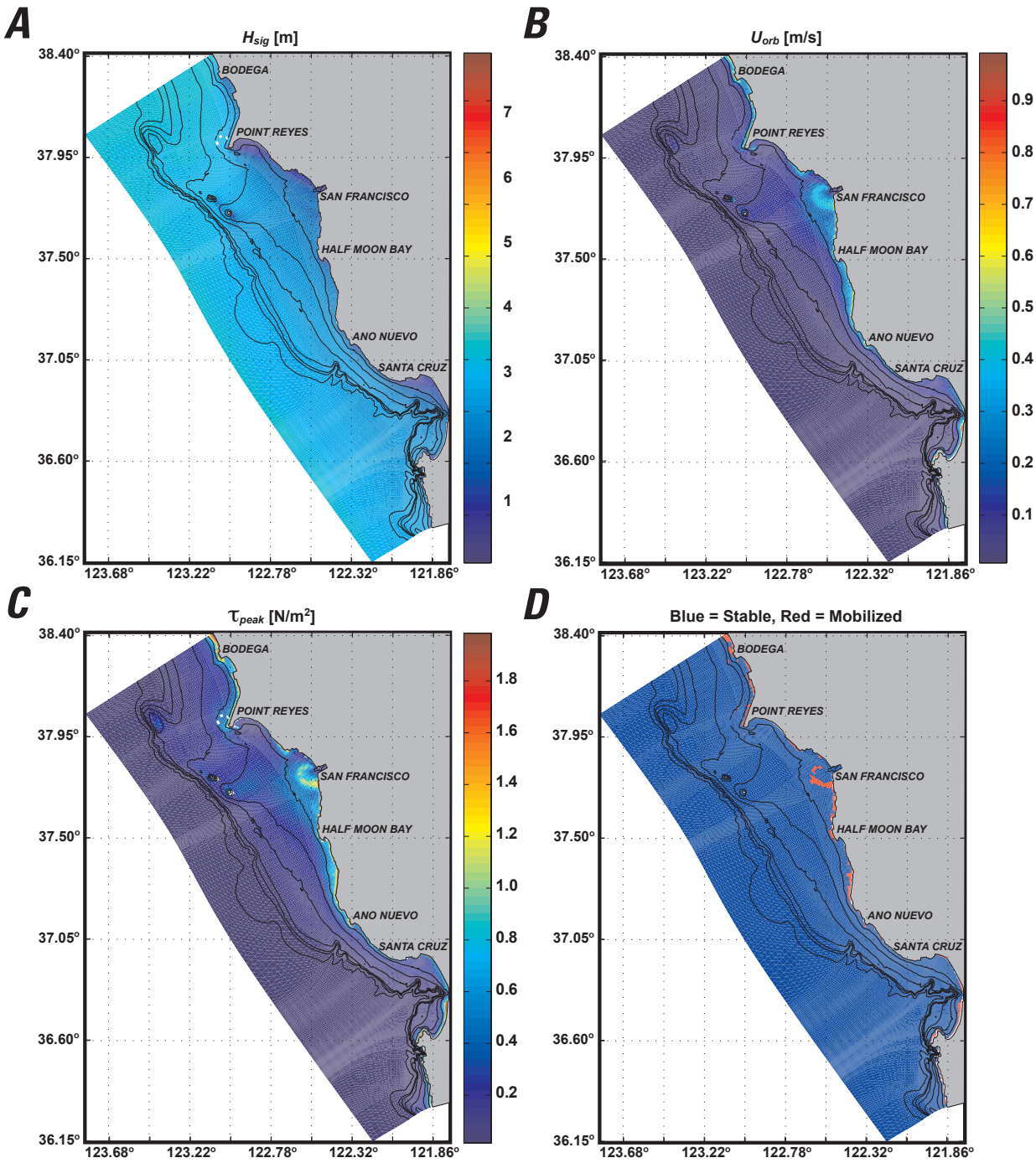

Appendix 20. Model run for an El Niño August. *A*, Map of significant wave height (H_{sig}), in m. *B*, Map of peak wave-induced near-bed orbital wave velocity (U_{orb}), in m/s. *C*, Map of peak wave-induced near-bed shear stress (τ_{peak}), in N/m^2. *D*, Map displaying which regions of the study area are mobilized (red) and which are stable (blue) for the modeled conditions. See table 2 for information on model run boundary conditions.

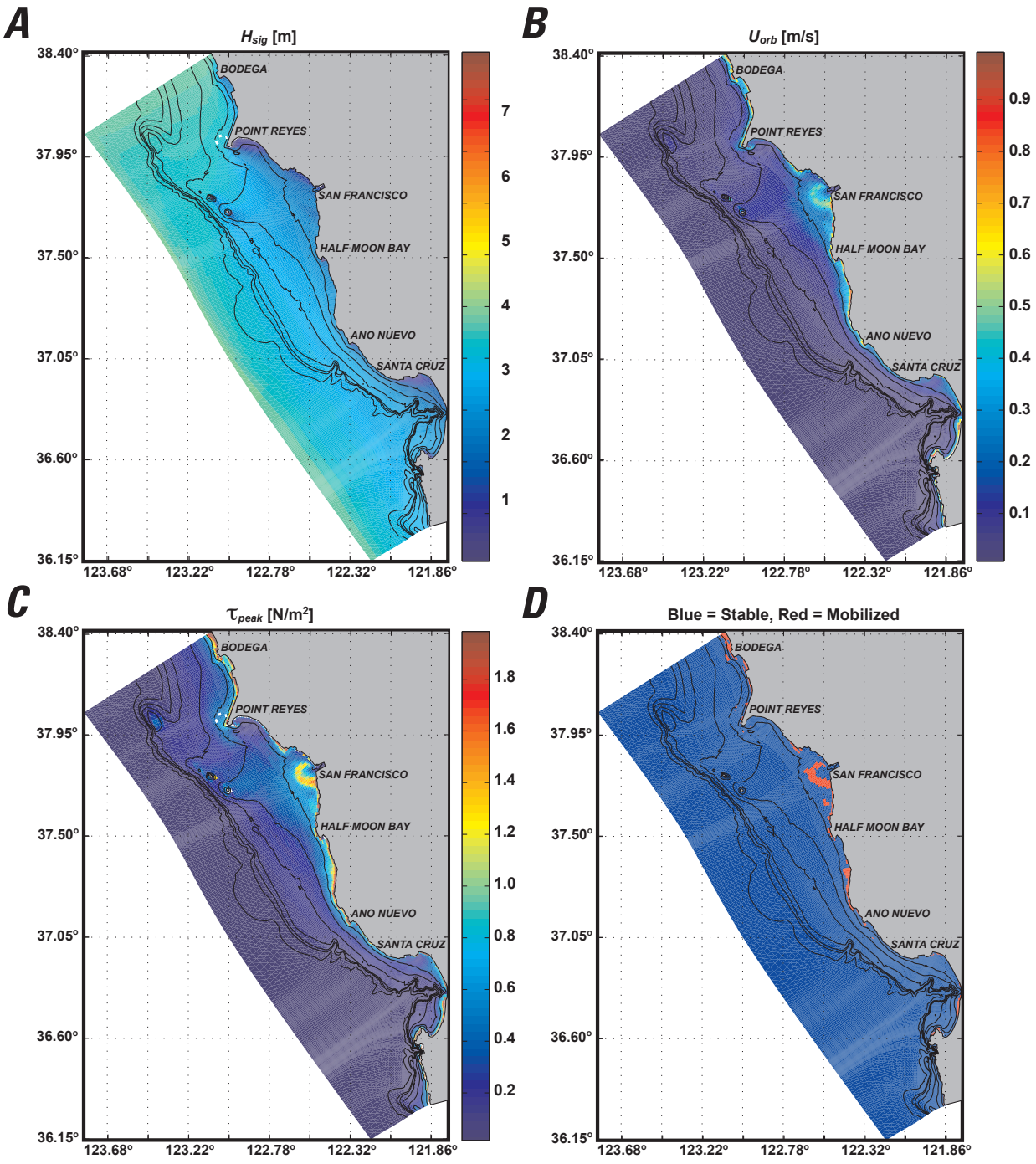

Appendix 21. Model run for an El Niño September. *A*, Map of significant wave height (H_{sig}), in m. *B*, Map of peak wave-induced near-bed orbital wave velocity (U_{orb}), in m/s. *C*, Map of peak wave-induced near-bed shear stress (τ_{peak}), in N/m^2. *D*, Map displaying which regions of the study area are mobilized (red) and which are stable (blue) for the modeled conditions. See table 2 for information on model run boundary conditions.

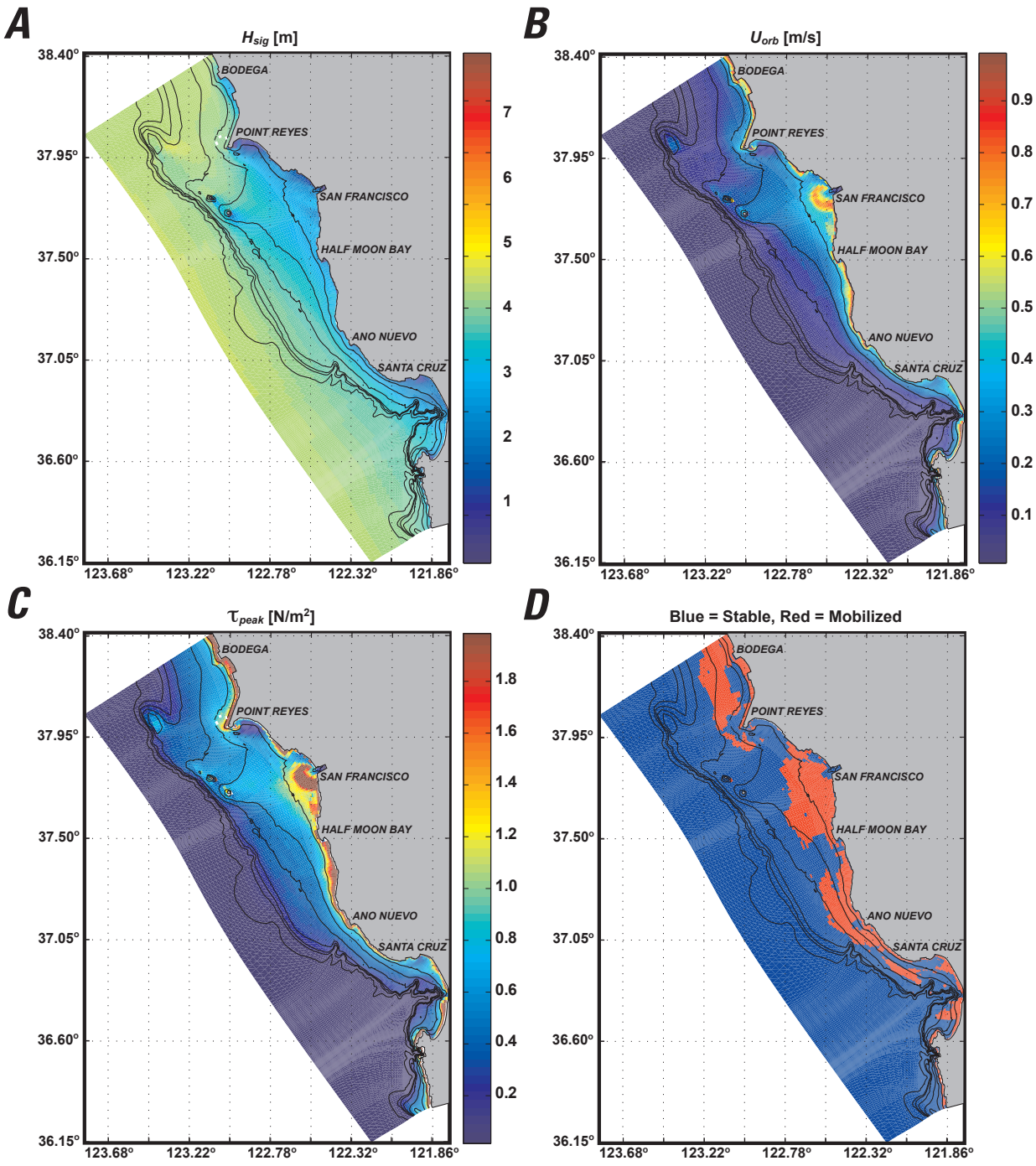

Appendix 22. Model run for an El Niño October. *A*, Map of significant wave height (H_{sig}), in m. *B*, Map of peak wave-induced near-bed orbital wave velocity (U_{orb}), in m/s. *C*, Map of peak wave-induced near-bed shear stress (τ_{peak}), in N/m^2. *D*, Map displaying which regions of the study area are mobilized (red) and which are stable (blue) for the modeled conditions. See table 2 for information on model run boundary conditions.

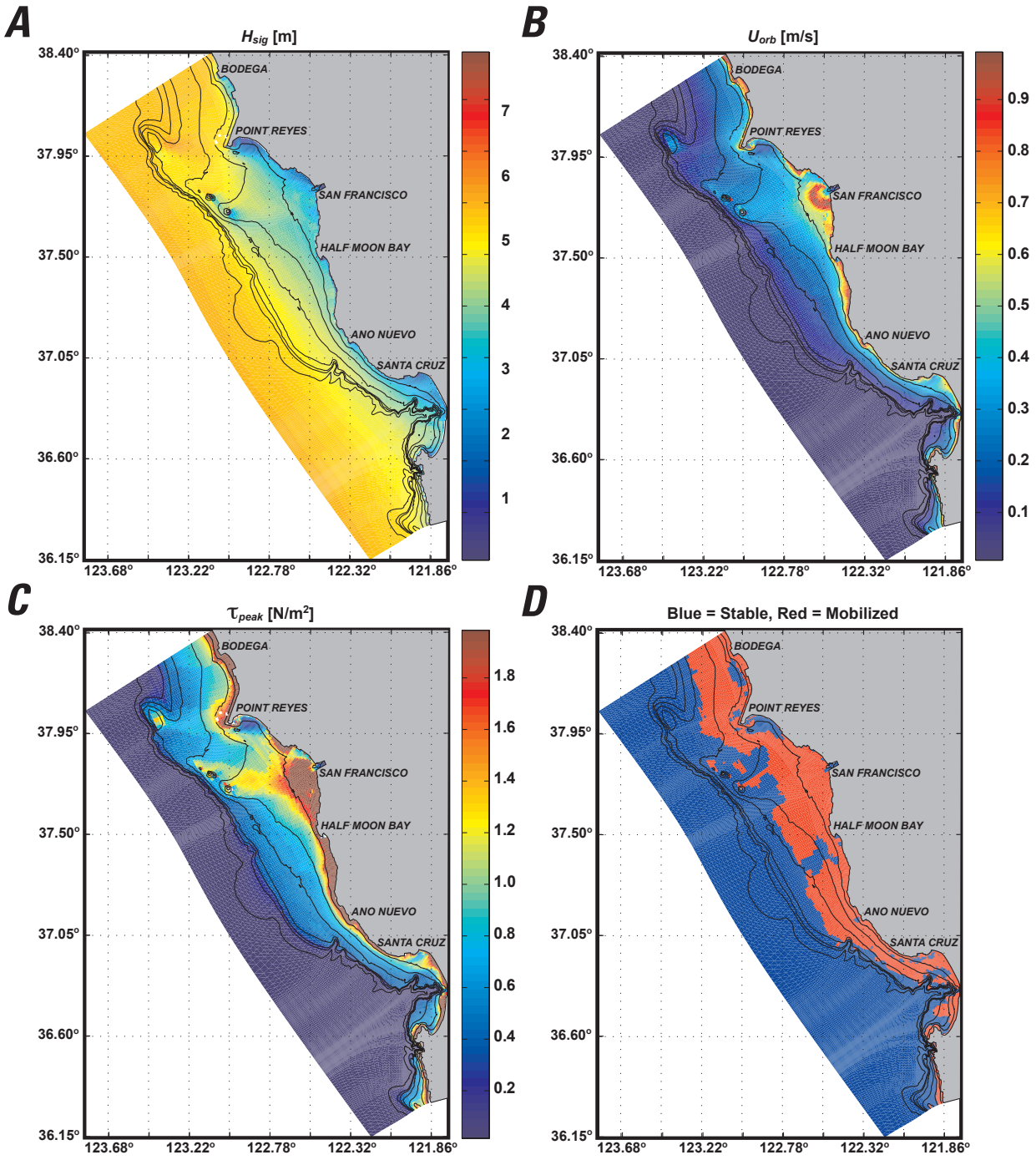

Appendix 23. Model run for an El Niño November. *A*, Map of significant wave height (H_{sig}), in m. *B*, Map of peak wave-induced near-bed orbital wave velocity (U_{orb}), in m/s. *C*, Map of peak wave-induced near-bed shear stress (τ_{peak}), in N/m^2. *D*, Map displaying which regions of the study area are mobilized (red) and which are stable (blue) for the modeled conditions. See table 2 for information on model run boundary conditions.

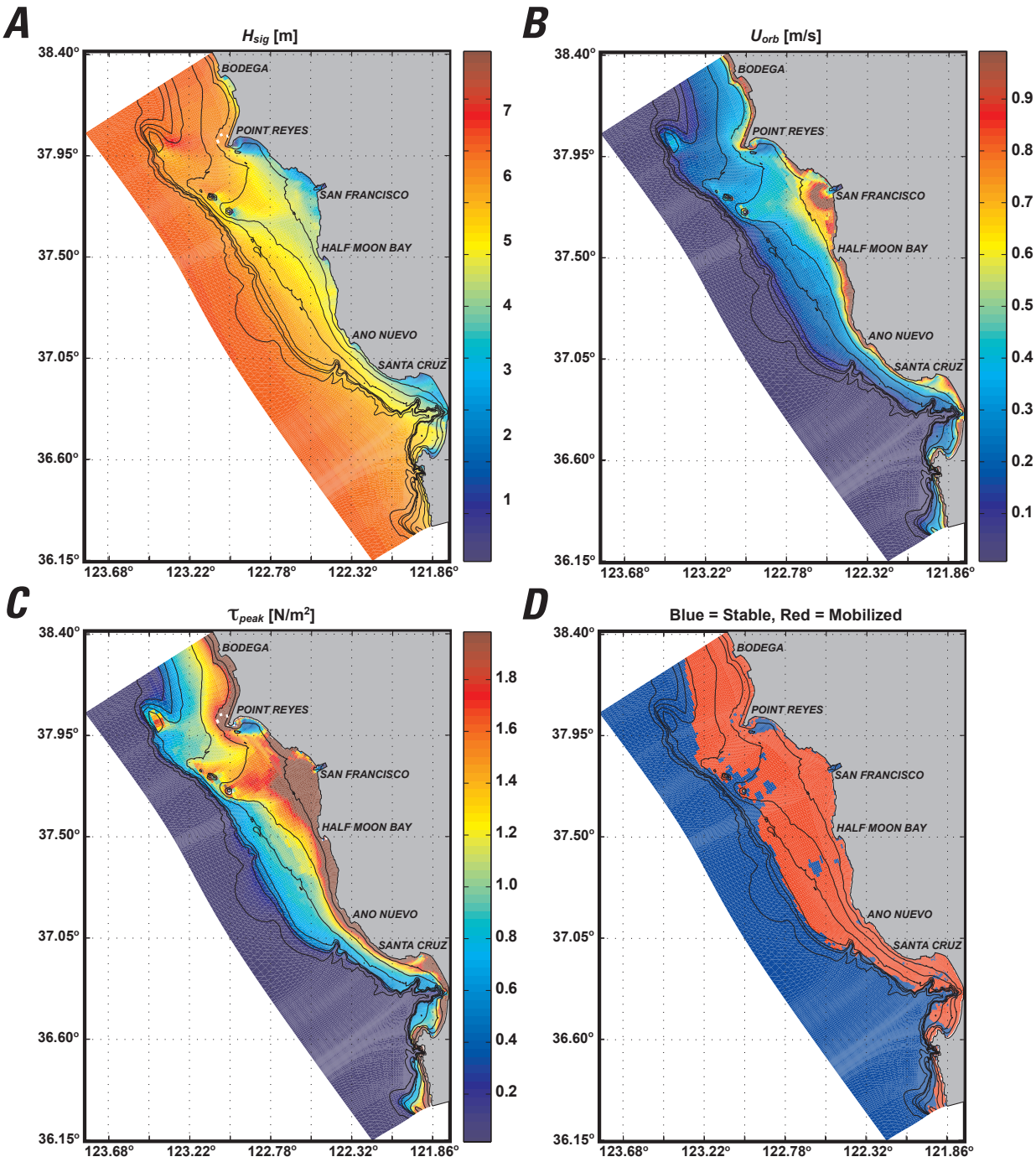

Appendix 24. Model run for an El Niño December. *A*, Map of significant wave height (H_{sig}), in m. *B*, Map of peak wave-induced near-bed orbital wave velocity (U_{orb}), in m/s. *C*, Map of peak wave-induced near-bed shear stress (τ_{peak}), in N/m^2. *D*, Map displaying which regions of the study area are mobilized (red) and which are stable (blue) for the modeled conditions. See table 2 for information on model run boundary conditions.

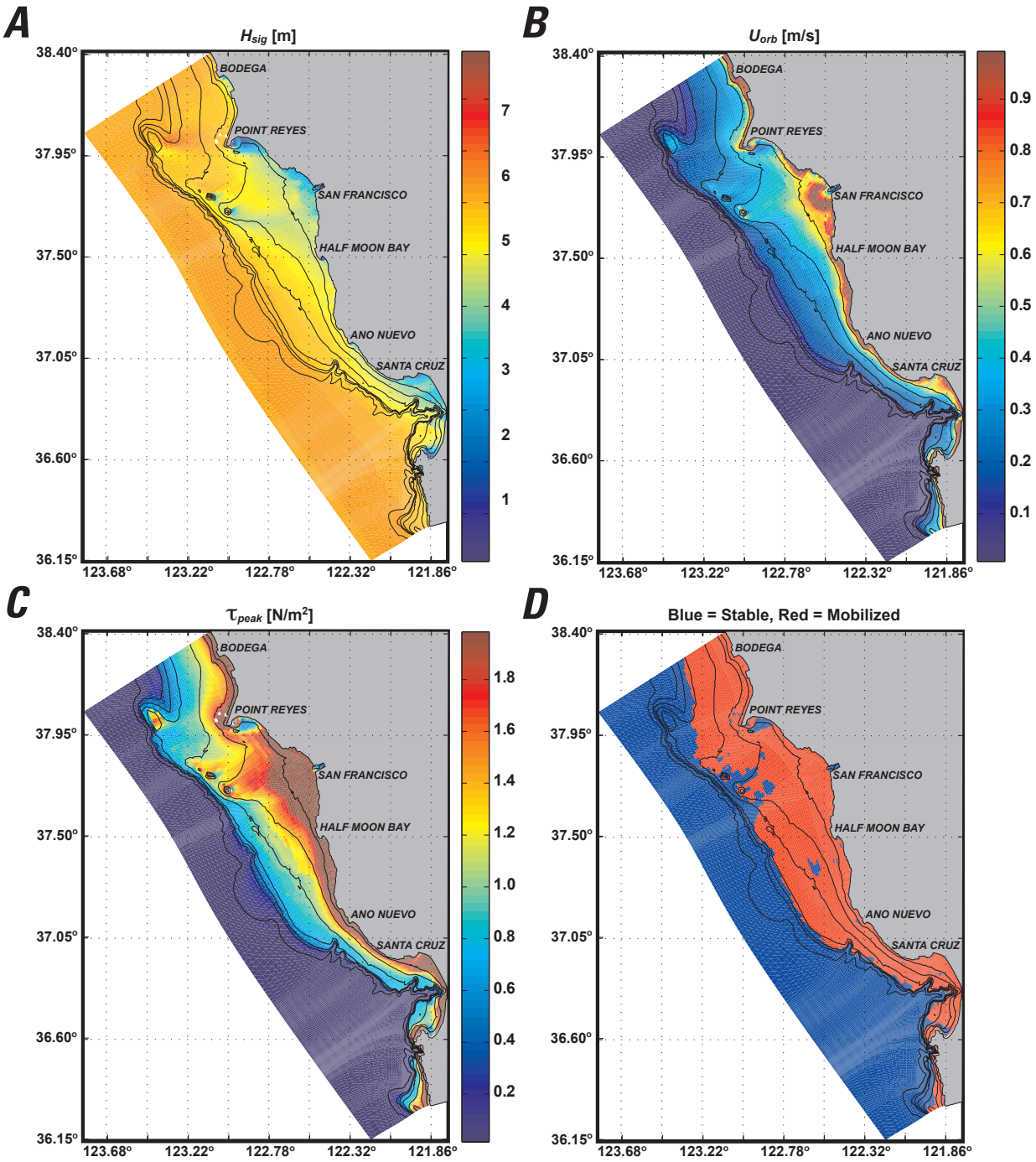

Appendix 25. Model run for a La Niña January. *A*, Map of significant wave height (H_{sig}), in m. *B*, Map of peak wave-induced near-bed orbital wave velocity (U_{orb}), in m/s. *C*, Map of peak wave-induced near-bed shear stress (τ_{peak}), in N/m^2. *D*, Map displaying which regions of the study area are mobilized (red) and which are stable (blue) for the modeled conditions. See table 2 for information on model run boundary conditions.

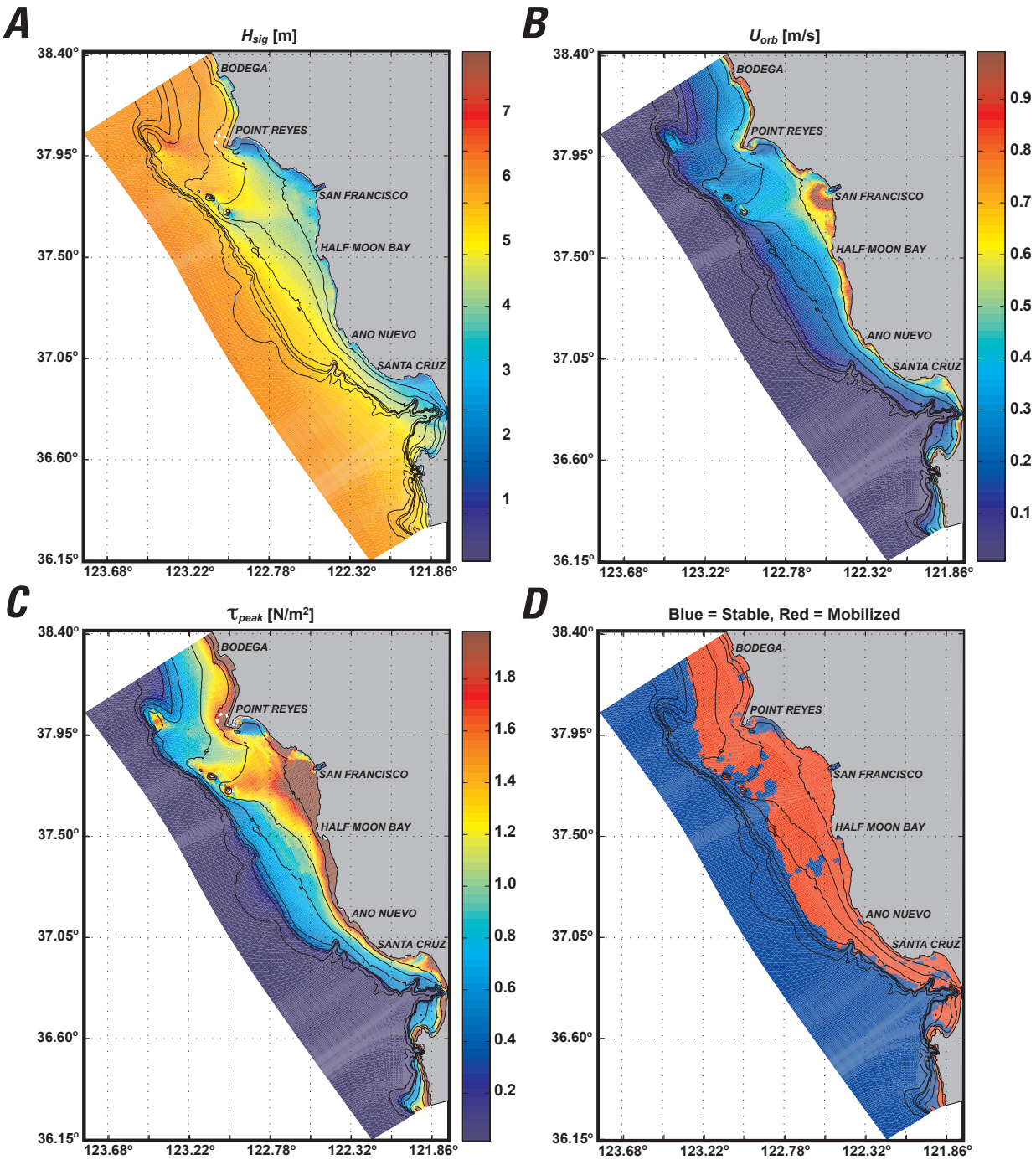

Appendix 26. Model run for a La Niña February. *A*, Map of significant wave height (H_{sig}), in m. *B*, Map of peak wave-induced near-bed orbital wave velocity (U_{orb}), in m/s. *C*, Map of peak wave-induced near-bed shear stress (τ_{peak}), in N/m^2. *D*, Map displaying which regions of the study area are mobilized (red) and which are stable (blue) for the modeled conditions. See table 2 for information on model run boundary conditions.

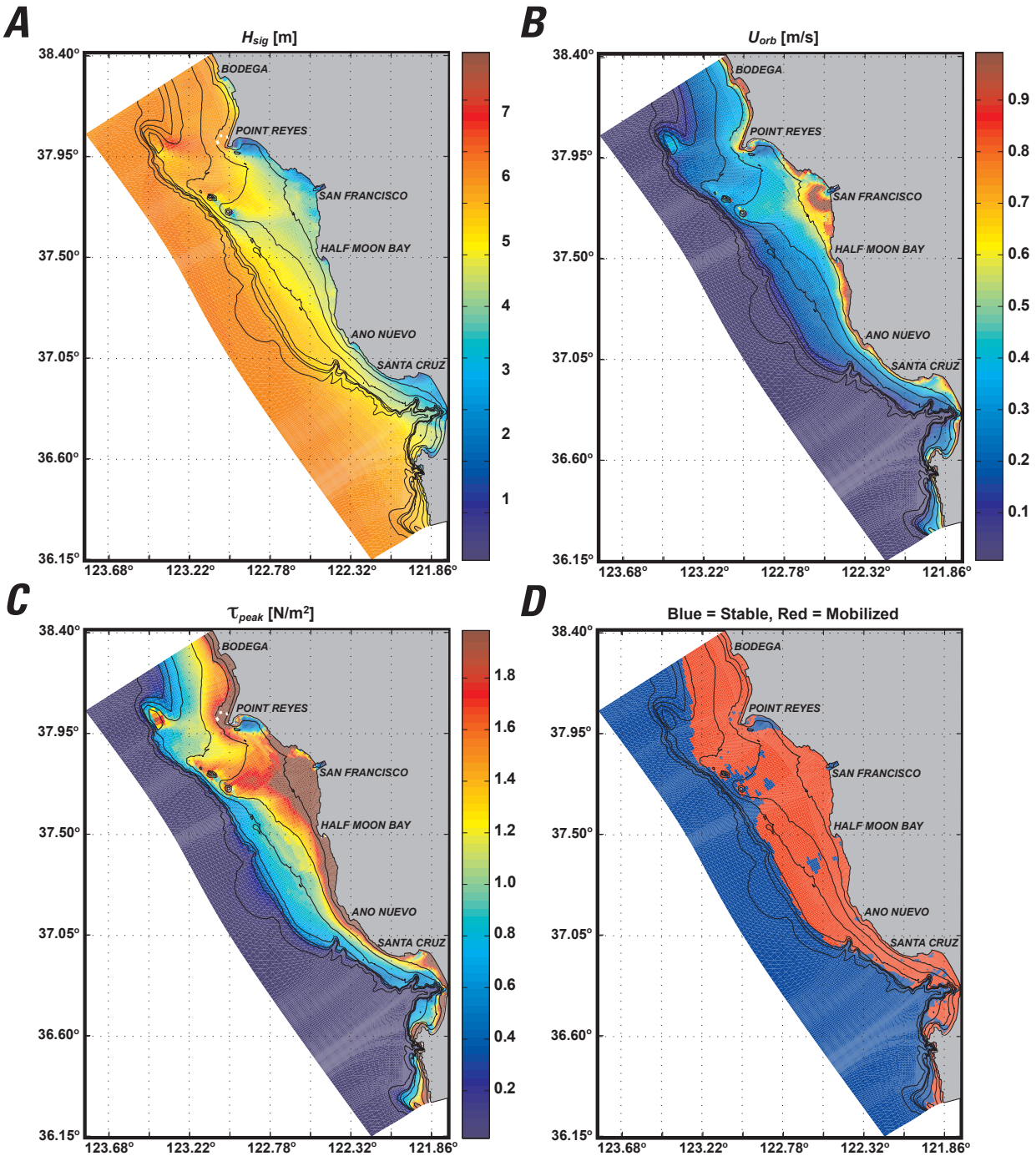

Appendix 27. Model run for a La Niña March. *A*, Map of significant wave height (H_{sig}), in m. *B*, Map of peak wave-induced near-bed orbital wave velocity (U_{orb}), in m/s. *C*, Map of peak wave-induced near-bed shear stress (τ_{peak}), in N/m^2. *D*, Map displaying which regions of the study area are mobilized (red) and which are stable (blue) for the modeled conditions. See table 2 for information on model run boundary conditions.

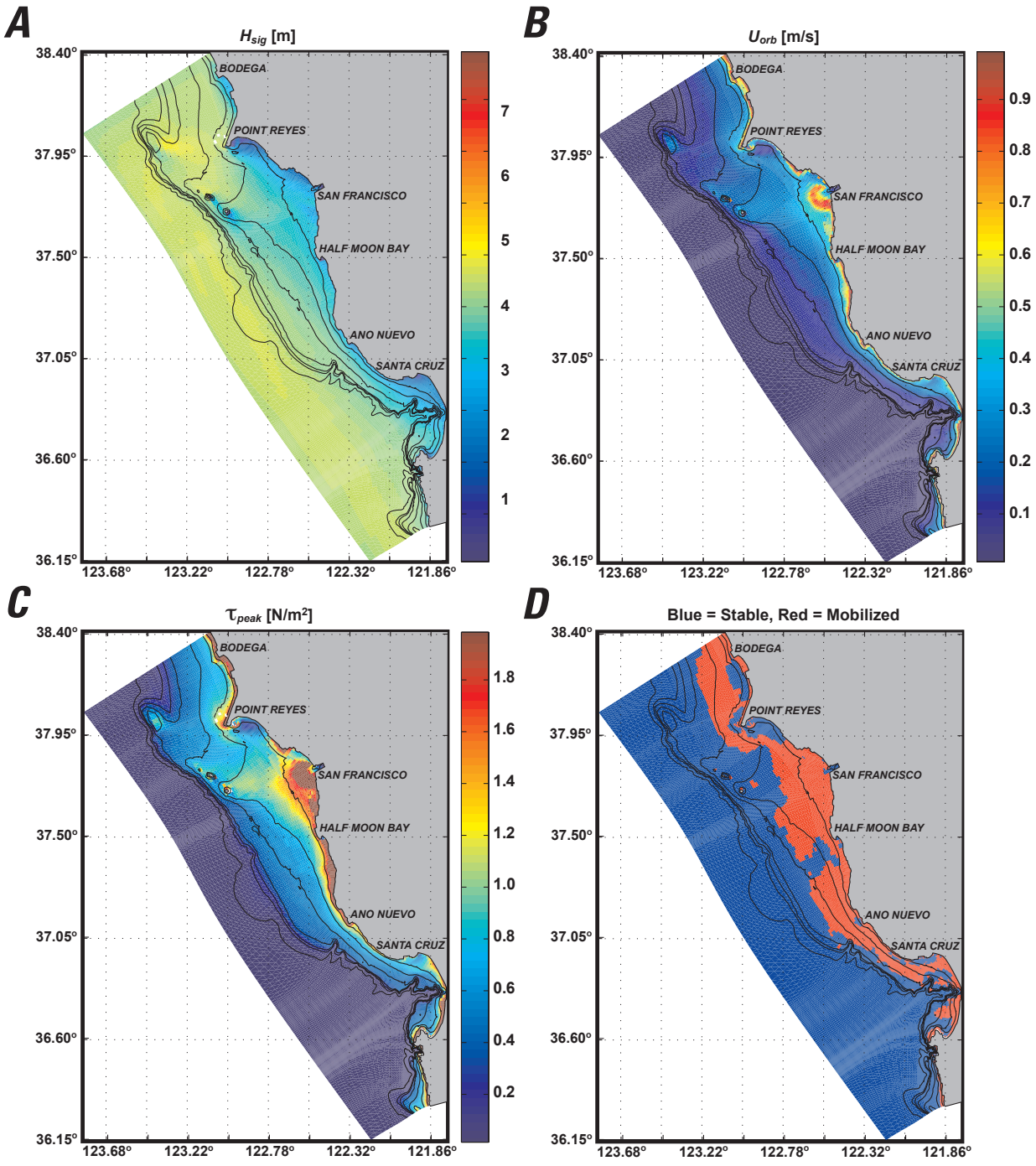

Appendix 28. Model run for a La Niña April. *A*, Map of significant wave height (H_{sig}), in m. *B*, Map of peak wave-induced near-bed orbital wave velocity (U_{orb}), in m/s. *C*, Map of peak wave-induced near-bed shear stress (τ_{peak}), in N/m^2. *D*, Map displaying which regions of the study area are mobilized (red) and which are stable (blue) for the modeled conditions. See table 2 for information on model run boundary conditions.

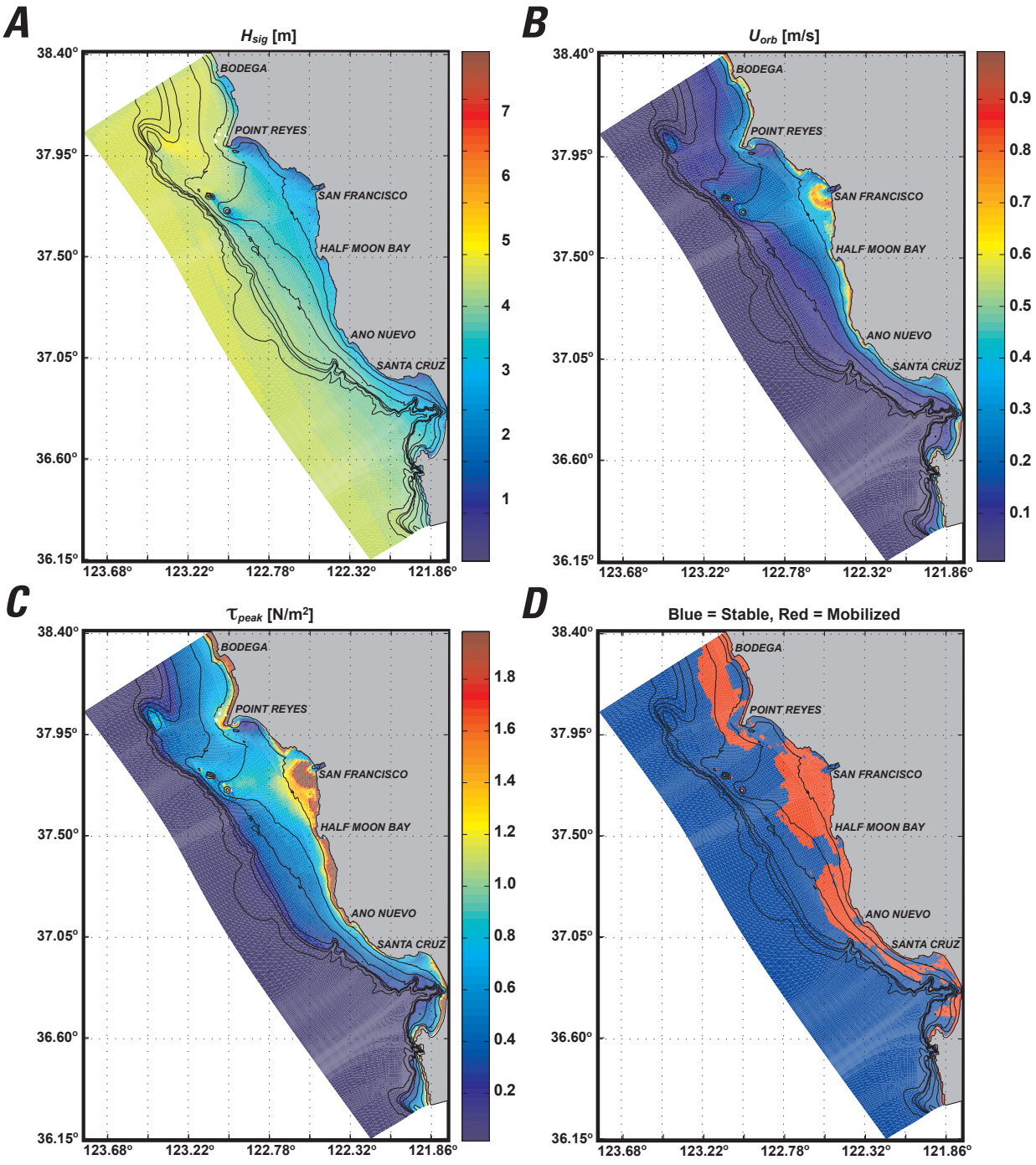

Appendix 29. Model run for a La Niña May. *A*, Map of significant wave height (H_{sig}), in m. *B*, Map of peak wave-induced near-bed orbital wave velocity (U_{orb}), in m/s. *C*, Map of peak wave-induced near-bed shear stress (τ_{peak}), in N/m^2. *D*, Map displaying which regions of the study area are mobilized (red) and which are stable (blue) for the modeled conditions. See table 2 for information on model run boundary conditions.

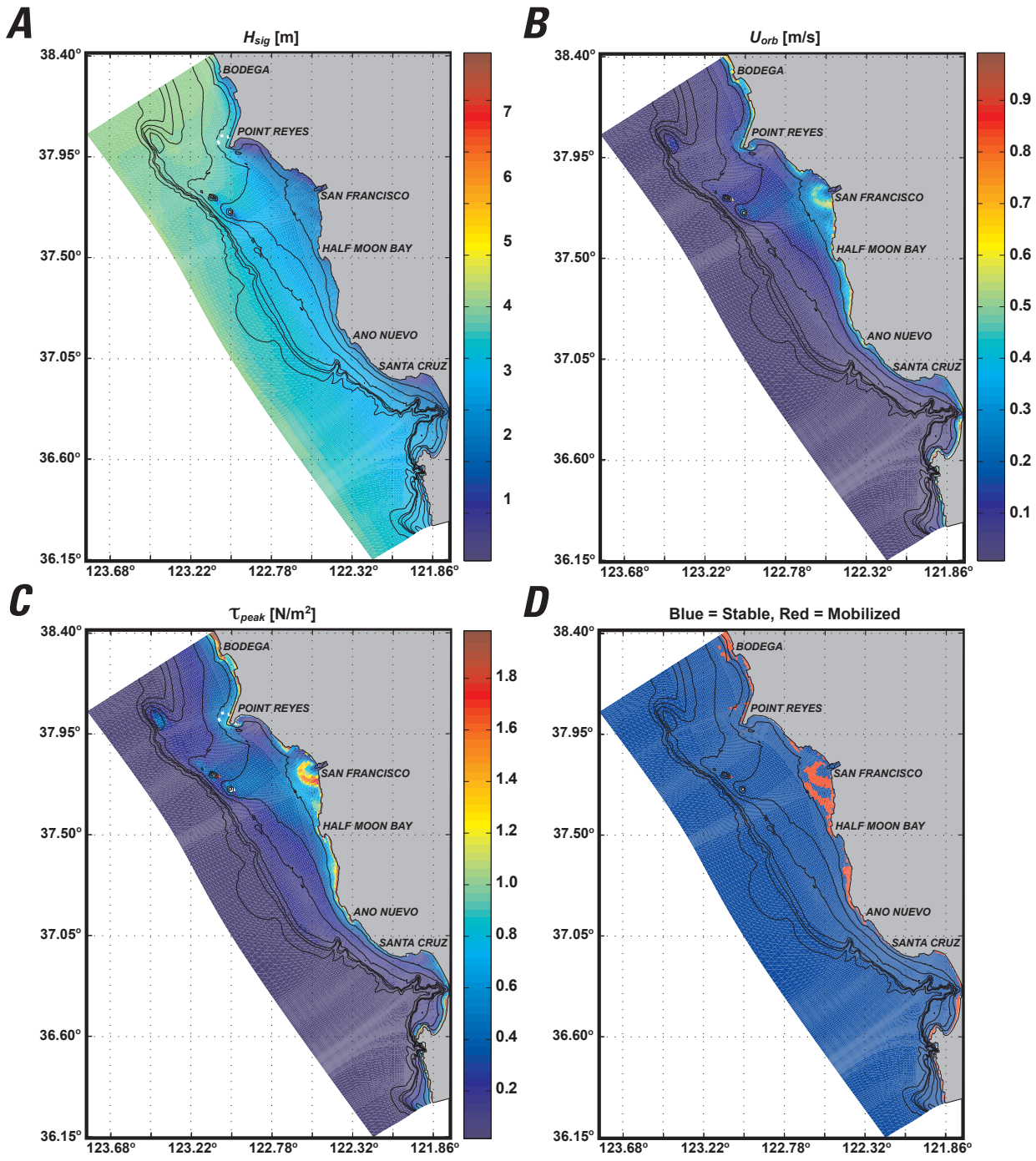

Appendix 30. Model run for a La Niña June. *A*, Map of significant wave height (H_{sig}), in m. *B*, Map of peak wave-induced near-bed orbital wave velocity (U_{orb}), in m/s. *C*, Map of peak wave-induced near-bed shear stress (τ_{peak}), in N/m^2. *D*, Map displaying which regions of the study area are mobilized (red) and which are stable (blue) for the modeled conditions. See table 2 for information on model run boundary conditions

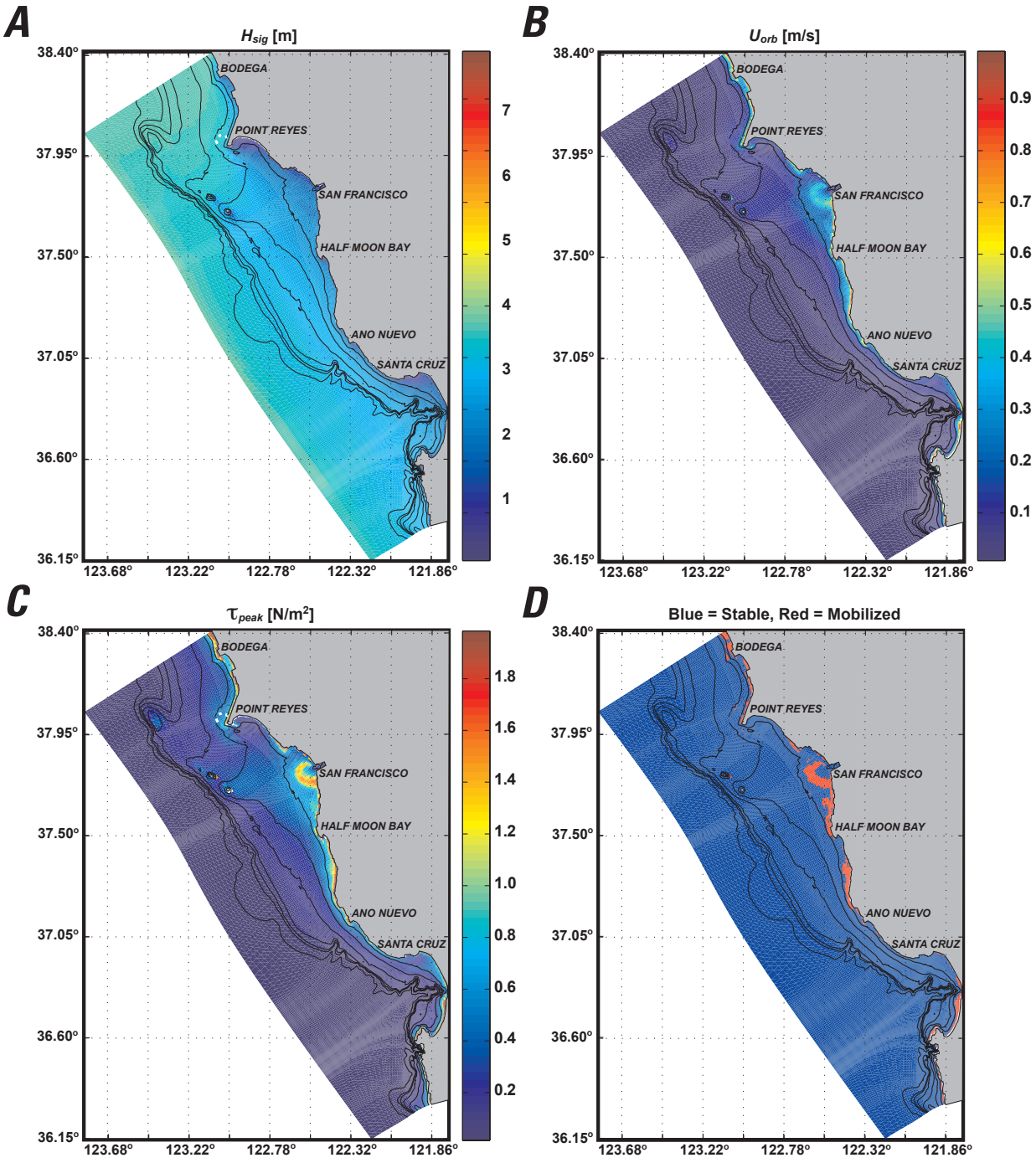

Appendix 31. Model run for a La Niña July. *A*, Map of significant wave height (H_{sig}), in m. *B*, Map of peak wave-induced near-bed orbital wave velocity (U_{orb}), in m/s. *C*, Map of peak wave-induced near-bed shear stress (τ_{peak}), in N/m^2. *D*, Map displaying which regions of the study area are mobilized (red) and which are stable (blue) for the modeled conditions. See table 2 for information on model run boundary conditions.

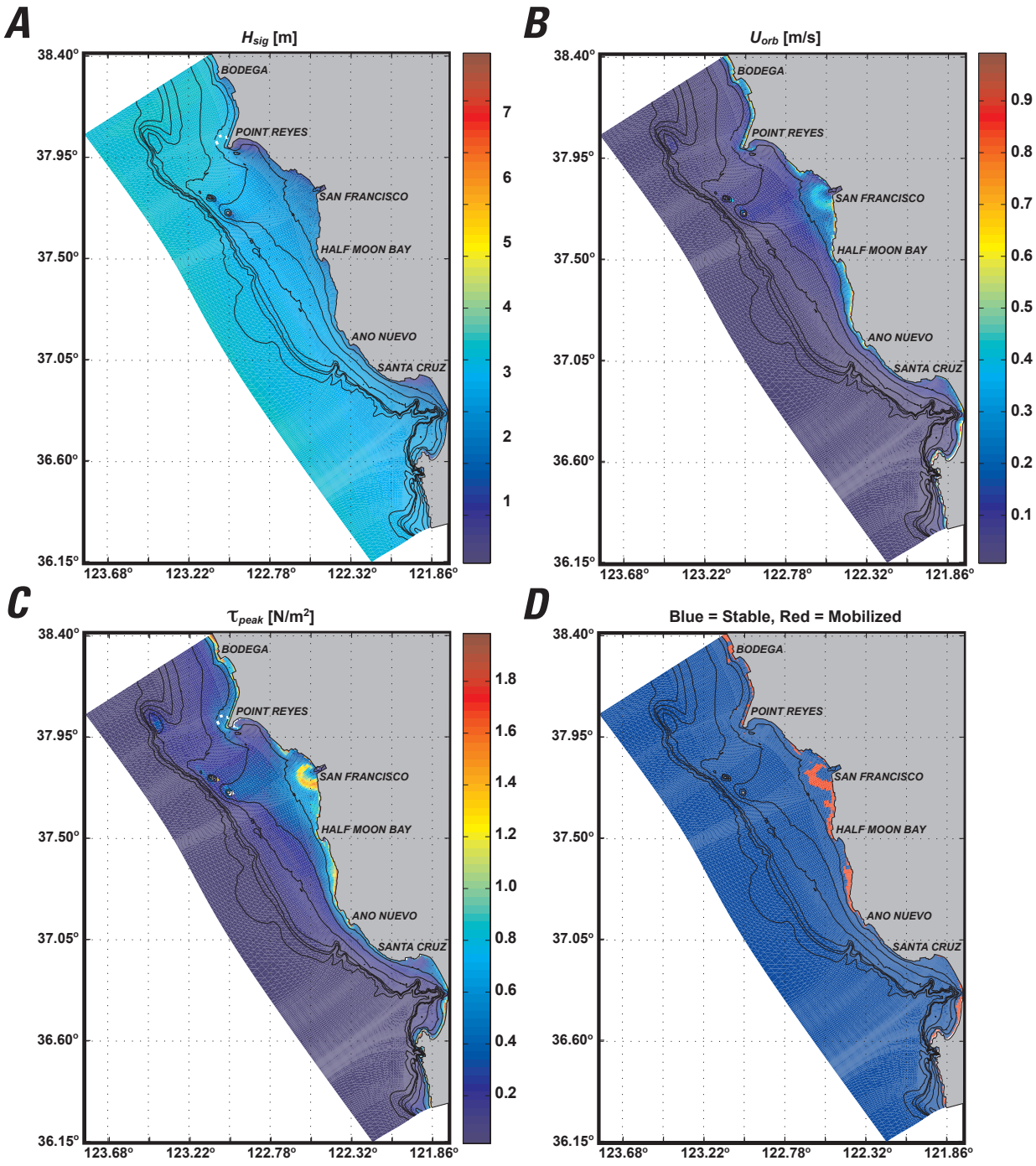

Appendix 32. Model run for a La Niña August. *A*, Map of significant wave height (H_{sig}), in m. *B*, Map of peak wave-induced near-bed orbital wave velocity (U_{orb}), in m/s. *C*, Map of peak wave-induced near-bed shear stress (τ_{peak}), in N/m^2. *D*, Map displaying which regions of the study area are mobilized (red) and which are stable (blue) for the modeled conditions. See table 2 for information on model run boundary conditions.

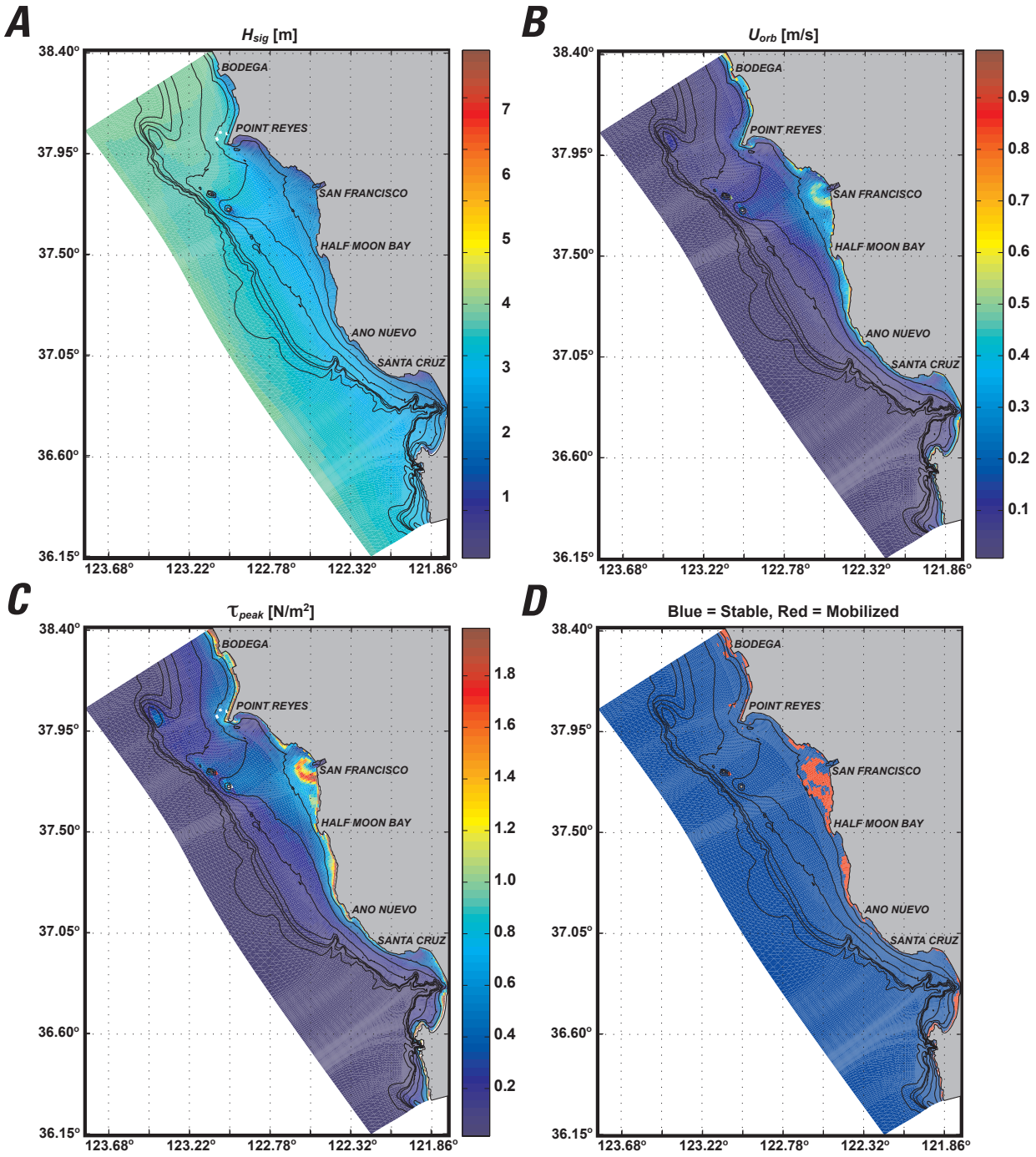

Appendix 33. Model run for a La Niña September. *A*, Map of significant wave height (H_{sig}), in m. *B*, Map of peak wave-induced near-bed orbital wave velocity (U_{orb}), in m/s. *C*, Map of peak wave-induced near-bed shear stress (τ_{peak}), in N/m^2. *D*, Map displaying which regions of the study area are mobilized (red) and which are stable (blue) for the modeled conditions. See table 2 for information on model run boundary conditions.

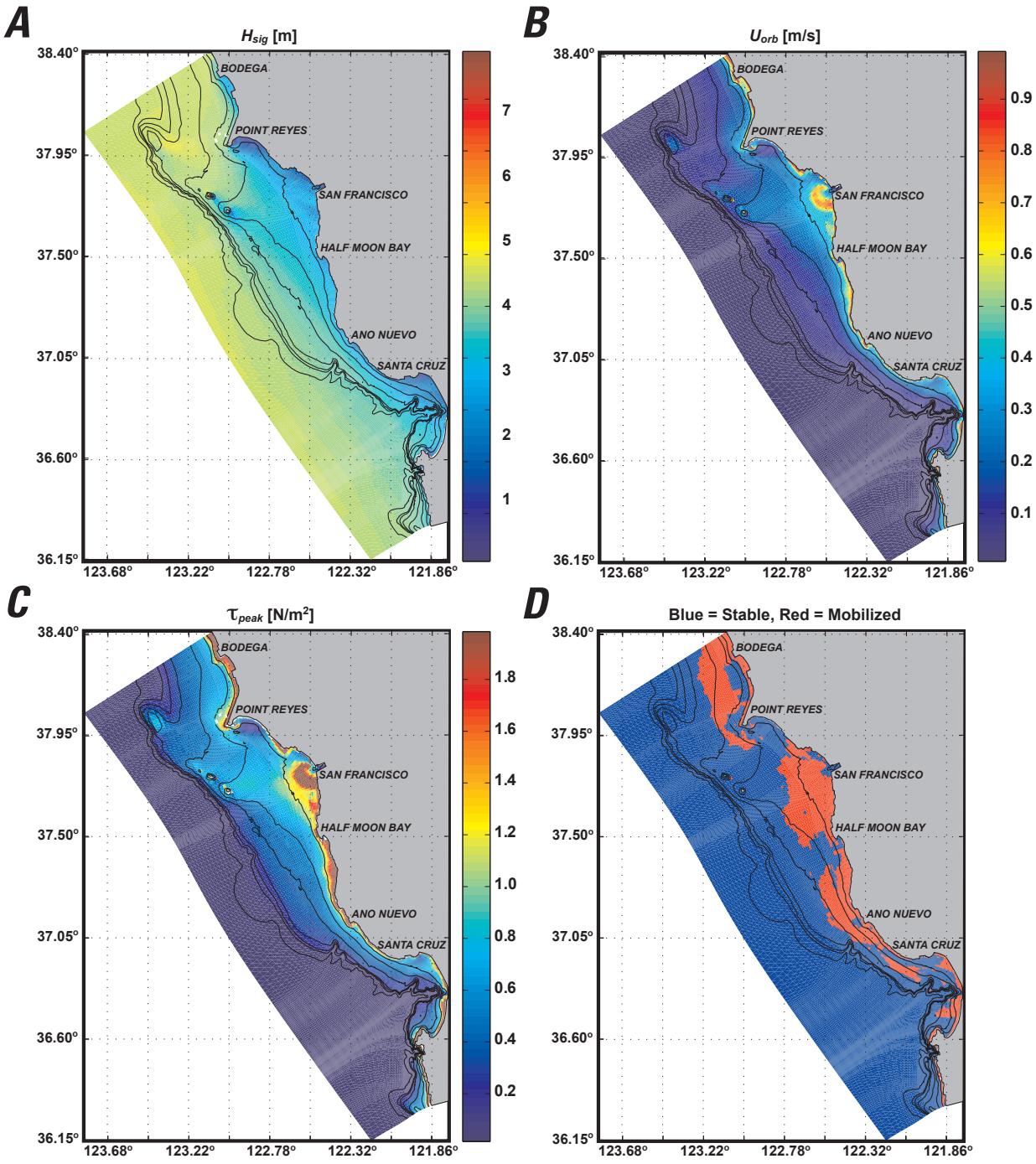

Appendix 34. Model run for a La Niña October. *A*, Map of significant wave height (H_{sig}), in m. *B*, Map of peak wave-induced near-bed orbital wave velocity (U_{orb}), in m/s. *C*, Map of peak wave-induced near-bed shear stress (τ_{peak}), in N/m^2. *D*, Map displaying which regions of the study area are mobilized (red) and which are stable (blue) for the modeled conditions. See table 2 for information on model run boundary conditions.

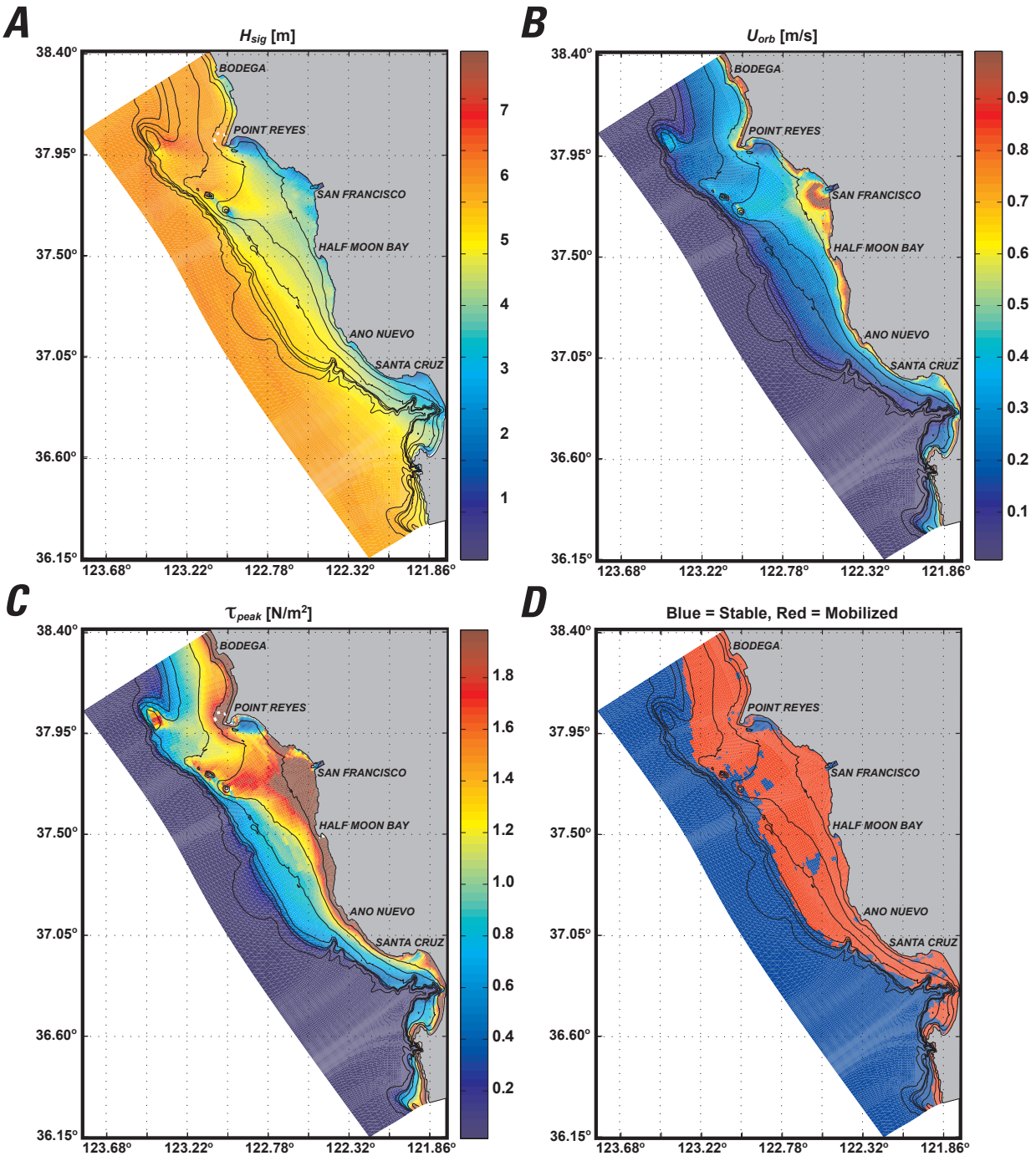

Appendix 35. Model run for a La Niña November. *A*, Map of significant wave height (H_{sig}), in m. *B*, Map of peak wave-induced near-bed orbital wave velocity (U_{orb}), in m/s. *C*, Map of peak wave-induced near-bed shear stress (τ_{peak}), in N/m^2. *D*, Map displaying which regions of the study area are mobilized (red) and which are stable (blue) for the modeled conditions. See table 2 for information on model run boundary conditions.

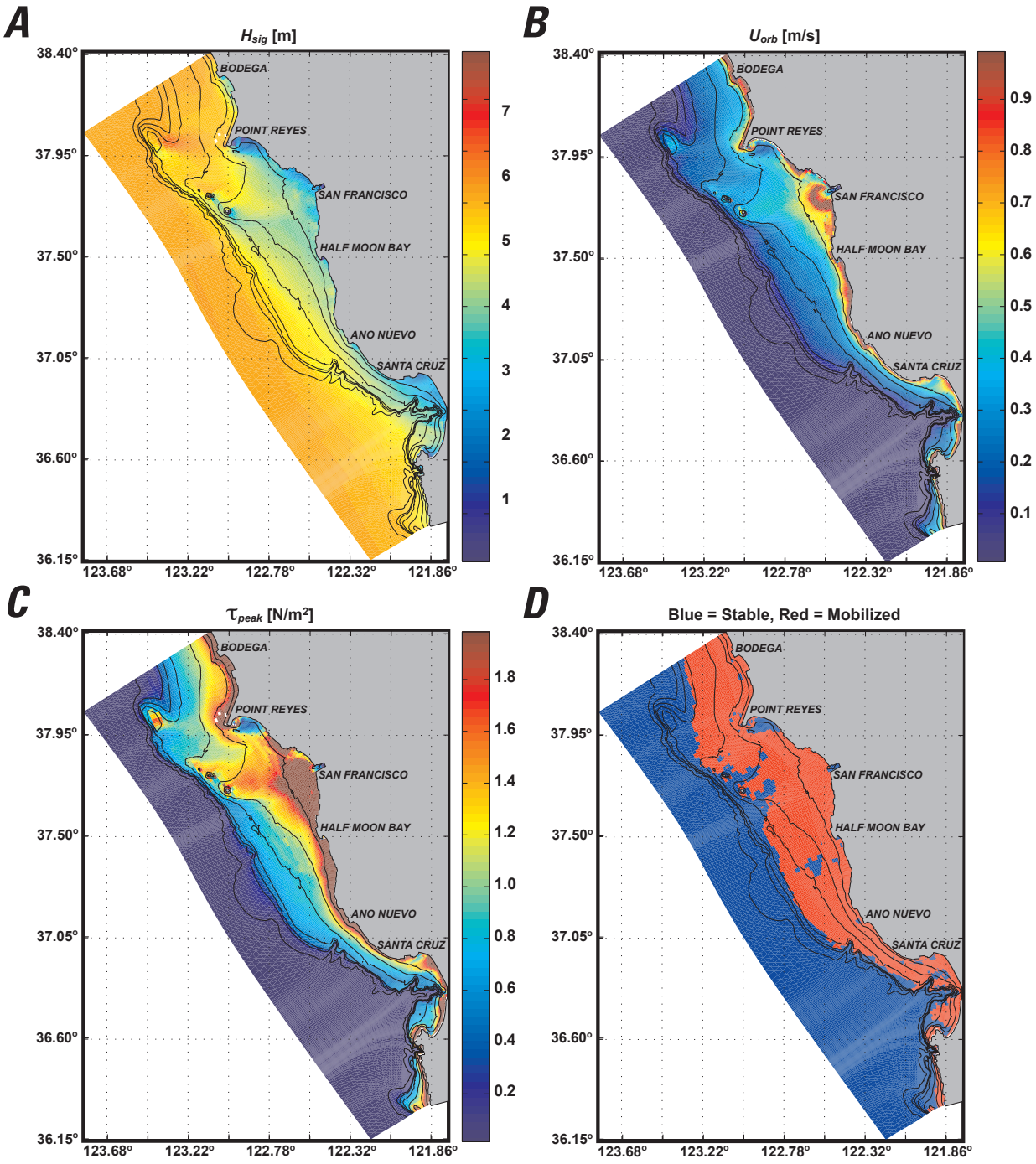

Appendix 36. Model run for a La Niña December. *A*, Map of significant wave height (H_{sig}), in m. *B*, Map of peak wave-induced near-bed orbital wave velocity (U_{orb}), in m/s. *C*, Map of peak wave-induced near-bed shear stress (τ_{peak}), in N/m^2. *D*, Map displaying which regions of the study area are mobilized (red) and which are stable (blue) for the modeled conditions. See table 2 for information on model run boundary conditions.

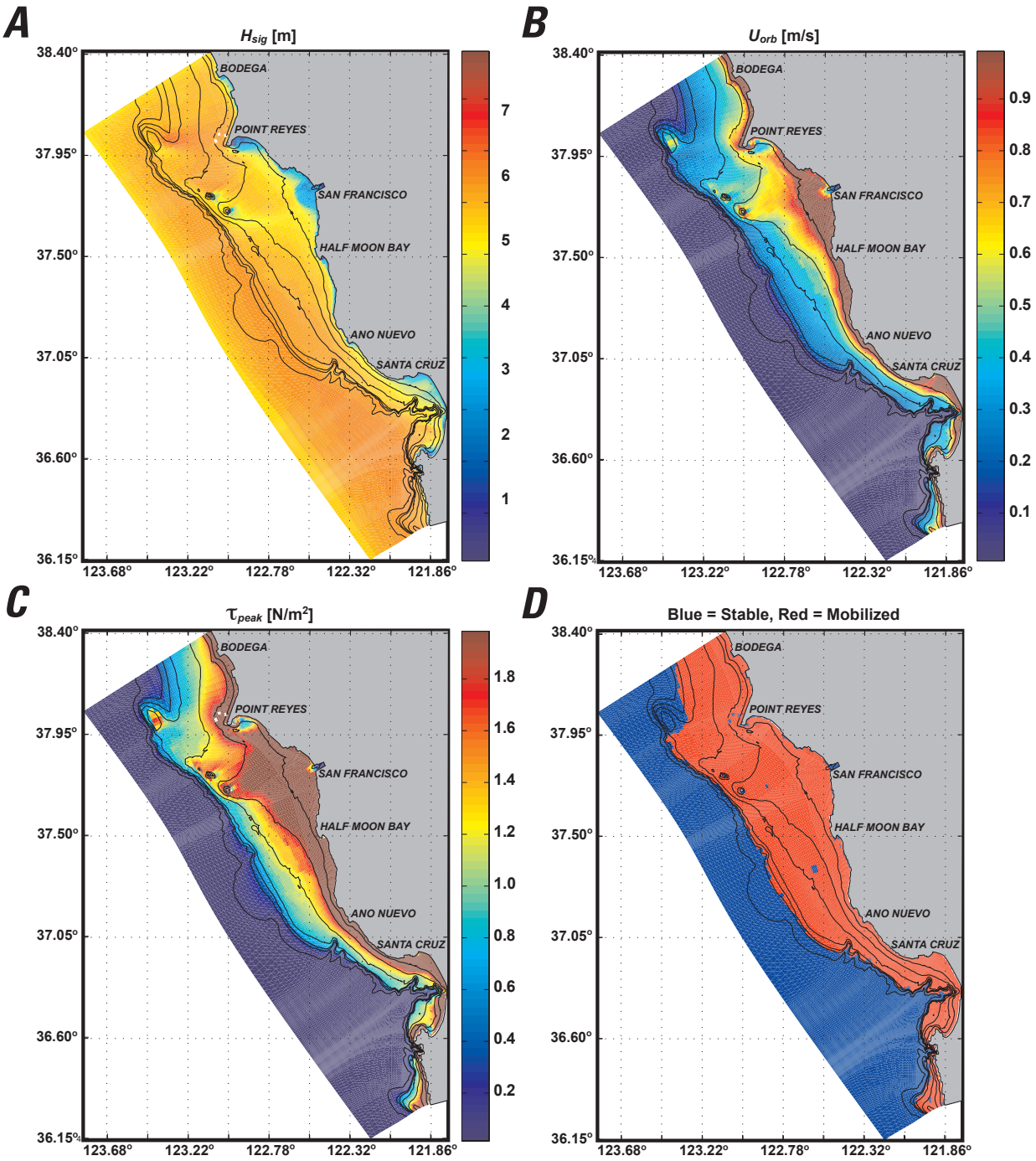

Appendix 37. Model run for a 2-year storm. *A*, Map of significant wave height (H_{sig}), in m. *B*, Map of peak wave-induced near-bed orbital wave velocity (U_{orb}), in m/s. *C*, Map of peak wave-induced near-bed shear stress (τ_{peak}), in N/m^2. *D*, Map displaying which regions of the study area are mobilized (red) and which are stable (blue) for the modeled conditions. See table 1 for information on model run boundary conditions.

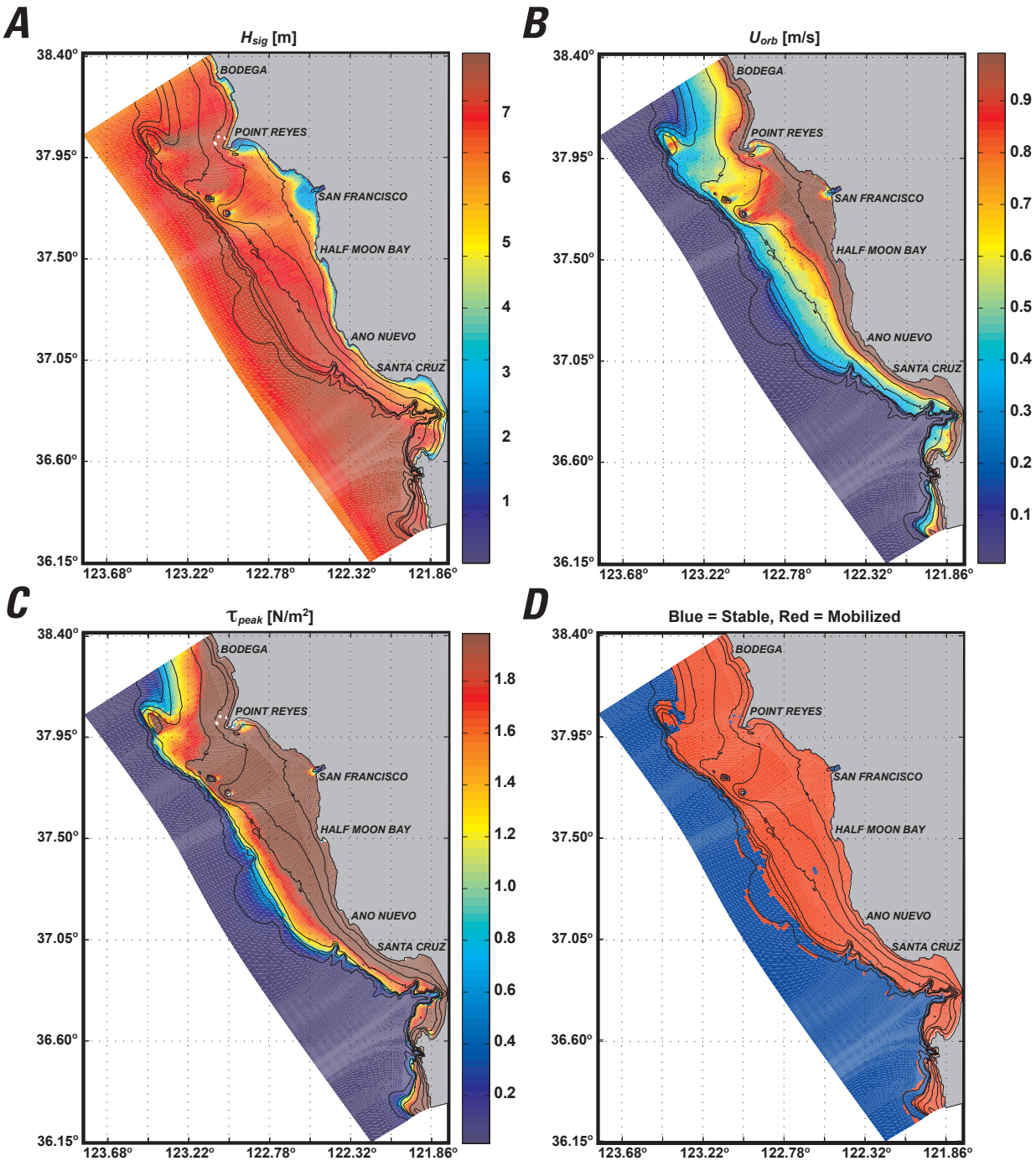

Appendix 38. Model run for a 10-year storm. *A*, Map of significant wave height (H_{sig}), in m. *B*, Map of peak wave-induced near-bed orbital wave velocity (U_{orb}), in m/s. *C*, Map of peak wave-induced near-bed shear stress (τ_{peak}), in N/m^2. *D*, Map displaying which regions of the study area are mobilized (red) and which are stable (blue) for the modeled conditions. See table 1 for information on model run boundary conditions.

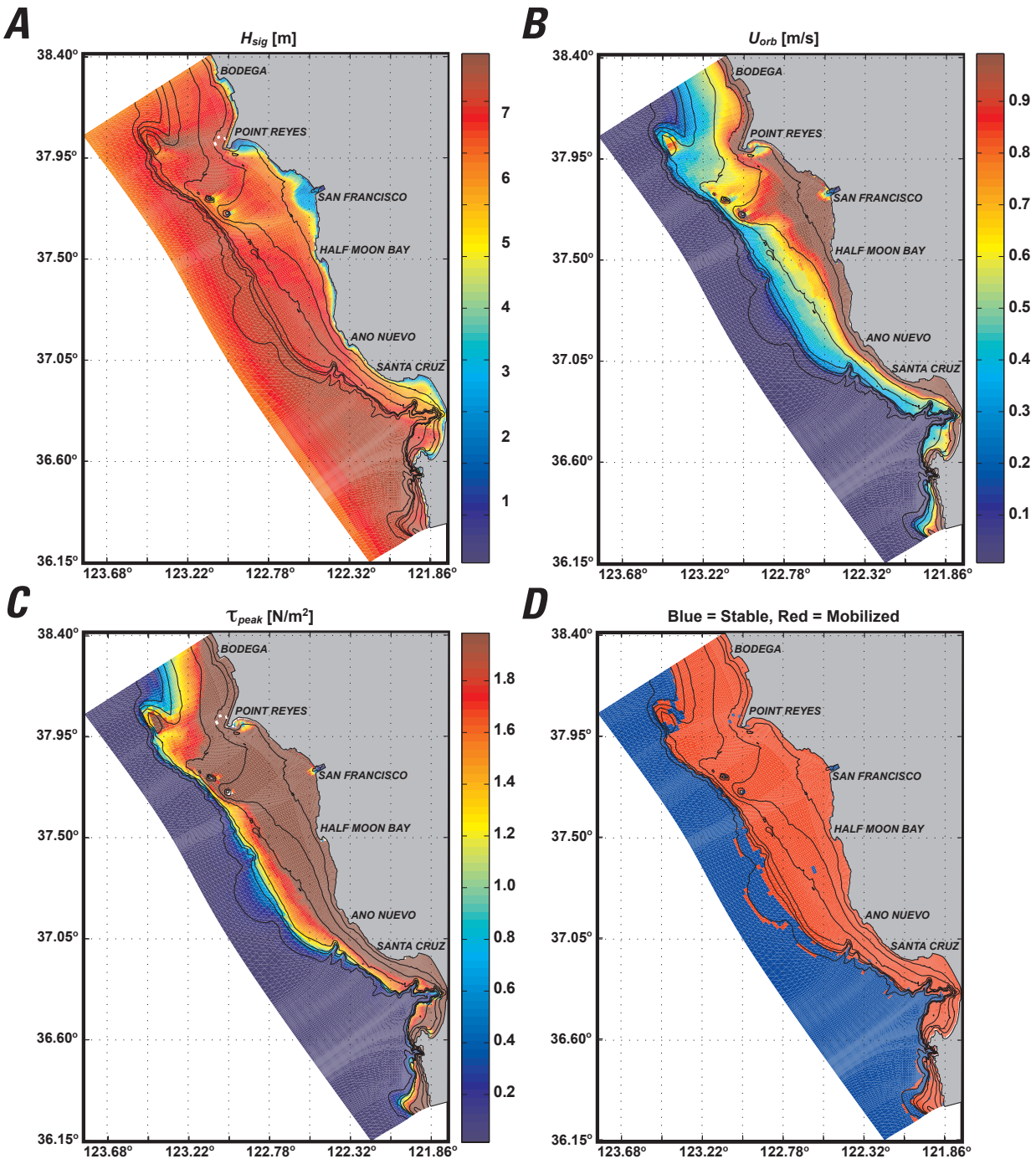

Appendix 39. Model run for a 25-year storm. *A*, Map of significant wave height (H_{sig}), in m. *B*, Map of peak wave-induced near-bed orbital wave velocity (U_{orb}), in m/s. *C*, Map of peak wave-induced near-bed shear stress (τ_{peak}), in N/m^2. *D*, Map displaying which regions of the study area are mobilized (red) and which are stable (blue) for the modeled conditions. See table 1 for information on model run boundary conditions.

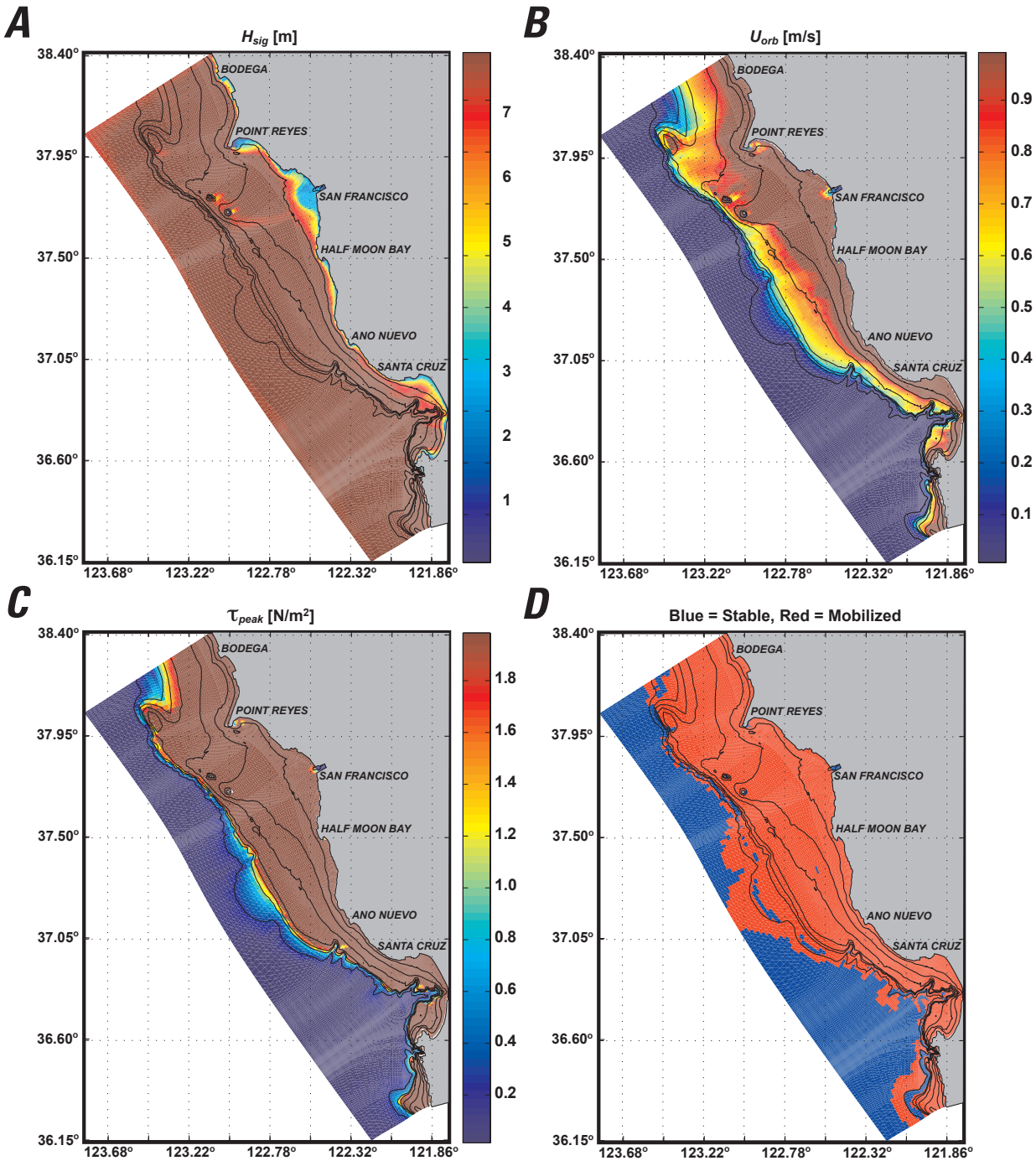

Appendix 40. Model run for a 50-year storm. *A*, Map of significant wave height (H_{sig}), in m. *B*, Map of peak wave-induced near-bed orbital wave velocity (U_{orb}), in m/s. *C*, Map of peak wave-induced near-bed shear stress (τ_{peak}), in N/m^2. *D*, Map displaying which regions of the study area are mobilized (red) and which are stable (blue) for the modeled conditions. See table 1 for information on model run boundary conditions.

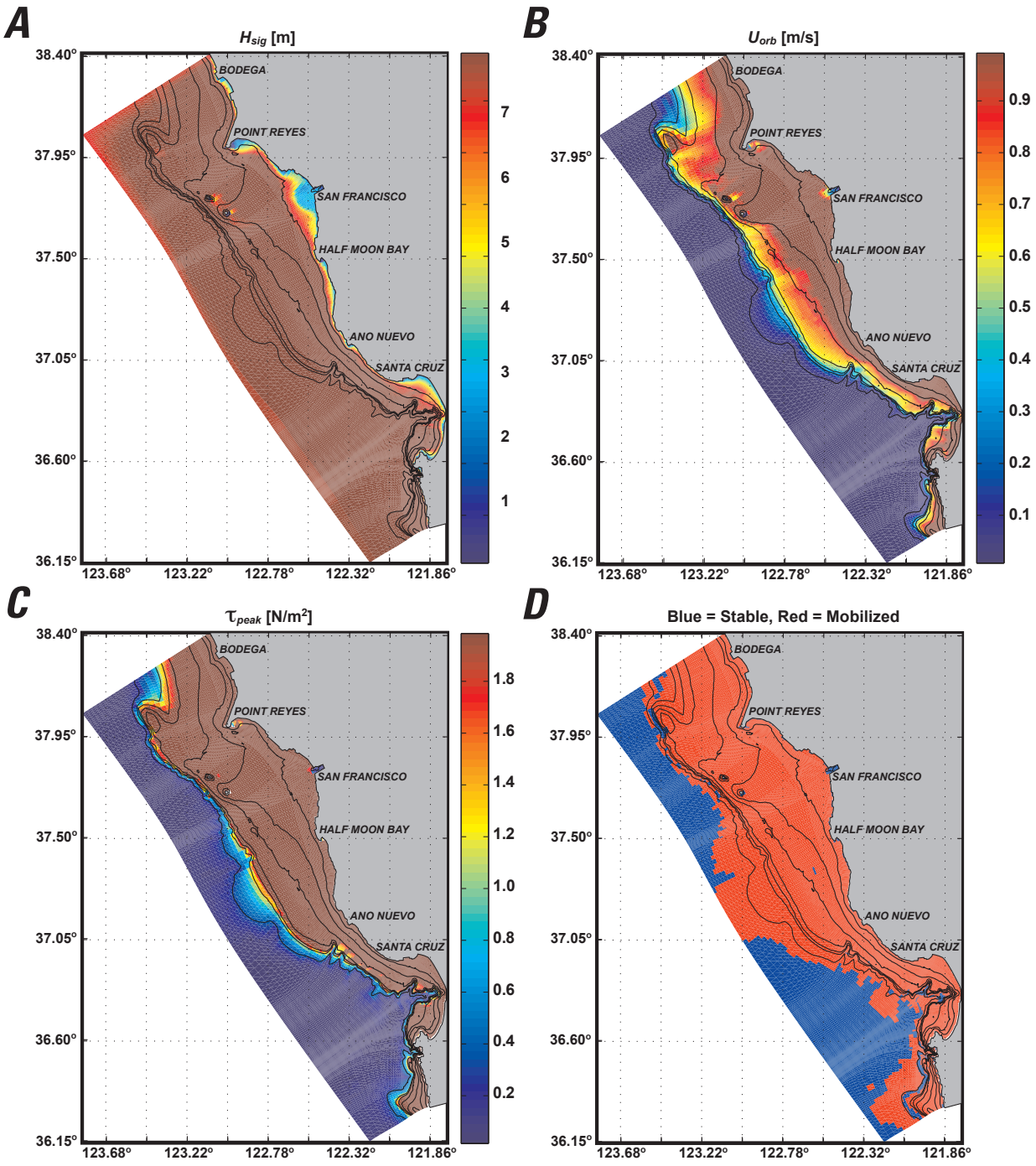

Appendix 41. Model run for a 100-year storm. *A*, Map of significant wave height (H_{sig}), in m. *B*, Map of peak wave-induced near-bed orbital wave velocity (U_{orb}), in m/s. *C*, Map of peak wave-induced near-bed shear stress (τ_{peak}), in N/m^2. *D*, Map displaying which regions of the study area are mobilized (red) and which are stable (blue) for the modeled conditions. See table 1 for information on model run boundary conditions.

This page intentionally left blank

Printed on recycled paper